Portable Insect Detection System for Stored-Product Pests

by

Garrett Shawn Kozyniak

A thesis submitted to

The Faculty of Graduate Studies of

The University of Manitoba

in partial fulfillment of the requirements

for the degree of

Master of Science

Department of Physics and Astronomy

The University of Manitoba

Winnipeg, Manitoba, Canada

February 2025

Copyright © 2025 Garrett Shawn Kozyniak

Thesis Advisor

Dr. Can-Ming Hu

Author

Garrett Shawn Kozyniak

Portable Insect Detection System for Stored-Product Pests

Abstract

Finding cost-effective methods to protect farmers' crops is essential for safeguarding their livelihoods and addressing global food insecurity, as crop losses reduce farmers' incomes and decrease food availability worldwide. This thesis presents a portable insect detection system utilizing a novel configuration of an interdigital capacitor (IDC) microwave oscillator combined with a Software Defined Radio (HackRF) transmitter/receiver application. This low-cost system relies on the microwave resonant cavity perturbation properties and the intense electric-field characteristics of the IDC to detect the movement of two insect species, *Tribolium castaneum* the Red Flour Beetle (RFB) and *Cryptolestes ferrugineus* the Rusty Grain Beetle (RGB). A modified probe-trap and microwave sensor was used to capture and detect the presence of RFBs within 10 kg of grain using a threshold analysis technique. In addition, small (SM) and large (LG) boundary configurations of the microwave sensor were fabricated to evaluate their effectiveness in differentiating the RFB and RGB signals in the presence of strong and weak electric-fields. An energy expenditure power-law relationship between insect activity and time was identified, revealing for the first time a heightened activity within $T < 60$ minutes, followed by a lowered constant insect activity for $T > 60$ minutes, scaling with insect numbers $M \in [1, 5]$ for both RFBs and RGBs over a 12-hour period. A time interval-dependent frequency shift and insect activity sensitivity analysis conducted led to the development of a predictive model comparing signals between 1-to-5 RFB and RGB insects using a 95% Confidence Estimate. It was determined that the SM bounded sensor provided overall insect signal enhancement, particularly for the RGB, and

excelled when combined frequency shift and insect activity metrics were used for distinguishing insect species. However, the LG boundary only increased species-specific frequency shift differentiation. An optimal species comparison was achieved at time intervals of $T_{\text{int}} = 1, 5$ minutes for both boundaries. This portable system and analysis technique lay the foundations for future comparison of different species and numbers of insects, offering potential application in insect threshold-based pest control strategies.

Keywords: Insect Counting, Insect Activity, Portable Insect Detection

Contents

Title Page i

Abstract i

Contents iii

List of Tables vi

List of Figures viii

Acknowledgements xix

1 Introduction 1

2 Theoretical Background 8

2.1 Coplanar Waveguide (CPW) Transmission Line 9

2.2 IDC Resonant Frequency 13

2.2.1 CPW-Backed IDC Resonator 15

2.3 Dielectric Perturbation for Microwave-Based Sensors 17

2.3.1 Dielectric Perturbation 18

2.3.2 Insect Detection using Δf 20

2.4 Microwave Oscillator Models 21

2.4.1 Laplace Analysis and Stability . . . 22
2.4.2 Feedback Model . . . 22
2.4.3 Negative Resistance Model . . . 24
2.4.4 Application to Insect Detection . . . 26
2.5 Analog-to-Digital Signals in RF Systems . . . 26
2.5.1 Quadrature Demodulation . . . 27
2.5.2 Discrete Fourier Transform and Fast Fourier Transform . . . 29
2.5.3 Digital Frequency Spectrum . . . 30
2.5.4 Portable Receiver . . . 31

3 Portable Insect Detection System 32

3.1 Microwave Sensor Characterization . . . 33
3.1.1 IDC Microwave Oscillator . . . 36
3.1.2 Portable Setup . . . 37
3.2 Preliminary Results using Insect Detection System . . . 41
3.2.1 Insect Rearing Information . . . 42
3.2.2 Insect Detection System Experimental Methods . . . 43
3.2.3 RFB, RGB, and Grain Movement Detection . . . 45
3.3 Grain Container and Microwave Probe Sensor . . . 46
3.3.1 Microwave Probe Sensor Setup . . . 47
3.3.2 RFB Capture Time Analysis . . . 47
3.3.3 In-Grain RFB Detection using Microwave Probe Sensor . . . 49
3.4 Conclusion . . . 52

4 Insect Activity and Counting 54

4.1 Background on Insect Movement Dynamics and Sensor Interactions . . . 55
4.1.1 Position Detecting Insect Movement Dynamics . . . 55
4.1.2 Frequency and Position Relationship of a Dielectric Probe . . . 57

4.1.3 Power-Law Dynamics of Insect Activity-Duration Relationship 60
4.2 Experimental and Measurement Methods 61
4.3 T.Castaneum / Red flour beetles (RFB) 67
4.3.1 RFB Insect Activity 67
4.3.2 RFB σ_A *vs.* $\Delta\bar{f}$ Relationship 73
4.4 C. Ferrugenius / Rusty grain beetles (RGB) 80
4.4.1 RGB Insect Activity 81
4.4.2 RGB σ_A vs. $\Delta\bar{f}$ Relationship 87
4.5 Comparison between RFB and RGB 94
4.5.1 Relative Sensitivity for a Single RGB and RFB 95
4.5.2 Sensitivity Comparison between 1-to-5 RFBs and RGBs 97
4.6 Conclusion 105

5 Outlook **109**
5.0.1 Cost-Benefit Analysis Example 111
5.0.2 Future Work 112

Appendices **116**

A Time-Interval Dependent Sensitivity **117**

Bibliography **122**

List of Tables

3.1 Microwave sensor dimensions of the top and bottom surface (sensor size $W_B \times L_B$ measured from either top or bottom surface). 34

4.1 $\Delta\bar{f}(\vec{x})$ and $\sigma^2_{\bar{f}}$ results of LG and SM boundaries of dielectric probes with Contact areas $C = (2 \times 1)\,\mathrm{mm}^2$ and $C = (3 \times 1)\,\mathrm{mm}^2$. 59

4.2 σ_A^{Act} Active Region At_{norm}^{-B} fit and Spontaneous Region constant σ_A^{Sp} results for $M = 1, 2, 3, 4, 5$ RFBs in SM and LG boundaries. 70

4.3 Initial Activity $A(M) = A'M + A'_o$ and Spontaneous Activity $\sigma_A^{Sp}(M) = S_{\sigma_A^{Sp}} M + \sigma_o^{Sp}$ fit results for $M = 1, 2, 3, 4, 5$ RFBs in SM and LG boundaries from Figure 4.8. 72

4.4 σ_A^{Act} Active Region At_{norm}^{-B} fit and spontaneous region constant σ_A^{Sp} results for $M = 1, 2, 3, 4, 5$ RGBs in SM and LG boundaries. 85

4.5 Initial Activity $A(M) = A'M + A'_o$ and Spontaneous Activity $\sigma_A^{Sp}(M) = S_{\sigma_A^{Sp}} M + \sigma_o^{Sp}$ fit results for $M = 1, 2, 3, 4, 5$ RGBs in SM and LG boundaries from Figure 4.15. 87

A.1 Time interval dependent insect activity and frequency shift RFB response using SM boundary 118

A.2 Time interval dependent insect activity and frequency shift RFB response using LG boundary 119
A.3 Time interval dependent insect activity and frequency shift RGB response using SM boundary 120
A.4 Time interval dependent insect activity and frequency shift RGB response using LG boundary 121

List of Figures

2.1 **Ungrounded CPW EM-Field Distribution.** A cross-sectional diagram of the Ungrounded CPW transmission line structure with electric (E)- and magnetic (H)- Field distribution about the signal line propagation. 10

2.2 **CPW Dielectric Regions.** A cross-sectional diagram of the Ungrounded CPW transmission with three dielectric regions confined by a magnetic boundary line. 11

2.3 **IDC Structure.** (a) Cross-section of unit cell IDC structure in 3 dielectric regions. (b) Top-view of IDC resonator with N electrodes and $N-1$ unit cells. 14

2.4 **MUT and C_1 Sensitivity.** (a) MUT with permeated electric field lines of parallel plate capacitor. (b) Open-plate capacitor with narrow electrode spacing w_g. (c) Open-plate capacitor with wide electrode spacing w_g. Extended E-Field lines with saturation height t_s (red-dotted line) permeate MUT. (d) C_1 99.5% saturation value of height t_s as a function of electrode spacing with $w_f = 0.5mm$. 16

2.5 **Dielectric Perturbation of Microwave Cavity** (a) Original cavity.(b) Full-volume dielectric perturbed cavity (c) Small-volume dielectric perturbed cavity 19

2.6 **Microwave Cavity Dielectric Perturbation from Moving Insects.** Microwave cavity with original dielectric perturbation for moving dielectric inclusions of same shape, volume and dielectric constant for multiple identical insects 21

2.7 **Feedback Loop Model.** Two-port feedback model composed of an Amplifier $A(s)$ and Frequency Selective Network $H(s)$. 23

2.8 **Negative Resistance Model.** One-port negative resistance model of an Active Circuit (Amplifier) and Frequency-selective Circuit (Network) decomposed into their impedances. 24

2.9 **Analog-to-Digital Path using Quadrature Demodulation.** Analog-to-Digital RF signal path separated into discrete I/Q samples to be processed by DSP block. 28

2.10 **Fast Fourier Transform (FFT) and Frequency Spectrum.** (a) FFT conversion of discrete time domain to discrete frequency domain of size N. (b) FFT-shifted discrete signal to display $|X[k]|$ frequency spectrum of bandwidth f_s. 30

3.1 **Microwave Sensor Schematics.** Horizontal dimensions of RO4350B $\epsilon_r = 3.66$ with 35 μm copper trace thickness (board size: $W_B \times L_B$) (a) Top surface of sensor with black dotted outlined ringed ($L_R \times L_R$) IDC structure connected via trace length L_A to output port. (b) Bottom surface of sensor: gap-coupled CPW backside (s_{TL}: slot width, g_{TL}: gap width, and L_{TL}: transmission line length). (c) IDC structure inside of square copper trace of width w_R composed of 4 columns of 8 digital fingers (l_f: finger length, w_f: finger width, and w_g: gap width). 34

3.2 **Measured and Simulated $|S_{21}|$.** (a) Experimental $|S_{21}|$ measurement using VNA and IDC Resonator with impedance matched load at the output port. (b) IDC resonator HFSS simulation of the resonator surface and electric-field magnitude color coded at resonance f_r.(c) Measured (solid-blue line) and simulated (dotted-black line)$|S_{21}|$ parameter of the IDC resonator. Resonance frequency f_r is the simulated resonance frequency (solid-red line) near the measured resonance frequency. 35

3.3 **Experimental Setup with Microwave Sensor.** Microwave sensor composed of VDC, LNA, and IDC resonator connected via output port to a signal analyzer. Spectrum recorded and analyzed with MATLAB software using a Laptop. . . 37

3.4 **Microwave Sensor Performance.** (a) Typical power density spectrum at 3.7 VDC input (blue markers) with Gaussian distribution fit (solid-red line) of the offset oscillation frequency Δf_o. (b) Bandwidth measurements with error bars as a function of input voltage. (c) Microwave sensor output power (blue markers) and power efficiency (orange) as a function of input voltage. 38

3.5 **Hardware Transmitter and Receiver Flowpath.** Flowpath of Transmitter (Microwave Sensor) and Receiver (HackRF One SDR) path communicating wirelessly via Antenna. Data recorded and analyzed in Host CPU. 39

3.6 **GNU Radio Software Data Stream Flowpath.** Flowpath of the data stream input from HackRF into GNU Radio framweork. A Hardware-to-Software link interface (API) splits parallel data stream between GUI and DSP recording. The GUI interfaces directly with and can control HackRF, DSP and File Handling blocks individually for real-time software editing. . . 40

3.7 **Portable Insect Detection System.** The general insect detection system composed of a microwave sensor transmitter, HackRF One SDR receiver, and interfaced with GNU Radio. This wireless setup utilizes antennas at receiver input and transmitter output ports. 41

3.8 **Microwave Sensor for Analyte Movement Experiment.**(a) Modified microwave sensor composed of open ended glass cylindrical vial and lid centered about the sensor. Analytes used are RFB ($\sim$ 4 mm in length), RGB ($\sim$ 2 mm in length), and grain kernel. (b) Typical time-series data of an analyte detected at t_1 on the IDC surface inducing a Δf_m and df_{m+1} per time step dt for every $f_m(t_m)$ based on the position of the analyte. 44

3.9 **Analyte Detection Results.** Multiple insect signal response events: (a) Frequency shift response Δf with 2 MHz Offset between trials and (b) Instantaneous insect activity level $|df/dt|$ with 100 MHz/s Offset. Bare sensor response with no insect is represented by black solid-line in (a) and (b), Single grain drop signal response event: (c) Δf. (d) $|df/dt|$ with inset of total transient time of grain drop event. Maximum values are provided by a black scale in each plot. 46

3.10 **Grain Container and Microwave Probe Sensor Setup.** (a) Experimental grain container test setup using the portable insect detection system with modified microwave sensor placed in container of 10 kg of wheat grain (dotted-yellow line). Communicating wirelessly via antenna. (b) Modified microwave probe trap sensor with 5 mm trapping boundary. Antenna output from sensor connects to antenna peaking outside of grain. 48

3.11 **Microwave Probe Sensor $|df/dt|$ and Δf Results.** 19.5 hrs time-series results for different RFB insect densities (blue line: 0.5 Insect/kg and orange line: 1 Insect/kg) and bare sensor/clean grain (black line). (a) Δf *vs. Time.* (b) $|df/dt|$ *vs. Time.* 50

3.12 **Threshold Detection Level Duration Example.** Detection Level between 0 (undetected) and 1 (detected). Capture time constrained for duration $D > 1$ seconds and 15 minutes from last detection to be considered a single capture event. Detection time in shaded green region with Capture Time CT time bound between dotted-black lines. (a) 3 detection's at 0.5 insect/kg. (b) 3 detection's at 1 insect/kg. 51

4.1 **Sensing Environment.** (a) An insect and a positional sensor in copper-orange has their positions defined by X and Y gray grid-line coordinates within a black boundary sensing environment. (b) Unstimulated movement of an insect with yellow arrows indicating a change in position of a change in time t_m. (c) Stimulated movement. 56

4.2 **Dielectric Probe $\Delta f(\vec{x})$ Mapping.** (a) Experimental setup using a dielectric probe and XYZ stage on the microwave sensor (LNA and IDC resonator). (b) $x-$ and $y-$ sweep direction along the $(24 \times 24)\,\mathrm{mm}^2$ Microwave sensor surface using a dielectric probe in contact with the IDC resonator. (c) $\Delta f(\vec{x})$ mapping of $(3 \times 1)\,\mathrm{mm}^2$ contact surface area and 30 mm height ROGERS TMM13i $\epsilon_r = 12.85$ dielectric probe. (d) $\Delta f(\vec{x})$ mapping of $(3 \times 10\,\mathrm{mm}^2)$ contact surface area and 30 mm height ROGERS TMM3 $\epsilon_r = 3.27$ dielectric probe. (e) $\Delta f(\vec{x})$ mapping of $(2 \times 1)\,\mathrm{mm}^2$ contact surface area and $30mm$ height ROGERS TMM3 $\epsilon_r = 3.27$ dielectric probe. Two artificial boundaries are defined: Large (LG) boundary containing area and the Small (SM) boundary area. 58

4.3 **Insect Activity-Duration Relationship.** (a) Insect activity as a function of time displaying a decaying red-line power-law with insect activity parameter A and decay parameter B for stimulated insect movement within an Active Region of time shaded in red. A flat red-line in shaded-blue Spontaneous Region of time represents the constant spontaneous insect activity σ_A^{Sp} corresponding to unstimulated insect movement. 61

4.4 **Portable Experimental Setup with Different Sized Boundaries.** (a) Portable experimental system consisting of a bounded microwave sensor powered via LNA AC/DC rechargeable battery, HackRF One SDR receiver, and GNU interface. (b) Cellophane lined 20×20 mm^2 inner diameter large (LG) boundary sensor configuration. The orange-dotted line represents the bounded strong and weak electric-field locations on the sensor. (c) Cellophane lined 16×13 mm^2 inner diameter small (SM) boundary sensor configuration. The red-dotted line represents the bounded strong electric-field locations on the sensor. The height of both boundaries is 24 mm. 63

4.5 **Stimulating Insect Movement.** Sample vial containing insects of adult RFB (4 mm length) or adult RGB (2 mm length) are forcibly removed and dropped onto sensor to stimulate movement. Bounded microwave sensor with sealed on top by a lid with a hole that is covered to prevent visual light from interfering with insect samples. 64

4.6 **Baseline Sensor Measurements with both Boundaries** σ_A and $\Delta\bar{f}$ absent insects over discrete time intervals T_{int}. (a) SM boundary df/dt histogram distribution at $T_{int} = 1$ min sample $n = 1$. (b) LG boundary df/dt histogram distribution at $T_{int} = 1$ minute sample $n = 1$. (c) $\Delta\bar{f}$ trend for 10 12hr SM and LG sample measurements over 10 time intervals.(d) σ_A trend for 10 12hr SM and LG sample measurements over 10 time intervals. Time intervals $T_{int}[min] = [1, 5, 15, 30, 60, 120, 240, 360, 480, 720]$. 66

4.7 **SM and LG Boundary RFB Insect Activity σ_A.** (a,b) SM(LG) boundary σ_A for 720 minutes using $T_i = 1$ minute intervals. Heightened σ_A defined at $T < 60$ minute in shaded red as Active Region. Mean σ_A defined at $T > 60$ minute by solid black line with black shaded 95% Prediction Interval for the Spontaneous Region.(c,d) SM(LG) boundary σ_A within the Active Region fit with power law function $\sigma_A = At_{norm}^{-B}$ represented by a red line bounded by 95% Prediction Interval shaded in red. 68

4.8 **RFB Insect Activity Relationship with Insect Number.** Plotted using fit results from Table 4.2 for $M = 1, 2, 3, 4, 5$ RFBs. $A(M) = A'M + A'_o$ fit via solid red line with shaded red 95% confidence interval region in (a) SM boundary and (b) LG boundary. $\sigma_A^{Sp}(M) = S_{\sigma_A^{Sp}} M + \sigma_o^{Sp}$ fit via solid red line with shaded red 95% confidence interval region in (c) SM boundary and (d) LG boundary. Decay coefficient B for (e) SM boundary case and (f) LG boundary case. 71

4.9 **σ_A and $\Delta\bar{f}$ Dynamics as a Function of Time Interval for a Single RFB.** The time interval $T_{int}[min] = [1, 5, 15, 30, 60, 120, 240, 360, 480, 720]$ is represented by the vertically dashed gray lines in (a-d), with standard error of the mean represented by error bars in (a-f), and blue shaded $\Delta\bar{f}$ pooled standard error. (a) σ_A *vs.* T_{int} for SM bounded sensor. (b) $\Delta\bar{f}$ *vs.* T_{int} for SM bounded sensor.(c) σ_A *vs.* T_{int} for LG bounded sensor. (d) $\Delta\bar{f}$ *vs.* T_{int} for LG bounded sensor. (e,f) σ_A *vs.* $\Delta\bar{f}$ plots with vertically descending data points for ascending T_{int} intervals. (e)σ_A *vs.* $\Delta\bar{f}$ for SM boundary. (f) σ_A *vs* $\Delta\bar{f}$ for LG boundary. 74

4.10 σ_A *vs.* $\Delta\bar{f}$ **Plot for** $M = 1, 2, 3, 3, 5$ **RFBs.** σ_A *vs.*$\Delta\bar{f}$ relationship colour-coded for multiple RFBs using different boundaries with shaded $\Delta\bar{f}$ pooled standard errors (a) SM boundary. Inflection point represented by dotted black line at $T_{inf} = 60$ minutes ($T_{inf} = 30$ minutes $M = 2$). (b) LG Boundary. Absent consistent inflection point. 77

4.11 $\Delta\bar{f}$ **and** σ_A *vs.* M **RFB at** $T_{int} = 1$ **minute.** Weighted least-squares regression solid red line fit of frequency shift $\Delta\bar{f} = S_{\Delta\bar{f}}M$ and insect activity $\sigma_A = S_{\sigma_A}M + \sigma_o$ with 95% confidence interval shaded red region for $T_{int} = 1$ minute (a) $\Delta\bar{f}$ SM boundary (b) $\Delta\bar{f}$ LG boundary. (c) σ_A SM boundary. (d) σ_A LG boundary. 78

4.12 $S_{\Delta\bar{f}}$, $S_{\sigma A}$, **and** σ_o, *vs.* T_{int} **for RFB.** Linear fitting parameters of Figure 4.10 with S.E. as a function of T_{int} for both boundaries. (a) $S_{\Delta\bar{f}}$, (b) $S_{\sigma A}$, and (c) σ_o. 79

4.13 **SM and LG Boundary Insect Activity** σ_A **of RGB for** $T_i = 1$ **minute.** (a) SM boundary σ_A over 720 minutes. The heightened decaying σ_A is marked as the Active Region for $T < 60$ minutes, shaded in red. The mean σ_A for $T > 60$ minutes, representing the Spontaneous Region, is shown as a solid black line with a 95% prediction interval shaded in black. (b) LG boundary σ_A over 720 minutes, showing two active regions. Active Region 1 is defined for $T < 90$ minutes, and Active Region 2 is between $90 < T < 270$ minutes. The mean σ_A in Active Region 1 is represented by a solid red line with a 95% prediction interval shaded in red, while the mean σ_A in Active Region 2 is shown by a solid green line with a 95% prediction interval shaded in green. The Spontaneous Region for $T > 270$ minutes is indicated by a solid black line with a 95% prediction interval shaded in black. No decaying σ_A is observed. (c) SM boundary σ_A in the Active Region is fit with a power-law function $\sigma_A = At_{norm}^{-B}$, represented by a solid red line with a 95% prediction interval shaded in red. 82

4.14 **Insect Activity Dynamics for Multiple RGBs.** A log-log plot of σ_A time evolution for $M = 1, 2, 3, 4, 5$ RGBs using a time interval $T_i = 1$ minute fit with a power law duration relationship $\sigma_A^{Act} = At_{norm}^{-B}$ for each M. Absent error bars and prediction interval for clarity. (a) σ_A time evolution for SM boundary configuration for $M = 1, 2, 3, 4, 5$ RGBs with solid markers and solid line fits. (b) σ_A time evolution for LG boundary configuration for $M = 1, 2, 3, 4, 5$ RGBs with hollow markers and no fits. 84

4.15 **RGB Insect Activity Relationship with Insect Number.** Plotted using fit results from Table 4.4 for $M = 1, 2, 3, 4, 5$ RGBs. (a) $A(M) = A'M + A'_o$ fit via solid red line with shaded red 95% confidence interval region for SM boundary case. (b) Scaling power law decay coefficient for SM boundary case. (c) $\sigma_A^{Sp}(M) = S_{\sigma_A^{Sp}} M + \sigma_o^{Sp}$ fit via solid red line with shaded red 95% confidence interval region for SM boundary case. (d) $\sigma_A^{Sp}(M) = S_{\sigma_A^{Sp}} M + \sigma_o^{Sp}$ fit via solid red line with shaded red 95% confidence interval region for LG boundary case. 86

4.16 σ_A **and** $\Delta\bar{f}$ **Dynamics as a Function of Time Interval for a Single RGB.** The time interval $T_{int}[min] = [1, 5, 15, 30, 60, 120, 240, 360, 480, 720]$ is represented by the vertically dashed gray lines in (a-d), with standard error of the mean represented by error bars in (a-f), and blue shaded $\Delta\bar{f}$ pooled standard error. (a) σ_A *vs.* T_{int} for SM boundary. (b) $\Delta\bar{f}$ *vs.* T_{int} for SM boundary.(c) σ_A *vs.* T_{int} for LG boundary. (d) $\Delta\bar{f}$ *vs.* T_{int} for LG boundary. (e,f) σ_A *vs.* $\Delta\bar{f}$ plots with vertically descending data points for ascending T_{int} intervals. (e) σ_A *vs.* $\Delta\bar{f}$ for SM boundary. (f) σ_A *vs.* $\Delta\bar{f}$ for LG boundary. . 88

4.17 σ_A *vs.* $\Delta\bar{f}$ **plot for** $M = 1, 2, 3, 3, 5$ **RGBs.** σ_A *vs.*$\Delta\bar{f}$ relationship colour-coded for multiple RGBs using different boundaries with shaded $\Delta\bar{f}$ pooled standard errors (a) SM boundary case: inflection point represented by dotted black dotted line at $T_{inf} = 30$ minutes ($T_{inf} = 60$ minutes $M = 1 and 2$. Anti-inflection point represented by a red solid line through $T_{inf'} = 5$ minutes. (b) LG boundary case: Absent consistent inflection and anti-inflection point. . . 90

4.18 $\Delta\bar{f}$ **and** σ_A *vs.* M **RGB at** $T_{int} = 1$ **minute.** Weighted least-squares linear regression solid red line fit of frequency shift $\Delta\bar{f} = S_{\Delta\bar{f}}M$ and insect activity $\sigma_A = S_{\sigma_A}M + \sigma_o$ with 95% confidence interval shaded red region for $T_{int} = 1$ minute (a) $\Delta\bar{f}$ SM boundary case (b) $\Delta\bar{f}$ LG boundary case. (c) σ_A SM boundary case. (d) σ_A LG boundary case. 92

4.19 $S_{\Delta\bar{f}}$**,** $S_{\sigma A}$**, and** σ_o**, vs.** T_{int} **for RGB** Linear fitting parameters of Figure 4.10 with S.E. as a function of T_{int} for both boundaries. (a) $S_{\Delta\bar{f}}$, (b) $S_{\sigma A}$, and (c) σ_o. 93

4.20 **Relative Sensitivity Single RGB and RFB Measurements.** Single RFB and RGB 10 sample measurements comparison based on relative sensitivity. (a) Relative insect activity sensitivity with insect species comparison for same boundaries. (b) Relative frequency response sensitivity with insect species comparison for same boundaries. (c) Relative insect activity sensitivity with for individual insect using different boundaries. (d) Relative frequency response sensitivity with for individual insect using different boundaries. 96

4.21 **LG Boundary:1 RFB vs. 1-to-5 RGB** $|\Delta\bar{f}(M)|$ **and** $\sigma_A(M)$ **Bar Plot Comparison** Bar plot comparison using LG bounded configuration for 1 RFB to 1-to-5 RGB. RFB has solid bar colouring and RGB has hatched coloured bar coloring. The error bars are the 95% C.I. using the S.E from Figure 4.12 and Figure 4.19. (a) $|\Delta\bar{f}(M)|$ comparison. (b) $\sigma_A(M)$ comparison. 98

4.22 **SM Boundary:1 RFB vs. 1-to-5 RGB $|\Delta\bar{f}(M)|$ and $\sigma_A(M)$ Bar Plot Comparison** Bar Plot comparison using SM bounded configuration for 1 RFB to 1-to-5 RGB. RFB has solid bar colouring and RGB has hatched coloured bar coloring. The error bars are the 95% C.I. using the S.E from Figure 4.12 and Figure 4.19. (a) $|\Delta\bar{f}(M)|$ comparison. (b) $\sigma_A(M)$ comparison. 99

4.23 **SM Boundary $|\Delta\bar{f}(M)|$ Confidence Estimate Comparing 1 RFB with 5 RGB Example** (a) Constructing C.E. using $|\Delta\bar{f}(M)|$ of 1 RFB and 5 RGB at $T_{int} = 1$ minute bar plot comparing overlapping space of one-sided 95% C.I. (δx_{In}) light gray shaded regions to shaded gray measured difference Δx_{In} region between 1 RFB to 3 RGB example (1 RFB and 3 RGB has a non-overlapping region). (b) Colour coded distinguishability comparing overlapping region of 1 RFB to 5 RGBs with$C.E. \geq 100, \geq 75, \geq 50, \geq 25, \geq 0, and < 0\%$. Black indicating indistinguishability for a $C.E. < 0\%$ not shown here. 100

4.24 **LG Boundary C.E. Matrices for 1-to-5 RFB and RGB Comparisons.** Confidence Estimate matrices for RFB vs. RGB using LG boundary, showing distinguishability levels by predictor across time intervals. Color-coded percentages: $C.E. \geq 100$, ≥ 75, ≥ 50, ≥ 25, ≥ 0, and $< 0\%$, with high values indicating distinguishability and low/negative values indicating indistinguishability. (a) Insect activity comparison. (b) Frequency response comparison. 102

4.25 **SM Boundary C.E. Matrices for 1-to-5 RFB and RGB Comparisons.** Confidence Estimate matrices for RFB vs. RGB using SM boundary, showing distinguishability levels by predictor across time intervals. Color-coded percentages: $C.E. \geq 100$, ≥ 75, ≥ 50, ≥ 25, ≥ 0, and $< 0\%$, with high values indicating distinguishability and low/negative values indicating indistinguishability. (a) Insect activity comparison. (b) Frequency response comparison. 104

Acknowledgements

I'd like to first thank Dr. Can-Ming Hu, my thesis advisor, for giving me the opportunity to do such a thesis, as well as providing me the necessary guidance whenever I became lost. I like to individually thank all of my colleagues in the Dynamic Spintronics Lab. Thank you Jerry Lu for always helping when it came to 3D printing any arbitrary figure for my work. Thank you Jiguang Yao for the helpful discussions and challenging results when I naively accepted them. Thank you Chunlei Zhang for your patience and insightful discourse when teaching me new and exciting ideas in physics. Thank you Yi-Hui Zhang, for your understanding, patience and thoughtfulness. Thank you Mun Kim for being my first mentor and helping cultivate my skills in the lab prior to this thesis. Thank you Ying Yang for being such a kind friend and mentor in the Lab. A special thank you to Dr. Yongsheng Gui, who has been there from the beginning offering his insights and knowledge from his years of experience; which has honed my thinking. Again, thank you, everyone in my lab, I truly consider you all my dear friends for life.

Thank you to Dr. Fuji Jian, and his Ph.D student Kavi Mughil Murugesan for providing the vital insects necessary to do this study. Furthermore, thank you Kavi for your discussions and invaluable knowledge on insects as well as your relation to industry that helped guide my project in the right direction. Thank you to Research Manitoba for funding this project, and as an extension, thank you to the Lab2Market team for giving me a proper inlet in discovering what is truly useful to industry users.

I'd like to thank my committee members, Dr. Stephen Pistorius, for agreeing to review my work and for his advice during the report sessions. I'd like to thank Dr. Kurt Hildebrand for his valuable industry perspective and unwavering support pertaining to this project via meetings and correspondence. I'd also like to thank Susan Beshta for her help with anything related to graduate studies. Most of us would be lost without Susan.

Personally, I'd like to thank all my friends and family for always giving me support. I'd like to thank my parents for their patience and understanding, providing me a comfortable and safe space to grow my knowledge. Being patient with me during stressful times at University.

Saving the best for last, thank you to my wife, Siya Wu, my love of my life. Thank you for your gentle compassion, patience, and support. Thank you for providing clarity to my life; you have lifted me up and filled it with such joy and happiness. As the final chapter of this thesis ends, I cannot wait to see what our next chapter entails.

1

Introduction

With the rise in global conflicts, climate extremes, and inflationary food prices, food insecurity becomes increasingly dire. A Food and Agriculture Organization report in 2010 estimated that post-harvest losses equate to 1.3B tonnes of food loss worldwide [1]. Among developed countries, 10% of post-harvest losses is estimated to be attributed to insect infestations, a problem exacerbated in developing countries, witnessing an estimate of 20% of loss [2]. The impacts are felt in the degradation of the quality of stored goods, health hazards, financial losses related to product rejection, reduced quality grading, and the costs associated with treatment [3]. Typically, pest management treatments are chemically applied in and around storage facilities, often requiring specialized fumigants applied to grain [4, 5]. However, there is growing environmental and monetary concern with the increased cost of developing new chemicals to combat the production of resilient insects [6]. Thus, there is a real need for an early determination of insect presence to help guide Insect Pest Management (IPM) strategies.

Traditional field methods to determine the presence of insects require visual confirmation via sampling. Probe traps, pitfall traps, burlese funnels, triers, and sieving are the general methods discussed in [7–9] for sampling where species identification and counting are performed via the operator. Boosting sampling efficiency, traps will typically use attractants such as light [10] or pheromones [11] and may be accompanied by sticky adhesive to aid with visual inspection. Consequently, light traps are restricted to outdoor use, and pheromone

traps are affected by environmental factors and low ventilation, generally more suited for outside grain monitoring.

Although effective, the downsides of these manual methods are associated with the time and amount of labour required, and as a result, automated smart trap systems have been developed as a necessity of convenience [12]. Some of these smart systems include environmental sensors that measure an external parameter indirectly related to insects, such as temperature sensors that measure the generation of insect heat [13] and gas sensors that respond to the CO_2 byproduct of insect respiration [14]. Odor-sensing is based on sensors sensitive to chemical volatiles released by deteriorating grain, which was shown to be capable of differentiating between low moisture grain and *Tribolium castaneum* (Red Flour Beetles) [15]. However, in practice, these indirect methods usually link insect presence as a secondary result of high storage temperature and humidity, deteriorating grain, or fungi production, not the insect itself. Direct methods such as acoustic sensing, detecting insect sound, can estimate the population density within grain bulk [16] or imaging captured insects aided through deep learning can identify species and number [17]. Although, the downside to these methods is that they are susceptible to large data transfers, background noise (acoustic), and low light levels (imaging). However, there are other sophisticated methods to detect insects, such as X-ray Imaging [18] and Near-Infrared Spectroscopy [19], which can detect internal insects but suffer from high false positive rates, expensive operation, and complex calibration procedures.

With the extensive work developing automated insect detection systems, notable commercialized post-harvest insect detection systems have capitalized on this potential market where early-warning, insect number, and species identification being the most sought-after features. One of the most notable commercialized insect detector is known as the Electronic Grain Probe Insect Counter (EGPIC) [20], later developed through OPI. Limited as the *Insector*. Using an optical receiver array and laser combination, aptly placed as a "trip-wire" within a probe trap that estimates the size of the insect from an intensity distribution, which is easily countable; however, the insect signals exhibit significant overlap between very small

insects and are indistinguishable between *Tribolium castaneum* and the very common and similarly sized *Rhyzopertha dominica* [21, 22]. An additional problem occurs within the grain environment; the EGPIC is prone to false counts from debris falling into the sensor path, which is common during bin aeration procedures. These problems, coupled with the expensive cost, may be a deterrent for continual and future users. The more obvious and popular route is imaging captured insects often requiring pheromone bait and/or an adhesive pad to attract and render the insect immobile. Systems such as the *Sight Trap*, which is a baited hanging trap embedded with expensive high-resolution cameras and integrated *Foresight IPM* software to analyze the insect captures, are typically employed in storage areas [23]. Introducing artificial intelligence to image-based baited traps combined with environmental sensors is able to provide temperature, humidity, and insect capture results daily using AI technology registered as the *SmartProbe* by AIVision Food Inc [24]. Although relatively new, the system shows no evidence of species identification, and the low lighting and overcrowding effect of the imaging environment will misconstrue AI analysis of the true insect capture data, which is a common occurrence of this method. These automated systems demonstrate strong early-warning insect detection methods but show weakness in some cases of insect counting and species identification. Indicating that a new methodology for insect counting and identification would be a boon to the automated stored product smart trap industry.

It has been suggested that microwaves be an alternative method towards insect detection. A far-field motion-based detector using microwaves was shown to be able to resolve insect movement utilizing the Doppler effect by observing the frequency blue shift (forward movement relative to the observer) or frequency red shift (backward movement relative to the observer) of the transmitted and reflected microwaves from the target source. A commercial-based motion detector designed for termites was able to estimate the level of infestation for common storage insect pests which increased with insect number [25]. More recently, developed by our research group, an active microwave-based close-to-surface near-field sensor was used to detect a complex frequency response of a single common storage insect interacting with the

electric field of the sensor. Two species of different sizes (*T.castaneum*/Red Flour Beetle and *C.ferrugineus*/Rusty Grain Beetle) displayed different frequency responses in relation to the size and temperature-dependent movement of the insect and its distance from the surface [26]. Although restricted to a laboratory environment and lacking the necessary quantitative analysis metrics to count and identify insect species, this near-field microwave sensing approach demonstrated the potential of a microwave-based smart trap for insects.

Microwave-based sensors have been used extensively to quantify frequency responses of solid, liquid, and gaseous dielectric materials. The fundamental principle involves dielectric material "perturbing" the original electric field of a microwave resonant cavity or resonator, producing a new frequency-shifted resonance. A comprehensive review [27] on current material characterizations using microwave-planar devices illuminates simple, low-cost, and wide range of applications achievable with these systems. Benefiting from many easy applications is also a double-edged sword; they suffer from a lack of selectivity, often needing knowledge of the analyte or "bait" prior to use. Microwave transduction sensing utilizes special materials ('bait') that change their dielectric properties when interacting with target analytes, such as sensors embedded with inorganic materials sensitive to industrial gases including ammonia [28], carbon dioxide [29], and methane [30]. Another example involves a chemical reaction between a highly conductive thin film and water used with a microwave resonator, constructing an enhanced sensitivity humidity sensor [31]. Even organic materials such as SARS-CoV-2 antibodies were used as binding sites of a gold-plated microwave sensor to detect Covid-19 samples [24]. The implementation of analyte-selective materials onto the dielectric sensitive regions of the microwave resonator is the critical differentiator for real-world uses.

Often, the choice of resonator design stems on creating intense local electrical-fields for enhanced dielectric sensitivity. One such design, the interdigital capacitor (IDC) resonator, incorporates both a mixture of intense electric-fields between the interdigital space parallel to digital fingers or electrodes while having distributed electric-fields over a large surface for

enhanced field-material under test (MUT) interaction. These IDC resonators have been used for some specific applications, such as for complex permittivity measurements of solids [32] or even used with a gas sensitive thin film used to probe environmental changes [33]. However, like all the microwave sensors and IDC sensors mentioned before, these systems require the use of lab-equipment necessary for these experiments and can be deterrents for any non-expert user.

Typical near-field microwave sensors, mqy rely on a heavy and expensive Vector Network Analyzer (VNA) that powers and measures the microwave signals. Fortunately, microwave telecommunication has been simplified through the conception of *Software Defined Radios* (SDRs) comprising of *Digital-to-Analog* (D/A) and *Analog-to-Digital* (A/D) converters (Transmit/Receive) functionality and using microprocessors to handle the *Digital Signal Processing* (DSP) [34] The framework that interfaces the hardware to software has most frequently been handled through Windows-based MATLAB and Linux-based GNURadio (Windows version exists) libraries accessible on any PC [35]. This ease of functionality has been used in many microwave-radar based *Internet of Things* (IoT) applications seen in health, agricultural, and engineering disciplines which were reviewed in [36]. Often, attracting the attention of hobbyists, inspired to design simple microwave receivers capable of capturing transmitted frequencies within a specific bandwidth of interest. At its core, a microwave transmitter consists of a microwave oscillator where previously, the near-field microwave-based insect detection sensor centers on active resonators [26], which can be reconfigured into a self-sustaining oscillator; the foundational basis for antenna transmission design [37, 38]. As a result, highlights the potential of a continuously transmitted microwave oscillator signal perturbed by insect presence and movement to be received as a complex frequency by an SDR peripheral as an alternative portable insect detection system.

The complex nature of the insect frequency response is natural due to the movement within the close-to-surface detection range. Meaning, the insect position will be time dependent and may not always be in the strongest interaction region of the microwave resonant cavity.

Further, increasing the number of insects associated with an increase of material volume is an additional complexity. These issues must be considered when trying to extract any meaningful information of a signal that is not a simple *yes* or *no* detection result.

It is possible to capitalize on the motion detection capabilities of the microwave sensor by observing the dependent movement behaviour of a particular stored product insect pest species. Possibly, there are over 1 million insects on Earth, but out of the 32 classification orders, 3 *Coleoptera* (beetles), *Lipdoptera* (moths), and *Psocoptera* (booklice/mites) are post-harvest storage pests [39]. In Canada, the Canadian Grain Commission identifies 50 species (beetles, moths, and mites) as stored-product insect pests; some of the most common are the Red Flour Beetle (RFB) and Rusty Grain Beetle (RGB) [40]. The biological, physical, and ecological long-term movement of these insects is based on many factors: light, sound, temperature, humidity, behavioural, environmental, to name a few [41–46]. However, the short-term movement is difficult to observe in insects and yet to be classified; it has been suggested that the sustainable energy an organism can exert for prolonged duration to fatigue is known as the power-duration relationship or speed-duration relationship. It is a curvilinear function, first observed when predicting the speed of world-record marathon runners [47], but has also been reported in other animals (for review see: [48]). The power-law trend in different animals can be digested as follows: a fast phenotype animal may lack endurance, while an animal with an endurance phenotype may not be able to generate very high speed. Typically, models follow a hyperbolic law, but for long durations of activity ($>$ 15minutes) power-laws have performed much better [49]. In [50], athletic world records of speeds sustained for over a particular duration were modeled with a *fatigue factor* or reciprocal *endurance parameter*. In the case of RFB and RGB movement, a temperature stimulus applied to the microwave sensing region demonstrated induced insect movement observable by an activity signal response [26]. Although the activity signal was larger for the RFB insect, both species demonstrated heightened activity between 20^{o}C to 30^{o}C and lowered activity at very high and low temperatures although may be under-represented as a result of

poor dielectric and electric-field interactions within the large weak electric-field regions of the 26 mm diameter containment area. As it relates to the position-based time-dependent dielectric perturbation frequency response parameter that the insect induces, movement is a secondary parameter that must be considered when inferring information upon insect species and number. This movement or activity-duration relationship is critical in this study to classify the system response to highly active stimulated insect movement to unstimulated spontaneous-like fatigue movement patterns observed by the microwave sensor.

In this thesis, we seek to characterize and demonstrate the construction of an IDC microwave oscillator. Using the oscillator as a microwave-based sensor to be used in a transmitter and receiver configuration with a SDR HackRF One platform, we demonstrate the capability to detect common stored product RFB and RGB insects. Then, to increase selectivity, integrate the system with a probe trap to be used in a mock grain bin for a time-to-detection measurement, demonstrating the real-time detection ability of the insect detection system. Outside of grain, two boundaries: a small (sensitive) region encompassing only the IDC electrodes and a large (moderately-sensitive) region encompassing the IDC electrodes and weak electric-field regions around the IDC sensor are used to demonstrate that the choice of boundary affects the insect activity and frequency response. We first characterize the insect activity-duration relationship from stimulation, then a model is developed using the time-dependent frequency shift response and insect activity to differentiate between species and insect number. Then we determine which boundary produces the optimal comparison metrics between RFB and RGB and at what time from detection this comparison is most significant. This model aims to serve as a direction for others that can be further developed for in-grain use and other environmental factors.

2

Theoretical Background

The outline of this chapter, we first explore the theoretical framework for constructing a microwave sensor to be used in a portable insect detection system. We begin by addressing the impedance matching condition for the coplanar waveguide (CPW) the mechanism responsible for proper signal transmission. Following this, we delve into the interdigital capacitor (IDC) resonator design and explain how structural geometry affects capacitance (dielectric and electric-field) and limits the electric-field spatial and interdigital space distribution to the IDC surface at resonance. The time-dependent dielectric perturbation theory is then discussed, providing insight into how a resonant frequency responds to multiple moving insects. This is followed by an examination of two key microwave oscillator models—the feedback loop model and the negative resistance model—which help define the conditions required for stable oscillation. Finally, we detail the signal processing path through a Software Defined Radio (SDR) receiver, including quadrature demodulation, analog-to-digital (AD) conversion, and the application of the Fast Fourier Transform (FFT) algorithm to convert the discrete time-domain signal into a frequency-domain spectrum for insect detection.

2.1 Coplanar Waveguide (CPW) Transmission Line

In this thesis, the core foundation of our microwave sensor is based on the use of coplanar waveguide (CPW) transmission line geometry. CPW, like other transmission line geometries (e.g., microstrip, stripline, and slotline), is widely used in microwave circuit applications such as filters, amplifiers, antennas, and sensors. In general, the transmission lines' main purpose is to guide electromagnetic signals of a particular mode of propagation supported by either electric, magnetic, or electromagnetic transverse field propagation relative to the signal direction [51]. CPWs are particularly useful due to their ease of integration with active components, which will be discussed later on the topic of microwave oscillators. For now, we are concerned with designing a signal carrying structure to feed power into a microwave resonator for use as a sensor. Henceforth, for designing a CPW structure to acquire the desired characteristic impedance when interfacing with other microwave systems, we will be using the textbook knowledge [52] from *Coplanar waveguide circuits, components, and systems.*

There are two primary types of CPW: grounded and ungrounded, referring to the presence or absence of a ground plane on the bottom of the dielectric substrate. For our sensor, we use ungrounded CPW[1] transmission lines, its basic structure consists of a central conductor (signal line) separated from two ground planes by an air gap, all placed on the surface of a dielectric substrate. In Figure 2.1, the cross-sectional diagram of the CPW demonstrates the transverse electric- and magnetic-field distributions that permeate the dielectric substrate as the signal propagates along the central conductor. Since the electromagnetic-fields are not fully confined within a homogeneous dielectric material (with some fields residing in air), pure transverse electric- and magnetic-field (TEM) modes cannot be supported. This open structure complicates modal analysis due to phase mismatch at the air-dielectric interface [51]. The phase velocity in air is approximately $v_{ph} = c$, while in the dielectric it is approximately $v_{ph} = c/\sqrt{\epsilon_{eff}}$. For microwave wavelengths, their length is between 1 m to 1 mm, where a

[1] CPW is assumed to be ungrounded

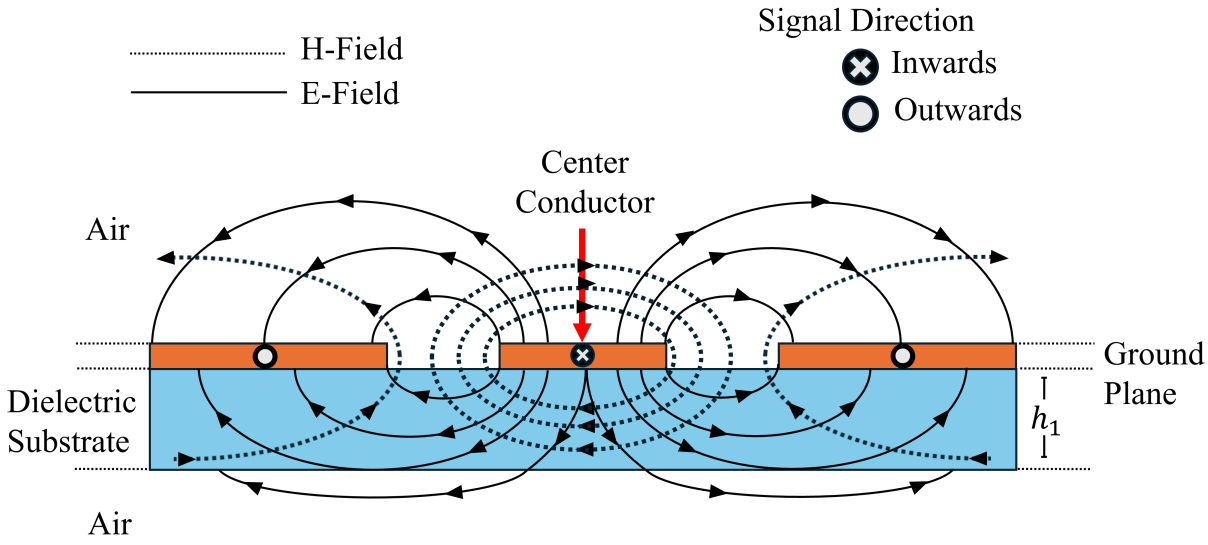


Figure 2.1: Ungrounded CPW EM-Field Distribution. A cross-sectional diagram of the Ungrounded CPW transmission line structure with electric (E)- and magnetic (H)- Field distribution about the signal line propagation.

1 GHz microwave corresponds to $\lambda_{1GHz} = 30$ cm. However, when the substrate height h_1 is much smaller than the wavelength λ traveling along the conductor ($h_1 \ll \lambda$), the fields can be considered static, and the mode supported is called the quasi-static TEM mode. A CPW transmission line primarily supports a quasi-TEM mode, where the electric and magnetic fields are mainly confined between the central conductor and the ground planes. For a signal propagating inwards Figure 2.1, the magnetic (H)-field circulates clockwise around the signal line, and the electric (E)-field extends radially from the signal line to the ground plane, refracted and condensed in the substrate, with some fringing fields extending into the air above and below the substrate. Secondary magnetic-fields are generated by edge currents along the ground plane, propagating in the opposite direction to the signal. Like other transmission lines, the geometric dimensions of the CPW determine the electric- and magnetic-field distributions, which influence the effective dielectric constant and impedance of the conductor—two key factors for optimal power transfer when interfacing with coaxial cables, amplifiers, antennas, and measurement systems.

For design purposes, it is crucial to understand the effective dielectric constant ϵ_{eff} and

characteristic impedance Z_o which are related via phase velocity and capacitance (C_{CPW}) of the CPW structure $Z_o = 1/C_{CPW}v_{ph}$. The effective dielectric constant accounts for the fraction of the electric-field in both the dielectric substrate (ϵ_1) and the surrounding air (ϵ_0). A method used to determine ϵ_{eff} and Z_o transforms the complex CPW geometry to distinct regions of parallel plate capacitors to derive simpler analytical expressions, known as conformal mapping.

Figure 2.2 shows three distinct regions of isotropic dielectric substrates. The conductors of the CPW are encased vertically between the dielectric substrates with magnetic wall conductors along the dielectric boundaries. The ground planes are separated by a distance s_{TL} from the center conductor of width w_{TL}. All conductors are assumed to have negligible thickness ($t \to 0$) and perfect conductivity.

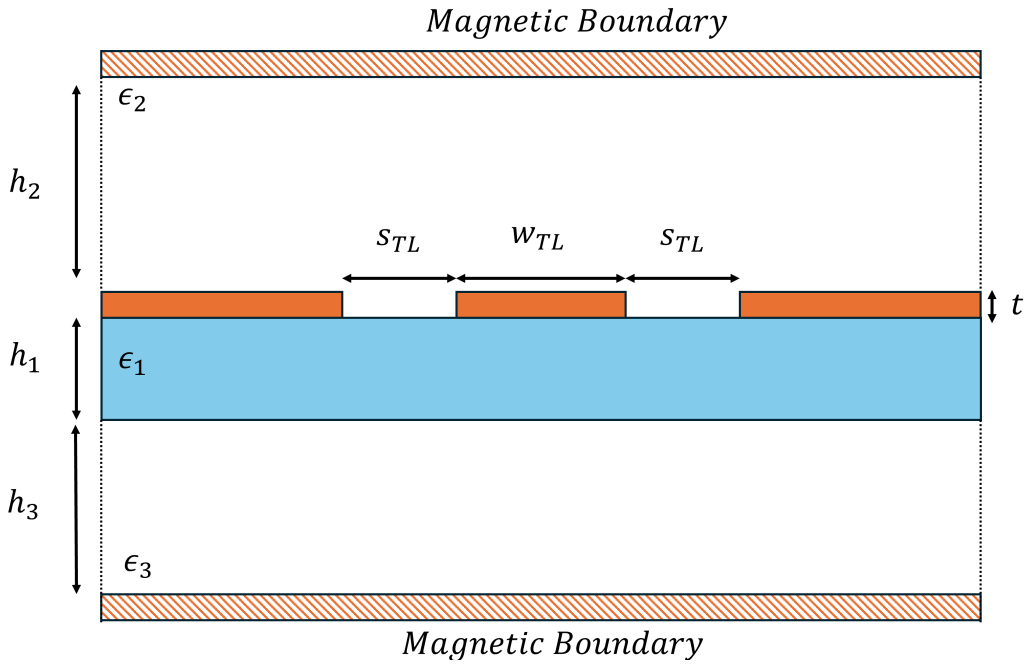


Figure 2.2: CPW Dielectric Regions. A cross-sectional diagram of the Ungrounded CPW transmission with three dielectric regions confined by a magnetic boundary line.

The total capacitance C_{CPW} is the sum of the partial capacitances in the upper dielectric region (ϵ_2) and the lower dielectric region (ϵ_3 and ϵ_1). For a finite dielectric substrate (ϵ_1)

suspended in air ($h_2 = h_3 \to \infty$, $\epsilon_2 = \epsilon_3 = \epsilon_o$), the total capacitance is given by:

$$C_{CPW} = C_{\epsilon_1} + C_{\text{air}} \tag{2.1}$$

where C_{ϵ_1} is the capacitance due to the dielectric substrate and C_{air} is the capacitance due to the electric-fields in the air. This leads to an effective dielectric constant:

$$\epsilon_{\text{eff}} = \frac{C_{CPW}}{C_{\text{air}}} = 1 + \frac{\epsilon_1 - 1}{2} \frac{K(k_1)K(k_0')}{K(k_1')K(k_0)}. \tag{2.2}$$

The characteristic impedance is:

$$Z_0 = \frac{30\pi}{\sqrt{\epsilon_{\text{eff}}}} \frac{K(k_0')}{K(k_0)} [\Omega]. \tag{2.3}$$

The effective dielectric constant and the characteristic impedance are functions of complete elliptical integrals of the first kind $K(k)$, with k_0 and k_1 being the moduli of $K(k_0)$ and $K(k_1)$, respectively. The geometrical relationships are given by:

$$k_0 = \frac{s_{TL}}{s_{TL} + 2w_{TL}}, \tag{2.4}$$

$$k_1 = \frac{\sinh\left(\frac{\pi s_{TL}}{4h}\right)}{\sinh\left(\frac{\pi(s_{TL}+2w_{TL})}{4h_1}\right)}, \tag{2.5}$$

$$k_1' = \sqrt{1 - k_1^2}, \tag{2.6}$$

$$k_0' = k_1'. \tag{2.7}$$

This equation is accurate within a few percent depending on the shape ratio $w_{TL}/(2s_{TL} - w_{TL})$ when compared at 1 GHz with the spectral domain technique [53]. A frequency dispersion and copper cladding thickness correction factor can be applied to further refine impedance matching [52]. However, for the purpose of this thesis, a rough design with $Z_0 \approx 50\,\Omega$ is sufficient to interface with port-matched microwave circuits and measurement equipment.

2.2 IDC Resonant Frequency

Microwave resonators are essential components in RF and microwave circuits, commonly used in filtering and sensing applications. Depending on the CPW mechanism, the resonator can act as a stop-band or pass-band filter. Metallic cavities store electromagnetic energy in their electric- and magnetic-fields at specific frequencies, forming standing waves determined by the cavity's physical dimensions and boundary conditions. This is called the resonance frequency.

Resonator behaviour can be modelled using basic lumped circuit elements such as inductors and capacitors, simplifying the design for specific frequencies and geometries [51]. For a simple LC tank circuit, the resonant frequency is given by the lumped inductance L and capacitance C:

$$f_r = \frac{1}{2\pi\sqrt{LC}}. \tag{2.8}$$

Capacitance C is the critical element in microwave sensors, since $C \propto \epsilon$, ϵ being the dielectric material constant responsible for dielectric perturbations, we will discuss this further below. A change in C leads to a change in the resonant frequency f_r. When an MUT is in contact with an open capacitive element, the total capacitance is the parallel combination of the circuit capacitance C and the MUT capacitance C_{MUT} [32]:

$$f_r = \frac{1}{2\pi\sqrt{L(C + C_{MUT})}} \tag{2.9}$$

Sensing using an interdigital capacitor (IDC) resonator can produce strong capacitive effects confined to the planar surface. An IDC resonator consists of multiple parallel electrodes, creating a strong localized electric-field between them. To describe the capacitance C of the resonator, a conformal mapping technique is used to analyze the unit cell capacitance [54]:

$$C_{UC} = C_1 + C_2 + C_3 \tag{2.10}$$

Here, C_1, C_2, and C_3 represent the capacitances in the dielectric regions: directly between the electrodes (ϵ_1), above the electrodes (ϵ_2), and below the electrodes (ϵ_3) Figure 2.3(a). The cross-section of the unit cell has length l_{UC}, electrode spacing w_g, and height t_f. The capacitances $C_2 + C_3$ are modelled as two plate capacitors, while C_1 is modelled as a simple one-dimensional plate capacitor. Figure 2.3(a), regions (2) and (3) correspond to air ($\epsilon_2 = \epsilon_0$) and the substrate ($\epsilon_3 = \epsilon_r$), respectively, with gaps filled by air ($\epsilon_1 = \epsilon_0$). The total capacitance of the unit cell is:

$$C_{UC} = \left[\frac{\epsilon_0(1-\epsilon_r)}{2}\frac{K(k')}{K(k)} + \frac{\epsilon_0 t_f}{w_g}\right] \tag{2.11}$$

where ϵ_r is the dielectric constant of the substrate, $k = \frac{l_{UC}}{w_g}$, and K is the complete elliptic integral of the first kind.

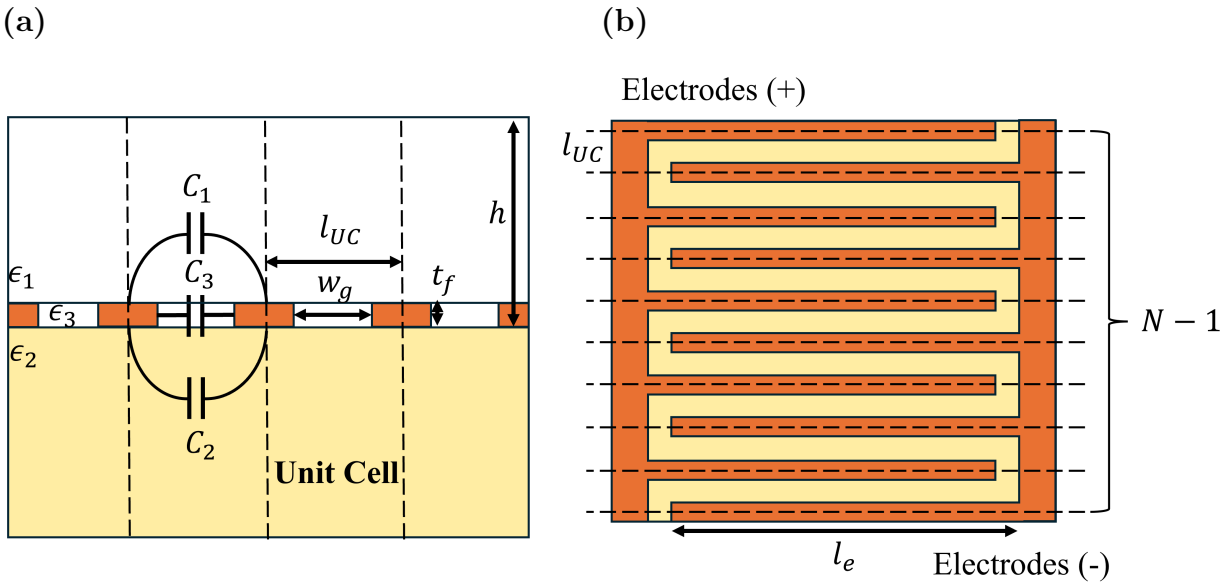


Figure 2.3: IDC Structure. (a) Cross-section of unit cell IDC structure in 3 dielectric regions. (b) Top-view of IDC resonator with N electrodes and $N-1$ unit cells.

For multiple electrodes, the total capacitance is:

$$C = C_{UC}(N-1)l_f \tag{2.12}$$

where N is the number of electrodes, and l_f is the electrode length Figure 2.3(b). Thus, more electrodes increase the capacitance and interactions with the MUT.

It has been experimentally verified that C_1 saturates at 99.5% of its maximum value at a height t_s [55], which scales with the unit cell spacing $l_{UC} = w_g + w_f$ as:

$$t_s = -\frac{w_g + w_f}{d_2(w_g)} \ln\left(\frac{0.005}{d_1(w_g)}\right) \tag{2.13}$$

where d_1 and d_2 are coefficients fitted to third-order polynomials as functions of w_g and electrode width w_f. The cartoon in Figure 2.4(a) illustrates that the electric field lines between parallel plate capacitors are perpendicular within an MUT. When the plates are open-faced parallel (electrodes) to each other, the electric-field lines extend to a height limited by t_s. For narrow spacing, the electric-field lines are confined within the MUT Figure 2.4(b), but for wide spacing, the electric-field lines extend beyond the MUT Figure 2.4(d). The electrode spacing that extends from narrow to wide results in an increase in the electric-field saturation height for a set electrode width Figure 2.4(c). This electric-field height extension is undesirable for contact sensing; specifically, insects are very small and reside on the surface of the sensor; hence a narrow electrode spacing is desirable for greater insect (MUT) and electric-field interaction.

2.2.1 CPW-Backed IDC Resonator

The designed microwave resonator uses a pass-band CPW configuration, with a series capacitive gap along the centre of the signal line and the IDC resonator placed directly beneath the capacitive gap. The CPW acts as a feedline, providing an input and output path for the energy stored in the resonator. The electromagnetic field lines of the quasi-TEM mode for a signal propagating along the CPW transmission lines are coupled magnetically and electrically into the IDC resonator near and at the resonance frequency. Typically, the circuit form of magnetic coupling and electrical coupling is done via mutual inductance and a capacitor, respectively. However, deriving an equivalent circuit model can be challenging

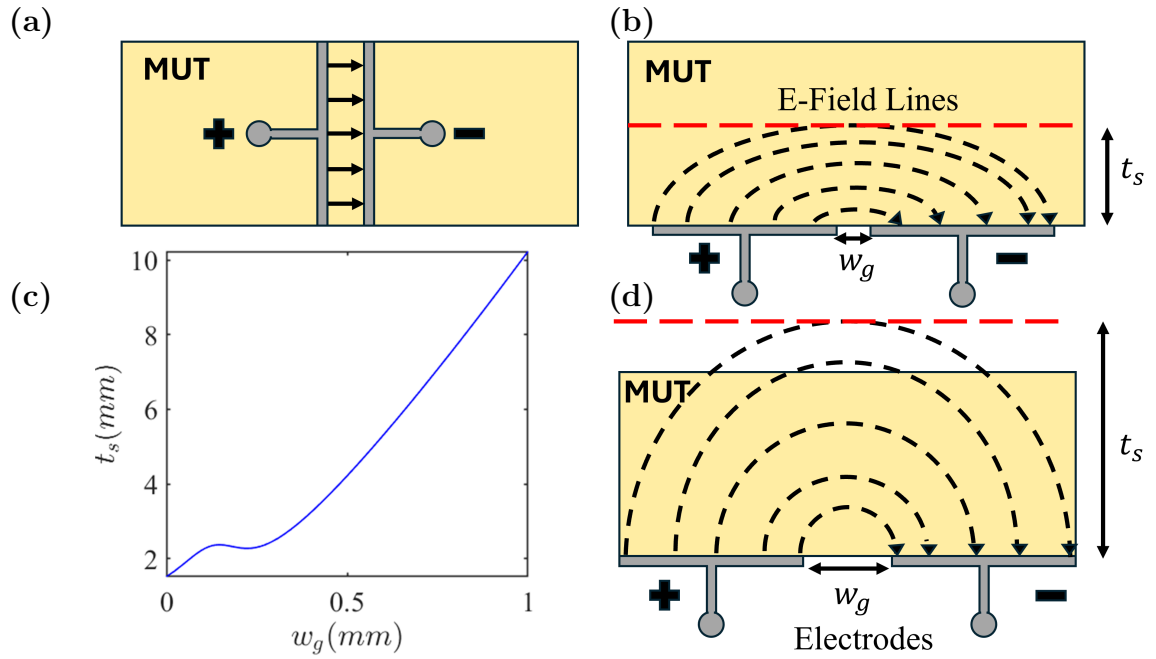


Figure 2.4: MUT and C_1 Sensitivity. (a) MUT with permeated electric field lines of parallel plate capacitor. (b) Open-plate capacitor with narrow electrode spacing w_g. (c) Open-plate capacitor with wide electrode spacing w_g. Extended E-Field lines with saturation height t_s (red-dotted line) permeate MUT. (d) C_1 99.5% saturation value of height t_s as a function of electrode spacing with $w_f = 0.5mm$.

for most planar resonator designs due to the unknown series or parallel RLC configuration of the IDC resonator. Therefore, often designers will verify the resonance frequency using EM simulation software tools (see Chapter 3). As of this thesis, the CPW-backed IDC resonator does not have a complete equivalent circuit model and relies on EM simulators to design and discern the resonant structure and frequency.

Nevertheless, in microwave sensing, apart from the resonant frequency, optimal power transfer from the CPW feedline is crucial, as it directly influences the measured quality factor (Q) of the system. Maximum power transfer is achieved when the feedline is impedance-matched to the resonator [51], termed critical coupling, defined by the coupling coefficient g:

$$g = \frac{Q_o}{Q_e} \tag{2.14}$$

where Q_o is the resonator's intrinsic quality factor, and Q_e is the external quality factor from the CPW feedline. The quality factor relates to the damping of the circuit:

$$Q = \frac{\text{Stored Energy}}{\text{Dissipated Energy}} \tag{2.15}$$

When the circuit is loaded by the CPW feedline, additional losses occur. The coupling condition is categorized as over-coupled ($g > 1$), under-coupled ($g < 1$), or critically coupled ($g = 1$). Depending on the RLC configuration, the coupling coefficient is:

$$g = \frac{Z_0}{R} \quad \text{(series)}, \quad g = \frac{R}{Z_0} \quad \text{(parallel)} \tag{2.16}$$

where R is the resistance of the RLC circuit. The coupling effect can be observed in the loaded quality factor Q_L:

$$Q_L = \frac{Q_o}{(1+g)} \tag{2.17}$$

In measurement systems, Q_L is determined by the bandwidth around the peak of the resonant distribution:

$$Q_L = \frac{f_r}{BW} \tag{2.18}$$

where BW is the full width at half maximum of the frequency distribution, or Δf_{3dB} measured 3dB from the peak in a decibel scale centered around the resonant frequency. As the measured bandwidth decreases, the frequency resolution improves and higher Q_L results in easier detection of small frequency deviations, making a narrow bandwidth or high Q desirable for microwave sensing.

2.3 Dielectric Perturbation for Microwave-Based Sensors

The fundamental concept behind the construction of microwave-based sensors involves material or cavity perturbations. For insect detection, material perturbations are sufficient. It is

assumed that the introduction of a small dielectric object into a cavity will not significantly alter the original field properties.

2.3.1 Dielectric Perturbation

Consider a microwave cavity Figure 2.5(a) characterized by electric- and magnetic-fields E_o and H_o, with material constants for permittivity (ϵ) and permeability (μ of free space, confined within a volume V_o. A material perturbation of equal volume $V_1 = V_o$, permittivity ϵ_1, and permeability μ_1 induces new fields E_1 and H_1 within a perturbed cavity Figure 2.5(b). Maxwell's equations for the original and perturbed cavities are:

$$\nabla \times \vec{E}_o = -j\omega_o \mu \vec{H}_o, \tag{2.19}$$

$$\nabla \times \vec{H}_o = j\omega_o \epsilon \vec{E}_o, \tag{2.20}$$

$$\nabla \times \vec{E}_1 = -j\omega_1 (\mu + \Delta\mu) \vec{H}_1, \tag{2.21}$$

$$\nabla \times \vec{H}_1 = j\omega_1 (\epsilon + \Delta\epsilon) \vec{E}_1, \tag{2.22}$$

where $\omega_r = \omega_o$ is the angular resonant frequency of the original cavity, ω_1 is the angular resonant frequency of the perturbed cavity, $\Delta\epsilon = \epsilon_1 - \epsilon$ is the dielectric perturbation, and $\Delta\mu = \mu_1 - \mu$ is the magnetic perturbation. The following assumptions are made: 1. The original cavity is lossless. 2. The sample volume is much smaller than the cavity volume. 3. The electric and magnetic fields remain unchanged outside the boundary of the sample.

Using the procedure from *Microwave Electronics* [56], the fractional frequency shift for a small material perturbation is given by:

$$\frac{\omega_1 - \omega_o}{\omega_o} \approx \frac{-\int_{V_1} (\Delta\epsilon \vec{E}_o^* \cdot \vec{E}_1 + \Delta\mu \vec{H}_o^* \cdot \vec{H}_1) dV}{\int_{V_o} (\epsilon \vec{E}_o^* \cdot \vec{E}_1 + \mu \vec{H}_o^* \cdot \vec{H}_1) dV}. \tag{2.23}$$

Since the perturbation occurs in air, which can be approximated as a vacuum ($\epsilon \approx \epsilon_o$ and $\mu \approx \mu_o$), and the resonant frequency is generally complex, the complex frequency shift $\Delta\tilde{\omega} = \tilde{\omega}_1 - \tilde{\omega}_o$ is defined as $\tilde{\omega}_o = \omega_o + j\omega_o\zeta$, where $\zeta = 1/2Q_o$ is the damping ratio related to

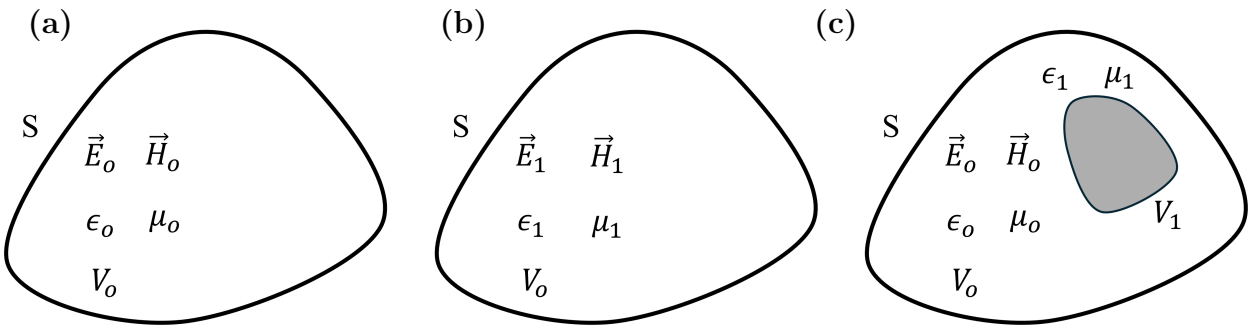


Figure 2.5: Dielectric Perturbation of Microwave Cavity (a) Original cavity.(b) Full-volume dielectric perturbed cavity (c) Small-volume dielectric perturbed cavity

the Quality-factor Q_o of the original cavity. The permittivity ϵ is also complex, expressed as $\tilde{\epsilon}/\epsilon_o = \tilde{\epsilon}_r = \epsilon_r' + j\epsilon_r''$.

For a small dielectric perturbation Figure 2.5(c) ($\Delta\mu = 0$) and assuming $V_1 \ll V_o$, the expression simplifies to:

$$\frac{\tilde{\omega}_1 - \tilde{\omega}_o}{\tilde{\omega}_o} \approx -\frac{\tilde{\epsilon}_r - 1}{2} \frac{\int_{V_1} \vec{E}_o^* \cdot \vec{E}_1 dV}{\int_{V_o} |\vec{E}_o|^2 dV} \tag{2.24}$$

$$\frac{\tilde{\omega}_1 - \tilde{\omega}_o}{\tilde{\omega}_o} \approx \left(\frac{f_1 - f_o}{f_o}\right) + \frac{j}{2}\left(\frac{1}{Q_1} - \frac{1}{Q_o}\right) \tag{2.25}$$

where f_o, f_1, and Q_1 is the resonant frequency of the original cavity, perturbed cavity, and Q-factor of the perturbed cavity. The following assumption is made: $\mathrm{Re}(\tilde{\omega}_1) \approx \mathrm{Re}(\tilde{\omega}_o)$, $\mathrm{Im}(\tilde{\omega}_1, \tilde{\omega}_o) \gg \mathrm{Re}(\tilde{\omega}_1, \tilde{\omega}_o)$, and $Q_o \gg 1$. Combining the real and imaginary parts, the shift in frequency and quality factor due to a small cavity perturbation becomes:

$$\Delta f = -A f_o(\epsilon_r' - 1)\frac{V_1}{V_o} \tag{2.26}$$

$$\Delta Q = -2Q_1 Q_o A \epsilon_r'' \frac{V_1}{V_o} \tag{2.27}$$

where A is the form factor, related to the shape and location of the sample inside the cavity:

$$A = \frac{V_o}{2V_1} \frac{\int_{V_1} \vec{E}_o^* \cdot \vec{E}_1 dV}{\int_{V_o} |\vec{E}_o|^2 dV} \tag{2.28}$$

For a uniform electric-field ($\vec{E}_1 \approx \vec{E}_o$), $A = 1$, but for a non-uniform field, $\vec{E}_1 \neq \vec{E}_o$, making the form factor dependent on the position of the maximum field.

2.3.2 Insect Detection using Δf

In insect detection, the dielectric perturbation for a single dielectric inclusion (insect) is positionally and temporally dependent meaning that the form factor $A(\vec{x}, t)$ is as well which directly influences frequency shift:

$$\Delta f(\vec{x}, t) = f_1(\vec{x}, t) - f_o. \tag{2.29}$$

Assuming multiple moving insects in Figure 2.6 of identical volume V_1 of a given species, the total volume is $V_1 = MV_{\text{In}}$, where M is the number of insects and V_{In} is the volume of an individual insect. Taking $\epsilon_1' = \epsilon_{\text{In}}'$ as the dielectric constant of the insect species, the approximate linear relationship between frequency shift and insect number is:

$$\Delta f(t) \approx -f_o(\epsilon_{\text{In}}' - 1)M\frac{V_{\text{In}}}{V_o}A(t). \tag{2.30}$$

For a simpler notation, we omit $\vec{x}$ since the form factor depends on the position of multiple insects, and in general we are only aware that the insect(s) are within the microwave cavity and not what their specific position(s) are.

The shift in ΔQ due to the lossy ϵ_r'' component can be treated similarly, but changes in Q_1 for a given resonator and insect number are more complex. As we will see in the next section, moving from a passive resonator to an active device (microwave oscillator) complicates the analysis of Q_1, and thus ΔQ is not used for insect quantification.

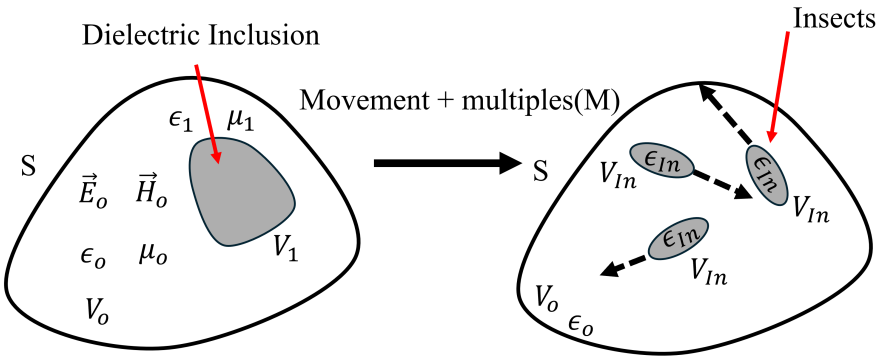


Figure 2.6: Microwave Cavity Dielectric Perturbation from Moving Insects. Microwave cavity with original dielectric perturbation for moving dielectric inclusions of same shape, volume and dielectric constant for multiple identical insects

2.4 Microwave Oscillator Models

Microwave oscillators are generally described by two main models: the Feedback Model and the Negative Resistance Model. The choice between these models depends largely on the construction and configuration of the oscillator. The Feedback Model is easier to interpret for general systems but is often mathematically arbitrary. On the other hand, when circuit components are known, the Negative Resistance Model is preferred, as it offers a more technical and detailed understanding. Since this thesis uses a complex configuration of a microwave oscillator that can be simplified into an LC tank circuit, both models will be explained.

2.4.1 Laplace Analysis and Stability

Most transistor oscillator systems are governed by non-linear differential equations. However, for oscillator design, it is more convenient to analyze a linear time-invariant system and examine stability at points in time. To do this, we use the Laplace transformation, which converts a differential equation in the time domain to an algebraic equation in the complex frequency domain (s-plane):

$$\mathcal{L}\{x(t)\} = F(s) = \frac{N(s)}{D(s)}. \tag{2.31}$$

where $F(s)$ is the transfer function, consisting of polynomials: $N(s)$ and $D(s)$. The zeros and poles of $F(s)$ fully describe the dynamic response of the system $x(t) = \sum_{i=0}^{n} C_i e^{\lambda_i t}$ where C_i is determined by the initial conditions, and λ_i are the roots of the characteristic equation $D(s) = 0$. The poles $p_i = \lambda_i$ represent the system's eigenvalues, indicating finite gain. Whereas zeros correspond to null gain for any given input.

For near-sinusoidal self-sustaining oscillators, $F(s)$ must have a pair of complex-conjugate poles $P(p_1, p_2) = \alpha \pm j\beta$ located in the right-hand plane (RHP) of the s-plane [37]. For an arbitrary input at these RHP poles, results in an exponentially growing sinusoid:

$$x(t) = X_o e^{\alpha t} \cos(\beta t). \tag{2.32}$$

Here, X_o represents the initial condition at startup. However, this exponential growth is physically unrealistic, so inherent non-linearities of the active components stabilize the output over time.

2.4.2 Feedback Model

The Feedback Model (Figure 2.7) is constructed using an amplifier with open-loop gain $A(s)$ and a frequency-selective network with feedback factor $H(s)$. These are connected in a positive feedback loop. The input signal $x_i(s)$ is summed with the source signal $x_s(s)$ and the feedback signal $x_f(s)$. After being amplified and undergoing a π-phase shift, the output $x_o(s)$

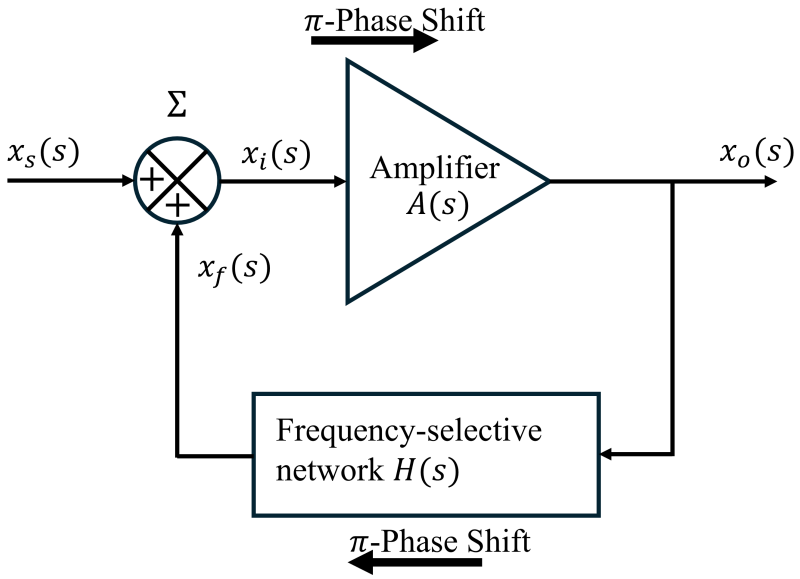


Figure 2.7: Feedback Loop Model. Two-port feedback model composed of an Amplifier $A(s)$ and Frequency Selective Network $H(s)$.

is fed back through $H(s)$, undergoing another π-phase shift. This phase matching condition ensures constructive interference at the resonant frequency ω_o.

The closed-loop transfer function is given by:

$$A_f(s) = \frac{A(s)}{1 - T(s)} \tag{2.33}$$

where $T(s) = A(s)H(s)$ is the loop gain, and $A_f(s) = \frac{x_o(s)}{x_s(s)}$. For zero input and non-zero output ($x_s = 0$, $x_o \neq 0$), $A_f(s) \to \infty$. Oscillations occur at the frequency $\omega = \omega_o$, determined by the frequency-selective network and the phase matching condition. The characteristic equation is $1 - T(s) = 0$. Then the oscillation condition is met when the phase of the loop gain is zero and the magnitude is unity, known as the Barkhausen criterion [37]:

$$\text{Arg}(T(j\omega_o)) = 0 \tag{2.34}$$

$$|T(j\omega_o)| = 1 \tag{2.35}$$

Referring to Equation 2.32, if the poles are not on the $j\omega$ axis, the signal decays in the left-hand plane (LHP) or grows in the RHP. During start-up, the loop gain is greater than

unity, in the RHP, causing the oscillation to grow until non-linearities stabilize the poles on the $j\omega$ axis, achieving steady oscillation due to the active components of the amplifier [57].

2.4.3 Negative Resistance Model

The Negative Resistance Model is another approach to analyzing microwave oscillators, particularly when circuit components are known. Using a one-port model design criteria [58], the input impedance of the active circuitry (Amplifier) of Figure 2.8 is represented as:

$$Z_A(I,s) = R_A(I,s) + jX_A(I,s) \tag{2.36}$$

where $Z_A(I,s)$ depends on the steady-state current I and the complex frequency s. Similarly, the input impedance of the frequency-selective circuit (Network) is:

$$Z_H(s) = R_H(s) + jX_H(s). \tag{2.37}$$

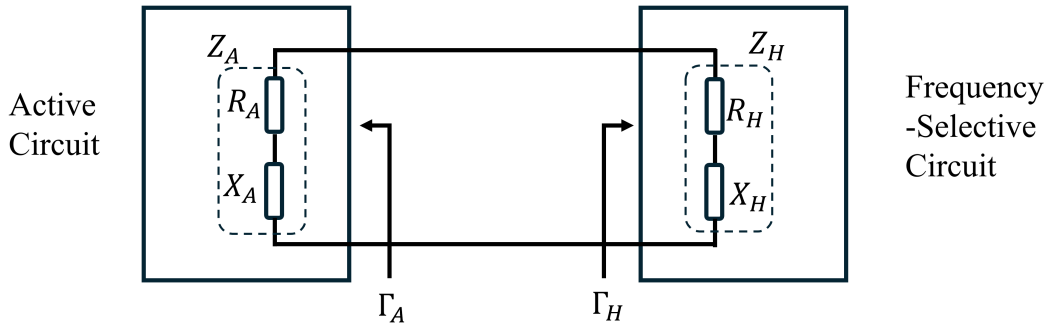


Figure 2.8: Negative Resistance Model. One-port negative resistance model of an Active Circuit (Amplifier) and Frequency-selective Circuit (Network) decomposed into their impedances.

To produce voltage oscillations ($V_o \neq 0$) with zero input ($V_{\text{in}} = 0$), the current I must be non-zero. Consider a series RLC circuit composed of the active and frequency-selective circuitry, with total impedance:

$$Z_T = (R_T + jX_T) = 0 \tag{2.38}$$

where $R_T = R_H + R_A^L$ and $X_T = sL_T + \frac{1}{sC_T}$. Here R_A^L is the linear component of the "non-linear" resistance R_A of the amplifier. A non-zero current $I(s)$ produces the characteristic equation:

$$s^2 L_T C_T + sC_T R_T + 1 = 0 \tag{2.39}$$

This results in a pair of complex-conjugate poles:

$$s_{p_1, p_1^*} = \zeta\omega_x \pm j\omega_x\sqrt{1-\zeta^2} \tag{2.40}$$

where $\zeta = -\frac{R_T C_T}{2\omega_x}$ is the damping ratio. $\omega_x = \frac{1}{\sqrt{L_T C_T}}$ is the natural frequency that, for high-Q oscillators $\omega_x \to \omega_o$, and the oscillation frequency determined by the frequency-selective circuit [59]. For oscillations to begin, we require $\zeta > 0$ and $R_T < 0$. This condition can be satisfied if $R_H > 0$ and $|R_A^L| > |R_H|$, which means that the active circuit provides negative resistance at startup to compensate for the losses of the passive resonator. At steady-state oscillation, the impedances are complex conjugates of one another $Z_A = Z_H^*$ and the oscillation condition is then:

$$R_H(s) - R_A(I, s) = 0 \tag{2.41}$$

$$X_H(s) + X_A(I, s) = 0. \tag{2.42}$$

Here, Equation 2.42 is the phase matching condition of Equation 2.34. When defined using the reflection coefficients Γ at the active and frequency-selective circuit interfaces $\Gamma = \frac{Z - Z_o}{Z + Z_o}$ resembles Equation 2.35 by taking the product of the reflection coefficients:

$$|\Gamma_A \Gamma_H| = 1. \tag{2.43}$$

If the one-port system was configured as a parallel RLC circuit, then the same form would hold for the total admittance [57].

2.4.4 Application to Insect Detection

For the insect detection system, the goal is to achieve a stable oscillation at the frequency $f_o = \frac{\omega_o}{2\pi}$. Consider in terms of power transfer between the active circuit and the frequency-selective circuit using Equations 2.16 and 2.17 regardless of the RLC configuration. Here, the impedance magnitude is $Z_o = |\Re(Z_A)| = R_A$, therefore, for sustained oscillations $g = 1$ and the oscillator is critically coupled. This corresponds to a $Q_L = 0.5Q_o$ which is the minimum noise about the oscillator signal.

Hence, we wish to measure the output power when the signal has stable oscillation output power and low noise:

$$P_{\text{out}} = \frac{V_{\text{o}}^2}{2Z_0} \tag{2.44}$$

or in decibels:

$$P_{\text{dBm}} = 10\log_{10}\left(\frac{P_{\text{out}}}{1\,\text{mW}}\right). \tag{2.45}$$

A stable output power P_{out} at a defined oscillation frequency f_o of this microwave sensor when used in conjunction with Equation 2.30 demonstrates the ability of this microwave sensor configuration to be used for insect detection. To use in the field, the next section will describe utilizing an SDR to determine the frequency content of our sensor.

2.5 Analog-to-Digital Signals in RF Systems

SDRs can be used as a wide-band receiver that digitizes an analog signal and can then be recorded or displayed using a CPU. When used together with the microwave sensor, we have a field-capable insect detection system. The analog-to-digital signal path will be demonstrated using quadrature demodulation, which can in turn be displayed as a frequency domain spectrum transformed from the original digitized time domain signal using the Fast

Fourier Transform (FFT) basics. In this section, we utilize digital signal processing knowledge from [60].

2.5.1 Quadrature Demodulation

Consider an RF signal composed of many frequencies over a limited bandwidth:

$$x_{\mathrm{RF}}(t) = \sum_{l} X_l \cos(2\pi f_l t + \phi_l) \tag{2.46}$$

where X_l is the amplitude of a given frequency f_l, and ϕ_l is the phase offset within the bandwidth of interest. The $x_{RF}(t)$ path from a continuous analog signal to discrete digital time domain signal follows Figure 2.9. A local oscillator with frequency f_c, the centre frequency of the bandwidth, is split into two sinusoidal signals with a 90° relative phase offset. The RF signal is also split and mixed (multiplied) with the local oscillator signals, producing a base-band frequency of:

$$x_{\mathrm{BB}}(t) = \begin{cases} x_I(t) = x_{\mathrm{RF}}(t)\cos(2\pi f_c t) \\ x_Q(t) = -x_{\mathrm{RF}}(t)\sin(2\pi f_c t) \end{cases} \tag{2.47}$$

The trigonometric multiplication of the local oscillator and RF signals produces frequencies $|f_l - f_c|$ and $|f_l + f_c|$. Frequencies $f_l + f_c$ are undesirable, so the additive frequencies are filtered at a low cutoff frequency f_{cut} using a low-pass filter $H_{\mathrm{LPF}}(f_{\mathrm{cut}})$:

$$x(t) = \begin{cases} I(t) = H_{\mathrm{LPF}}(f_{\mathrm{cut}})[x_{\mathrm{RF}}(t)\cos(2\pi f_c t)] \\ Q(t) = -H_{\mathrm{LPF}}(f_{\mathrm{cut}})[x_{\mathrm{RF}}(t)\sin(2\pi f_c t)] \end{cases} \tag{2.48}$$

Thus, the filtered base-band analog signal can be written in its complex form:

$$x(t) = I(t) + jQ(t) \tag{2.49}$$

where $I(t)$ is the In-phase signal, and $Q(t)$ is the Quadrature signal (90° phase-shifted signal). The process of taking the RF signal and separating it into I and Q baseband components is

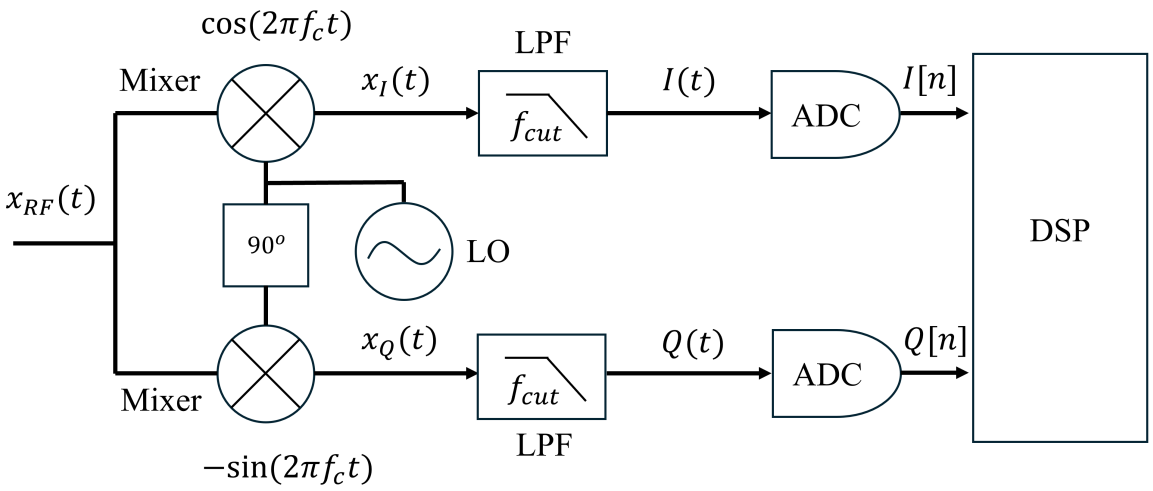


Figure 2.9: Analog-to-Digital Path using Quadrature Demodulation. Analog-to-Digital RF signal path separated into discrete I/Q samples to be processed by DSP block.

called *Quadrature Demodulation*, and it is the primary function of an RF tuner in a receiver system [61] Figure 2.9. This process is the foundation of many SDRs, which will be used in the portable insect detection system explained in Chapter 3. To transition from continuous time to discrete time, the Analog-to-Digital converter (ADC) digitizes the I/Q components, which are sampled at a specified frequency f_s, known as the sampling rate Figure 2.9. This results in a discrete sequence of complex samples:

$$x[n] = I[n] + jQ[n] = x(nT_s) \tag{2.50}$$

where n is the sample index, $n \in [0, N-1]$, N is the number of samples, and $T_s = f_s^{-1}$ is the sampling time interval. $I[n]$ and $Q[n]$ are the In-phase and Quadrature sequences at sample index n. From which, the digitized I/Q samples can then be used for *Digital Signal Processing* (DSP) performing the real-time data analysis for the portable insect detection system.

2.5.2 Discrete Fourier Transform and Fast Fourier Transform

Now that we have the discretized/digitized I/Q samples, we can convert them from the time domain to the frequency domain using the Discrete Fourier Transform (DFT). For N discrete-time samples of $x(nT_s)$, the DFT is given by:

$$X[k] = \sum_{n=0}^{N-1} x[n] e^{-j\frac{2\pi kn}{N}} \tag{2.51}$$

where $X[k]$ is the sequence of DFT coefficients, and k represents the frequency bin number of the DFT coefficient. For each frequency bin k, $X[k]$ describes the magnitude and phase for $k = 0, 1, \ldots, N-1$ in the frequency domain, with the frequencies for certain k as:

$$f_k = \frac{k f_s}{N} \tag{2.52}$$

The computation time of the DFT is directly related to the number of multiplications, which is proportional to N^2. To improve efficiency, the DFT can be re-written as:

$$X[k] = \sum_{n=0}^{N-1} x[n] W_N^{nk}, \quad W_N^{nk} = e^{-j\frac{2\pi kn}{N}} \tag{2.53}$$

Throughout the calculations, W_N^{nk} is recalculated multiple times for different combinations of n and k and is periodic for values of N. This allows the DFT to be divided into even and odd sequences:

$$X[k] = X_{\text{even}}[k] + W_N^k X_{\text{odd}}[k] \tag{2.54}$$

The sequences $X_{\text{even}}[k]$ and $X_{\text{odd}}[k]$ can be recursively split into $N/2$ point transformations until $N = 2$. This forms the basis of the Fast Fourier Transform (FFT), which reduces complex multiplications from N^2 (DFT) to $N/2 \log_2(N)$ (FFT) and reduces complex additions from $N(N-1)$ (DFT) to $N \log_2(N)$ (FFT) [60].

2.5.3 Digital Frequency Spectrum

When applying the FFT to a discrete time-domain sequence of N samples, a discrete frequency sequence with k frequency bins is produced. The term W_N^{nk} generates positive frequencies f_k for $k \in [0, N/2)$, where $k = 0$ is the DC component, and negative frequencies for $k \in [N/2, N-1]$, where $k = N/2$ corresponds to the frequency bin at the Nyquist sampling frequency $f_k = f_s/2$ (Figure 2.10(a)). The maximum frequency content in the signal is limited by the condition $f_s \geq 2f_{\max}$, and any sampling rate lower than $2f_{\max}$ will result in aliasing of higher frequency components, distorting the FFT signal. Reordering the spectrum around the centre of the DC component, with negative frequencies below and positive frequencies above the DC frequency, is performed using an FFT index shift operation (FFT-shift) (Figure 2.10(b)). Observing the frequency domain spectrum, for complex signals, unlike real signals, the magnitude $|X[k]|$ exhibits asymmetry around the DC centre. The bandwidth is f_s, with a frequency spacing of $\Delta a = \frac{f_s}{N}$ and a span of $[-f_s/2, f_s/2]$ for large N.

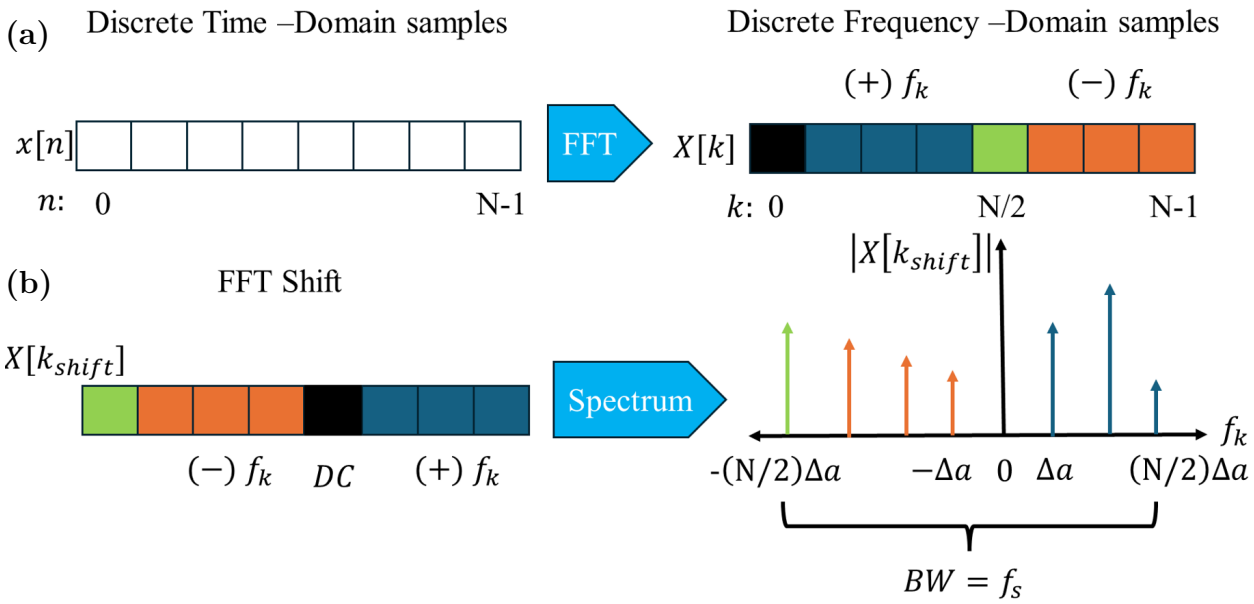


Figure 2.10: Fast Fourier Transform (FFT) and Frequency Spectrum. (a) FFT conversion of discrete time domain to discrete frequency domain of size N. (b) FFT-shifted discrete signal to display $|X[k]|$ frequency spectrum of bandwidth f_s.

2.5.4 Portable Receiver

For a portable receiver used for insect detection, data-recording functionality is desirable. To do this, the FFT algorithm can be recursively applied to the continuous data stream of the I/Q samples using pre-built DSP functions of a software package. In this thesis, a HackRF One SDR peripheral and GNU Radio software framework are used in tandem to perform the signal recording duties of an SDR receiver. Every power spectrum $|Xk|^2$ constructed from the continuous data stream is decomposed by its argument $arg(|X[k]|^2)$ to determine the peak frequency component $f_m \propto k^{(m)}\Delta a$ of the k^{th} Fourier index of the m^{th} power spectrum. Since this is a continuous data stream, the data is processed in a queue, assuming no data loss, f_m is processed and recorded every $dt = 1/f_s$.

Thus, in Chapter 3, we will explain the construction and demonstrate the functionality of the portable system in a field application. Chapter 4 will describe how insect activity and frequency shift response can depend on time, which can vary between insect species, and number, which will then be used to develop a simple model to distinguish species.

3

Portable Insect Detection System

This chapter presents the material construction and experimental techniques used to develop the portable insect detection system and apply it to a mock field test in grain bulk. We begin by characterizing the microwave sensor, which encompasses the design and fabrication of a CPW-backed IDC resonator. Its resonant frequency and electric-field distribution around the interdigital electrodes are verified through both measurement and simulation. Following this, we discuss the implementation of active circuitry, specifically an amplifier, to form a microwave oscillator via a feedback loop. The relationship between output power, bandwidth, and input voltage is explored to determine the optimal operating voltage to construct a microwave transmitter. For a portable system, the receiver path is first explored by demonstrating the architecture of the SDR HackRF One hardware peripheral. Then, the hardware interface with GNU Radio software is explained by describing the peak frequency recording flowpath. The experimental method for detecting two post-harvest insect pests, Rusty Grain Beetle (RGB) and Red Flour Beetle (RFB), is outlined, including time series data on frequency-shift response and instantaneous insect activity level, compared to the response from a single grain of wheat dropped onto the sensor surface (common debris in grain environment). Finally, we describe a modified sensor placed within a mock grain bin with infested grain, using a probe trap to determine the capture time of an insect entering and exiting the sensor.

3.1 Microwave Sensor Characterization

Constructing a near-field dielectric sensing microwave device that can be used without the addition of lab-based equipment suggests implementation of microwave oscillators. A microwave oscillator generates stable high-frequency signals by combining an amplifier and a frequency-selective network (resonator) in a feedback loop. The amplifier provides the necessary gain to sustain oscillations by compensating for losses, while the frequency-selective network determines the oscillation frequency. This network filters out unwanted frequencies, allowing only the oscillation frequency to be amplified. Together, these components maintain a stable microwave signal. A more descriptive operation of microwave oscillators is given in Chapter 2. In this section, we first focus on the microwave resonator construction.

Presented in Figure 3.1 is the IDC resonator, printed below a gap-coupled, ungrounded CPW. Prior to fabrication, the IDC resonator schematics were designed using ANSYS HFSS CAD software. The resonator was printed on a RO4035B dielectric slab (0.76 mm thickness, $\epsilon_r = 3.66$), with double-sided 35 μm copper cladding, using a S103 ProtoMat PCB plotter. The total planar size is $W_B \times L_B = (53.5 \times 58)$ mm^2 and all relevant copper dimensions are provided in Table 3.1.

The IDC structure of the sensor (Figure 3.1(a)), outlined by the dotted black line, is connected to the SMA output port with length L_A. An outer copper square ring, surrounding the electrodes measures (20×20) mm^2, forming the sensor surface. A branch line separates two columns of interdigital electrodes, each column containing eight electrodes with a length of $l_f = 5.25$ mm, width $w_f = 0.5$ mm, and spacing $w_g = 0.5$ mm (Figure 3.1(c)). Figure 3.1(b) shows the underside, where the gap-coupled CPW transmission line is connected to two SMA ports for power transfer between port 1 and the resonator and the resonator to port 2. The slot width s_{TL} and transmission line width w_{TL} were selected to achieve a 50 Ω impedance matching necessary for interfacing with measurement equipment and active circuitry.

To validate the resonance frequency of the IDC structure, a preliminary measurement and comparison with simulation were conducted. The experimental setup includes the IDC

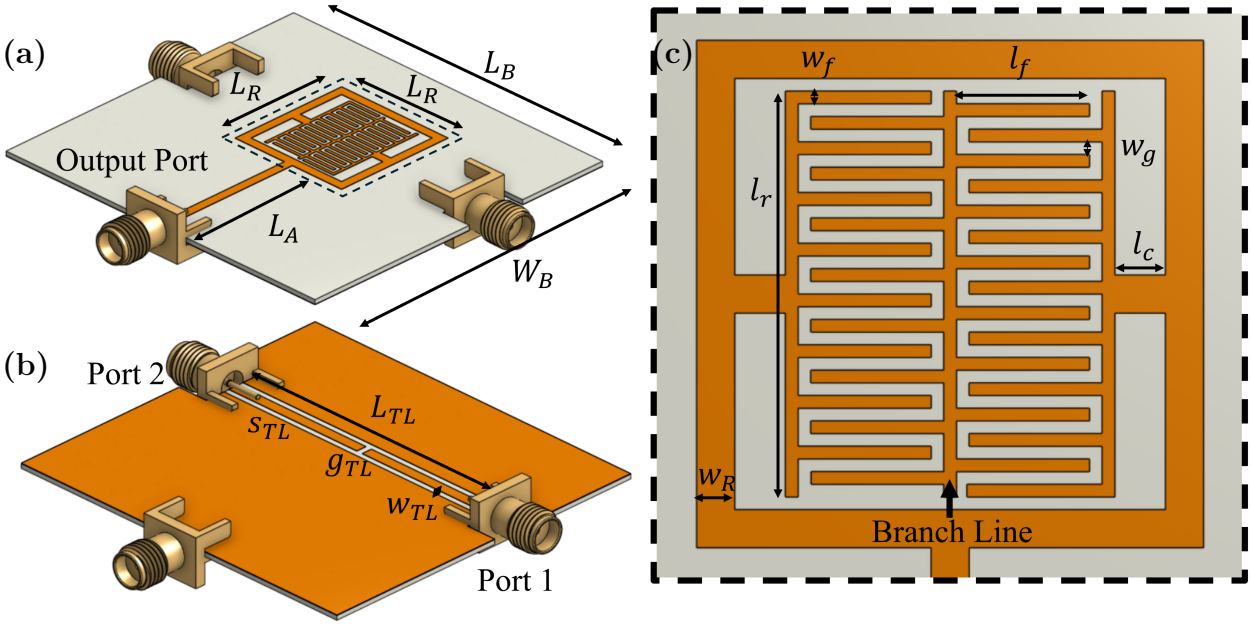


Figure 3.1: Microwave Sensor Schematics. Horizontal dimensions of RO4350B $\epsilon_r = 3.66$ with 35 μm copper trace thickness (board size: $W_B \times L_B$) (a) Top surface of sensor with black dotted outlined ringed ($L_R \times L_R$) IDC structure connected via trace length L_A to output port. (b) Bottom surface of sensor: gap-coupled CPW backside (s_{TL}: slot width, g_{TL}: gap width, and L_{TL}: transmission line length). (c) IDC structure inside of square copper trace of width w_R composed of 4 columns of 8 digital fingers (l_f: finger length, w_f: finger width, and w_g: gap width).

Top Surface		*Bottom Surface*	
Dimension	mm	Dimension	mm
L_R	20	L_{TL}	46.8
L_A	23.9	s_{TL}	0.925
w_R	1.5	g_{TL}	1
l_c	2	w_{TL}	1.68
l_f	5.25	W_B	53.5
w_f	0.5	L_B	58
w_g	0.5	-	-

Table 3.1: Microwave sensor dimensions of the top and bottom surface (sensor size $W_B \times L_B$ measured from either top or bottom surface).

resonator with a 50 Ω matched load at the output port; port 1 and port 2 are connected via a 50 Ω coaxial connector to a Keysight E5080B Vector Network Analyzer (VNA) (Figure 3.2(a)). $|S_{21}|$ measurement results were recorded using MATLAB on a laptop. A brief explanation of the $|S_{21}|$ measurement refers to the magnitude of the transmission coefficient, which represents how much power is transmitted from port 1 to port 2 of the tested resonator. Typically recorded in decibel form, $|S_{21}|[dB] = 10\log_{10}(P_2/P_1)$ is what is observed using experimental and simulation tools, where 0 dB represents complete power transmission.

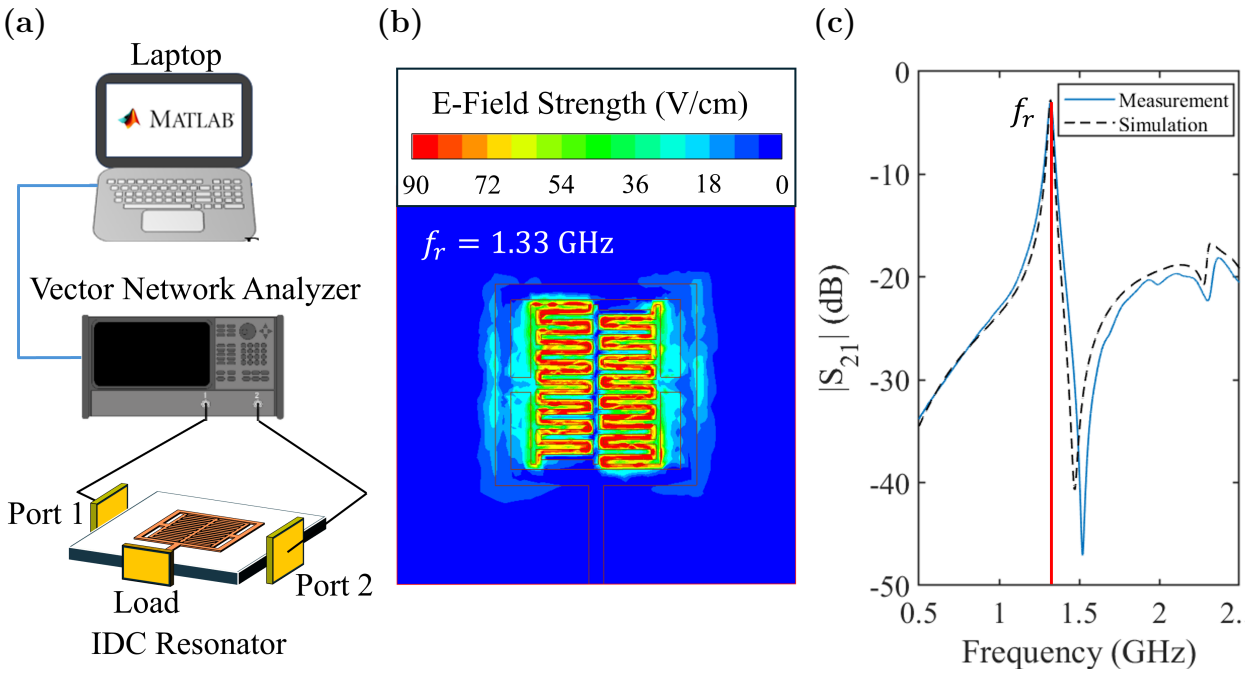


Figure 3.2: Measured and Simulated $|S_{21}|$. (a) Experimental $|S_{21}|$ measurement using VNA and IDC Resonator with impedance matched load at the output port. (b) IDC resonator HFSS simulation of the resonator surface and electric-field magnitude color coded at resonance f_r.(c) Measured (solid-blue line) and simulated (dotted-black line)$|S_{21}|$ parameter of the IDC resonator. Resonance frequency f_r is the simulated resonance frequency (solid-red line) near the measured resonance frequency.

The HFSS EM simulation tool was used to analyze the electric-field distribution of the resonator at resonance observed by the peak of the $|S_{21}|$ parameter. The electric-field distribution, colour coded in Figure 3.2 (b), at a resonance frequency of f_r = 1.33 GHz, shows that the strongest electric field regions are within the interdigital spacing, analogous to

the locations of the capacitive regions from Equation 2.11, and weaker fields near the outer square ring. These capacitive or strong electric-field regions indicate the areas sensitive to dielectric-induced frequency shift responses from insect movement.

The measured resonance frequency $f_{r,m} = 1.3313$ GHz closely matches the simulated frequency $f_{r,s} = 1.33$ GHz (Figure 3.2(c)). The peak transmission magnitudes were also similar, with $|S_{21,m}| = -2.99$ dB and $|S_{21,s}| = -2.78$ dB. However, both measured $Q_m \sim 58$ (with bandwidth $BW_m \sim 22$ MHz) and simulated $Q_s \sim 43$ ($BW_s \sim 30$ MHz) values indicated a low Q-factor and a large bandwidth, which negatively impact the resonator's resolution, making it difficult to detect small perturbations, such as insect movement. The following subsection addresses how this issue is mitigated.

3.1.1 IDC Microwave Oscillator

Transitioning from a microwave resonator to an oscillator involves the addition of an active component. A Qorvo TQP3M9037 Low-Noise Amplifier (LNA) is integrated using a PCB evaluation board. Two 50 Ω coaxial cables (16.5 mm) connect the resonator ports to the LNA input and output. The LNA is powered by a DC voltage source, completing the feedback loop for the microwave oscillator, which serves as the sensor used throughout this thesis (Figure 3.3). The output signal is connected to a Keysight N9010A EXA Signal Analyzer via a 30 mm 50 Ω coaxial cable, and the data are recorded using MATLAB.

The sensor's performance was analyzed by examining the power spectrum at different input voltages, focusing on bandwidth and output power to assess whether the oscillator improves resolution compared to the passive resonator. The experimental setup (Figure 3.3) uses a Keithley 2400 Sourcemeter for variable DC voltage. Spectrum captures were taken 100 times across input voltages from 0 to 12.5 V, with bandwidth and power determined by Gaussian fitting about the oscillation frequency f_o, as shown for the 3.7 VDC (Figure 3.4(a)). The bandwidth remained nearly insensitive to voltage, showing a significant improvement with a bandwidth on the order of Hz compared to the MHz scale bandwidth of the passive

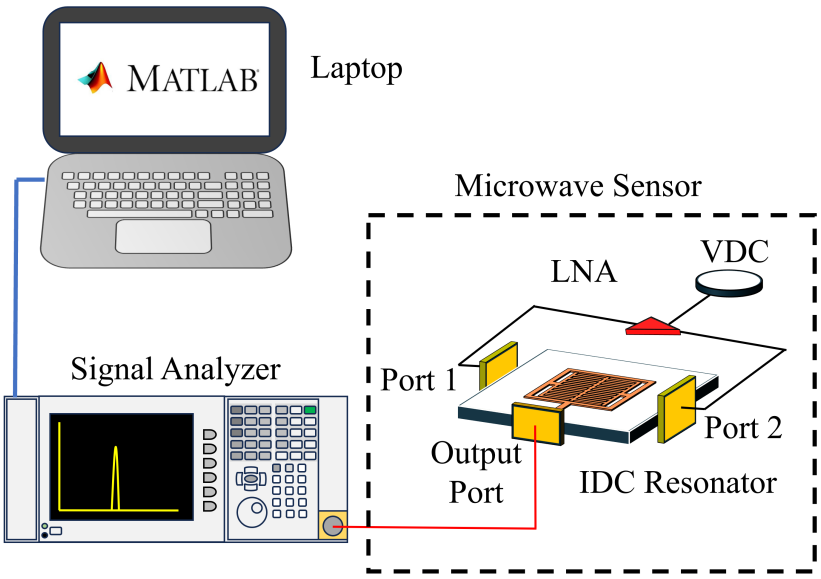


Figure 3.3: Experimental Setup with Microwave Sensor. Microwave sensor composed of VDC, LNA, and IDC resonator connected via output port to a signal analyzer. Spectrum recorded and analyzed with MATLAB software using a Laptop.

resonator (Figure 3.4 (b)), generating a Q-factor enhancement up to 10^6. Peak power increased non-linearly with voltage beginning from the startup voltage of 1.2 V, reaching a maximum of 9.5 dBm at 10.3 V, with a maximum efficiency of 1.3% at 3.15 V (Figure 3.4(c)). At 3.7 V, commonly provided by lithium-ion batteries, the sensor produced $P_{out} = 4.0$ dBm and $P_{eff} = 1.24\%$, this voltage is selected and used in subsequent chapters. The enhanced frequency resolution of the microwave oscillator sensor is crucial for accurate detection, and while output power is also important, it is not the primary focus, as a pre-amplifier at the transmitter output or antenna amplifier at the receiver input can be used to boost the signal.

3.1.2 Portable Setup

Now, we present a portable insect detection system using the HackRF One SDR as a makeshift frequency spectrum analyzer and receiver. The HackRF One is a half-duplex transceiver capable of transmitting and receiving a wide range of radio frequencies (1 MHz to 6 GHz). In the setup (Figure 3.5), the LNA and microwave resonator form the sensor's transmitter

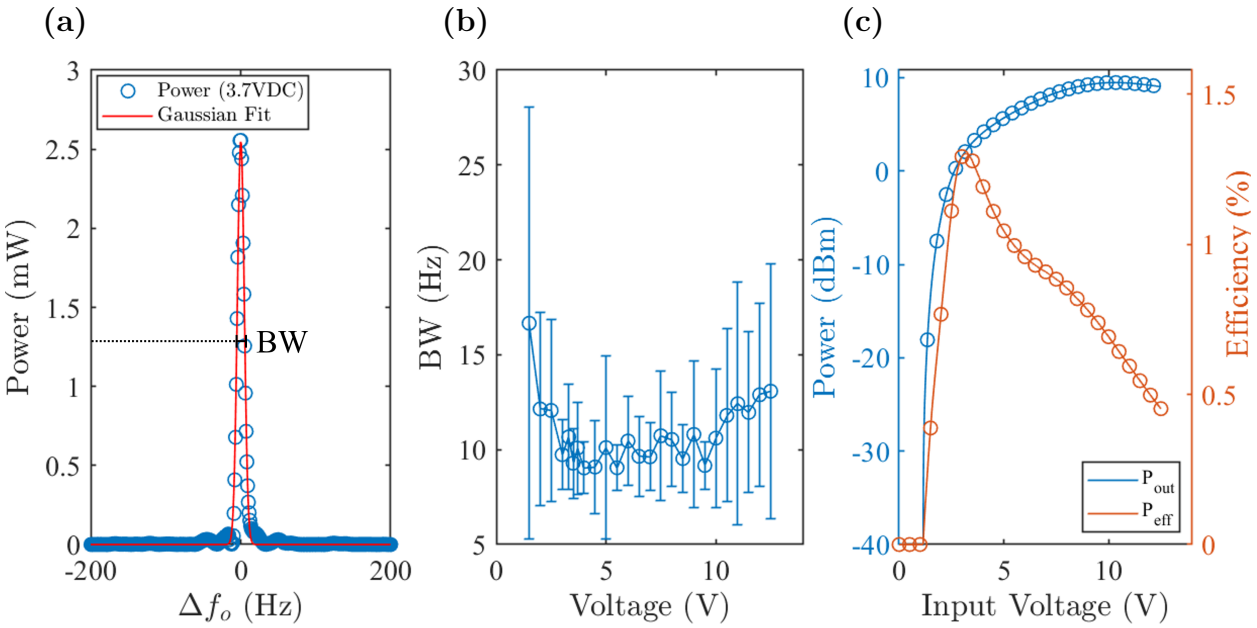


Figure 3.4: Microwave Sensor Performance. (a) Typical power density spectrum at 3.7 VDC input (blue markers) with Gaussian distribution fit (solid-red line) of the offset oscillation frequency Δf_o. (b) Bandwidth measurements with error bars as a function of input voltage. (c) Microwave sensor output power (blue markers) and power efficiency (orange) as a function of input voltage.

path, which is connected to an antenna. This antenna transmits the signal, which is then received by the HackRF One.

In the receiver path, the antenna collects incoming RF signals, which are filtered and passed through the RF tuner for direct downconversion. The RF tuner, using a MAX2837 transceiver, converts high-frequency RF signals to lower base-band frequencies by mixing them with a local oscillator through quadrature demodulation. The resulting base-band signal, containing both in-phase (I) and quadrature (Q) components, is digitized by an 8-bit analog-to-digital (A/D) converter. The digitized I/Q data is then buffered and packaged for USB communication by the Digital Down (DD) Converter, managed by the LPC4320 ARM Cortex-M4 microcontroller. The base-band digital data are transmitted through the USB interface to the host CPU, where specialized SDR software (such as GNU Radio) is used for DSP to analyze and characterize the received signal. GNU Radio is an open-source software framework that simplifies communication and signal processing for SDR hardware. It uses

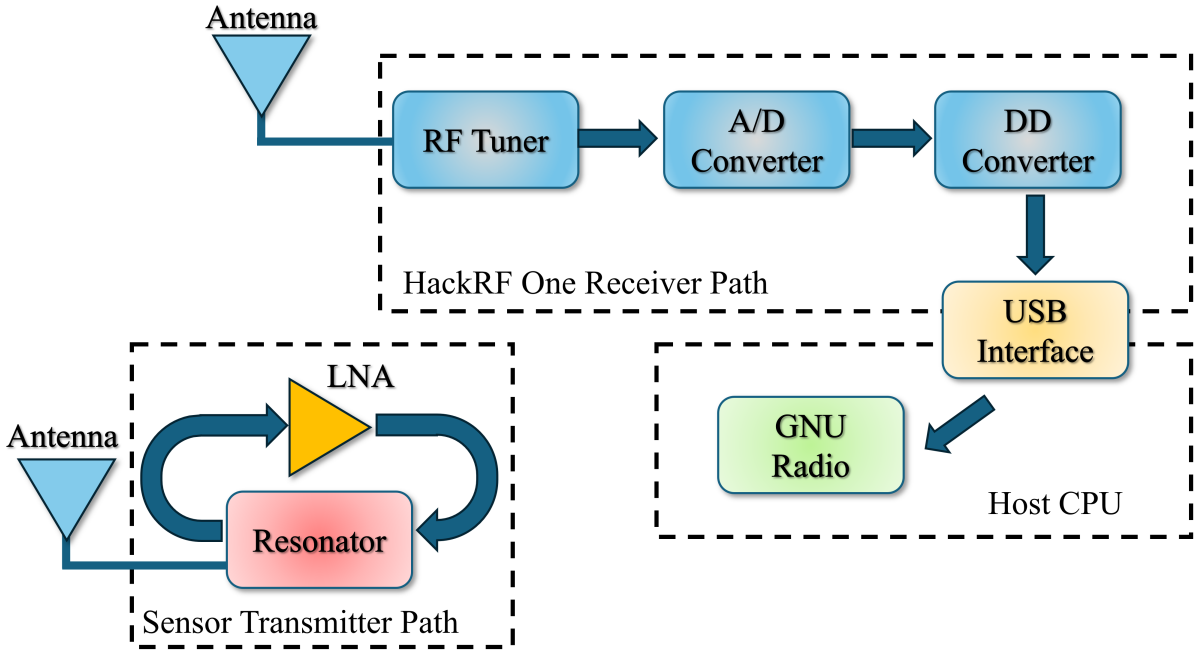


Figure 3.5: Hardware Transmitter and Receiver Flowpath. Flowpath of Transmitter (Microwave Sensor) and Receiver (HackRF One SDR) path communicating wirelessly via Antenna. Data recorded and analyzed in Host CPU.

embedded code blocks of specialized functions, arranged in a flowgraph design. To reduce the complexity of viewing the flowgraph (Figure 3.6), multiple code-block functionalities are combined into a single block, simplifying the data stream from start to finish.

The data stream begins at the Application Programmable Interface (API), which serves two purposes: interfacing with the HackRF hardware and converting the complex digital base-band signal into a stream of samples. The API also allows control over the HackRF's receiver gain, sampling rate, and tuning frequency. The data stream is processed through both the GUI and DSP flowgraph paths. The time-domain I/Q samples can be visualized in the GUI, while the DSP path handles recording.

In the DSP path, the time domain data is transformed into the frequency domain using the Fast Fourier Transform (FFT) algorithm, with the spectrum's bandwidth determined by the sampling rate and centred on the tuning frequency. A peak detection block identifies the frequency channel with maximum power, reducing the rest of the span to a single f_k data point, which is then recorded by the file handler block.

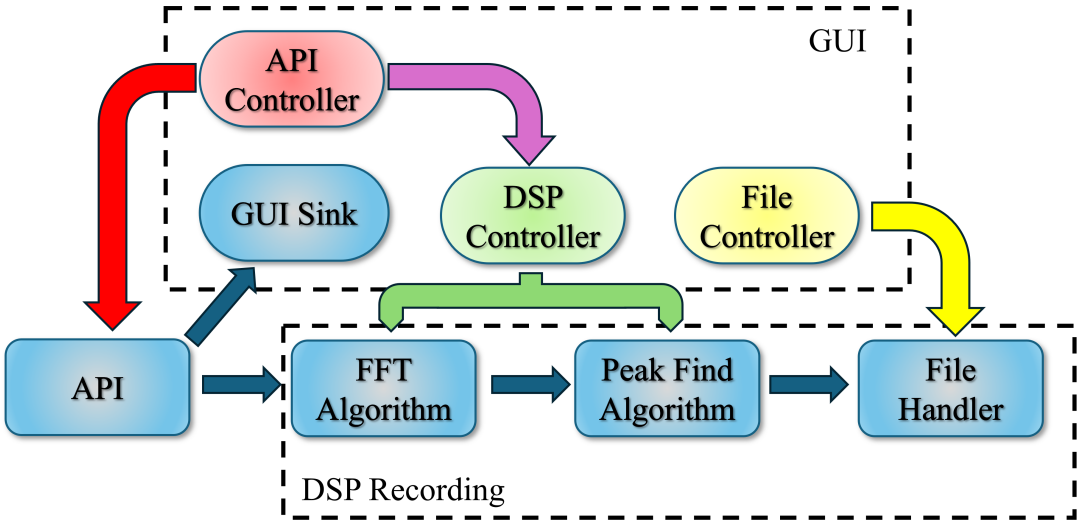


Figure 3.6: GNU Radio Software Data Stream Flowpath. Flowpath of the data stream input from HackRF into GNU Radio framweork. A Hardware-to-Software link interface (API) splits parallel data stream between GUI and DSP recording. The GUI interfaces directly with and can control HackRF, DSP and File Handling blocks individually for real-time software editing.

The GUI path provides real-time data visualization (GUI Sink) that displays an interactive frequency spectrum. The API widget controls the instantaneous bandwidth (frequency spectrum span) via the sampling rate and tuning frequency, affecting the DSP controller widgets responsible for scaling and centering the frequency spectrum. Recording is initiated and terminated by the file controller.

The HackRF supports a maximum sampling rate of 20 Msps. Since RF-to-base-band downconversion is done using a quadrature demodulator, the maximum observable instantaneous bandwidth using the FFT algorithm is 20 MHz. To minimize data loss from insect movement, the sampling rate is set to $T_s = 20$ MHz/s, with the finest frequency resolution achievable using an FFT size of $N_{FFT} = 2^{15}$, as limited by the GNU Radio software. The frequency resolution is $\Delta a = 610$ Hz and the recording speed is $dt = \frac{1}{\Delta a} = 1.64$ ms. This setup, using HackRF and GNU Radio software, was employed for the experiments described in the following section.

In completion, Figure 3.7 describes the general portable insect detection system used throughout the rest of Chapter 3. The transmitter is the microwave sensor (resonator, LNA, and VDC) and antenna. Here, the LNA is powered by a 3.7 V lithium-ion battery with a lifetime operation of $\sim$ 24hrs. The HackRF One SDR peripheral can be a wired or wireless receiver depending on whether an antenna is used (Figure 3.7). Thus, the transmitted signal from the microwave sensor is continuously digitized and sent to a laptop where, using the GNU Radio software framework, it displays and records the signal which is the core basis on how experiments are performed herein.

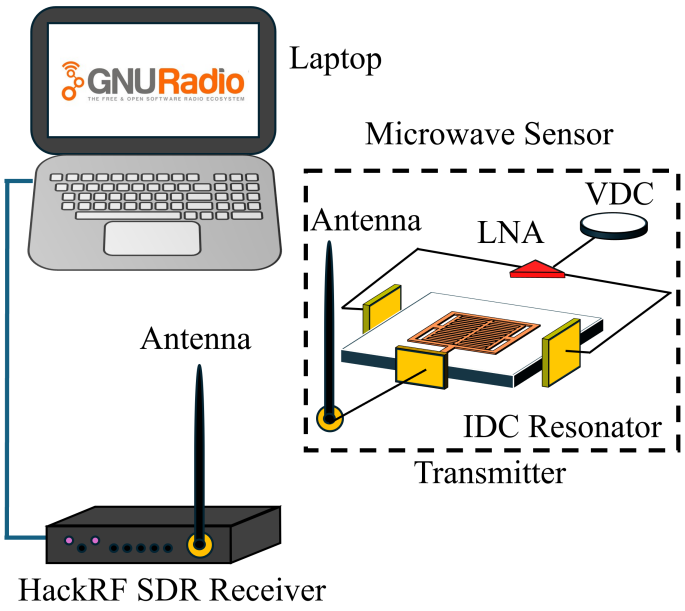


Figure 3.7: Portable Insect Detection System. The general insect detection system composed of a microwave sensor transmitter, HackRF One SDR receiver, and interfaced with GNU Radio. This wireless setup utilizes antennas at receiver input and transmitter output ports.

3.2 Preliminary Results using Insect Detection System

This section briefly demonstrates the frequency response and instantaneous insect activity level typically observed when an insect is placed on the sensor. The rearing information on

the insects used in the experiment and all experiments used throughout the thesis will be provided. Additionally, a single grain of wheat is to be dropped on the sensor to indicate the difference in signal between insect and grain, important to distinguish false positives.

3.2.1 Insect Rearing Information

Adults of *Tribolium castaneum* (Red Flour Beetles, RFB), of mixed sexes and of various ages, were reared on a 19:1 feed mixture of wheat flour and brewer's yeast at a temperature of 30°C and 70 ± 5% relative humidity. Adults were extracted from the laboratory colony by sieving and aspirating with a laboratory vacuum pump. Approximately 50 adults were placed in glass vials containing 5 g of the wheat and yeast mixture. They were then acclimated for at least 24 hours at 21°C before being introduced into the microwave sensor.

For each sample measurement, the required number of insects was separated using a brush and transferred to a clean glass vial, which was loosely sealed with a perforated lid. This vial was then used to drop the insects by gravity into the microwave sensor. After each measurement, the insects were not reintroduced to the sensor. A new sample from the laboratory colony was obtained every five days and the insect preparation process was repeated.

Adults of *Cryptolestes ferrugineus* (Rusty Grain Beetles, RGB), of mixed sexes and of various ages, were reared at 30°C and 75 ± 5% relative humidity. Their colony feed mixture consisted of 90% whole wheat, 5% cracked wheat, and 5% wheat germ. The extraction method, number of insects, and sample preparation for RGB were identical to those described for the RFB.

It is important to note that RFBs are typically 4 mm in length with an oval shape, while RGBs are less than 2 mm in length and have a rectangular shape [62, 63]. This distinction in size and shape affects how the dielectric content is distributed within their bodies, which in turn influences the overall dielectric constant depending on the shape and density of the insects [64]. Generally, the magnitude of $|\Delta \bar{f}|$ Equation 2.30 will be a mixture of both size

and ϵ_r which will be a primary contributor to identifying species and number investigated in Chapter 4.

3.2.2 Insect Detection System Experimental Methods

The experimental setup used for the insect detection system is based on Figure 3.7 modified by a containment area around the sensing surface. Figure 3.8(a) shows a glass 30(28) mm outer(inner) diameter cylindrical vial with an open end glued and centred on the IDC resonator and the other open end that can be sealed with a lid. Typical analytes within the grain environment are examined: adult RFB (4 mm length) and RGB (2 mm length) insects and typical grain kernel debris. They are dropped into the surface of the contained sensor (sealed for insects to prevent escape), where the f_m data points are recorded over 15 minutes by the system and later analyzed by MATLAB.

The analyte signals were independent time-series measurements taken at room temperature. Each time-series data set begins at t_0 which is the point in time prior to the first detected signal at t_1 recorded for a total duration of 15 minutes. In Figure 3.8(b), each $f_m(t_m)$ is recorded at time $t_m = mdt$ beginning at $f_0(t_0)$ for $m = 0$. Two primary measurements are performed, the first is frequency shift

$$\Delta f_m(t_m) = f_m(t_m) - f_0 \tag{3.1}$$

which in conjunction with Equation 2.30 relates the dielectric size and position of the analyte with the time-varying frequency shift distance from f_0 due to the change in position at time t_m on the sensor (Figure 3.8(b). The second measurement is the forward discrete frequency time-derivative:

$$\frac{df_{m+1}(t_{m+1})}{dt} = \frac{f_{m+1}(t_{m+1}) - f_m(t_m)}{dt} \tag{3.2}$$

which, like Equation 3.1, depends on the dielectric size and time-dependent position, but also the size of frequency deviations df between consecutive time steps dt as a consequence of movement detected by the sensor (Figure 3.8(b)). For detected movement, df_m/dt is

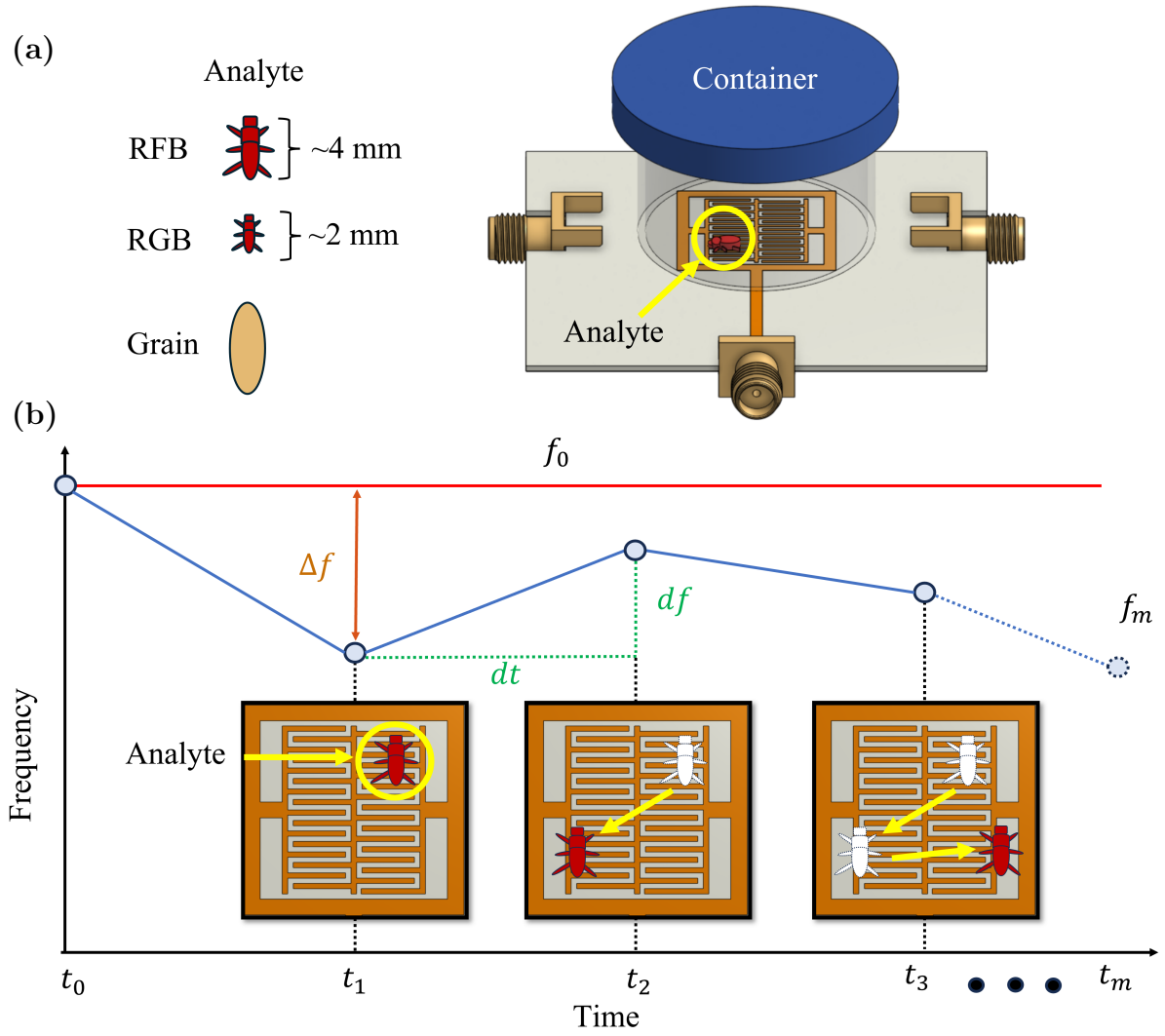


Figure 3.8: Microwave Sensor for Analyte Movement Experiment.(a) Modified microwave sensor composed of open ended glass cylindrical vial and lid centered about the sensor. Analytes used are RFB ($\sim$ 4 mm in length), RGB ($\sim$ 2 mm in length), and grain kernel. (b) Typical time-series data of an analyte detected at t_1 on the IDC surface inducing a Δf_m and df_{m+1} per time step dt for every $f_m(t_m)$ based on the position of the analyte.

distributed around an average $d\bar{f}/dt$ for a data set of size m and $d\bar{f}/dt = 0$ for a stationary target or undetected movement. We use the magnitude of frequency deviations scaled by dt to quantify the level of insect movement which we refer to as the *Instantaneous Insect Activity Level* $|df_{m+1}/dt|$.

3.2.3 RFB, RGB, and Grain Movement Detection

It is apparent in Figure 3.9 that the frequency shift response and the instantaneous insect activity level response are different for the two different sized insects and for a single grain. Within $t = 15$ minutes, the smaller RGB had a maximum $\Delta f_{RGB} = -1.2$ MHz, whereas the larger RFB had a maximum $\Delta f_{RFB} = -4.1$ MHz, both much larger when compared to a baseline maximum frequency response $\Delta f_{Bare} = -4.5$ kHz (Figure 3.9(a)). The instantaneous insect activity level, Figure 3.9(b), observed a maximum $|df/dt|_{RGB} = 201$ MHz/s and $|df/dt|_{RFB} = 54$ MHz/s for the RGB and RFB, respectively. A signal-to-noise ratio is used to compare the noise of the baseline signal to the instantaneous insect activity level, demonstrating typical RGB and RFB SNR values ranging from $SNR_{RGB} \in [0\ 115]$ and $SNR_{RFB} \in [0\ 429]$, respectively. Here, the maximum SNR value within the measured range for the RFB is around 4 times larger than the SNR of the RGB. However, there are multiple, varying in size, insect signal events in contrast to the single signal event observed when a grain is dropped onto the sensor. By dropping a single grain within the sensing environment, a typical maximal frequency shift of $\Delta f_G = -4.75$ MHz, Figure 3.9(c) is observed. Upon initial impact, we see a large change in $|df/dt|$ attaining a maximum value of $|df/dt|_G = 739$ MHz/s in Figure 3.9. In the inset, we can see that this one-time event lasted for a period $\propto$ 3 ms.

In summary, the portable insect detection system can be used to detect the movement of insects by measuring both responses from the frequency shift and the instantaneous insect activity. Insects of different sizes observed within the sensing environment can give different signal magnitudes based on their dielectric content, position, and movement, occurring as multiple events in time. Whereas, a single grain falling on top of the sensor produces a single strong in magnitude and short-lived event. Now that we have seen the basic measurement principles of the insect detection system, we prepare a field-like test using a mock grain bin in the following section.

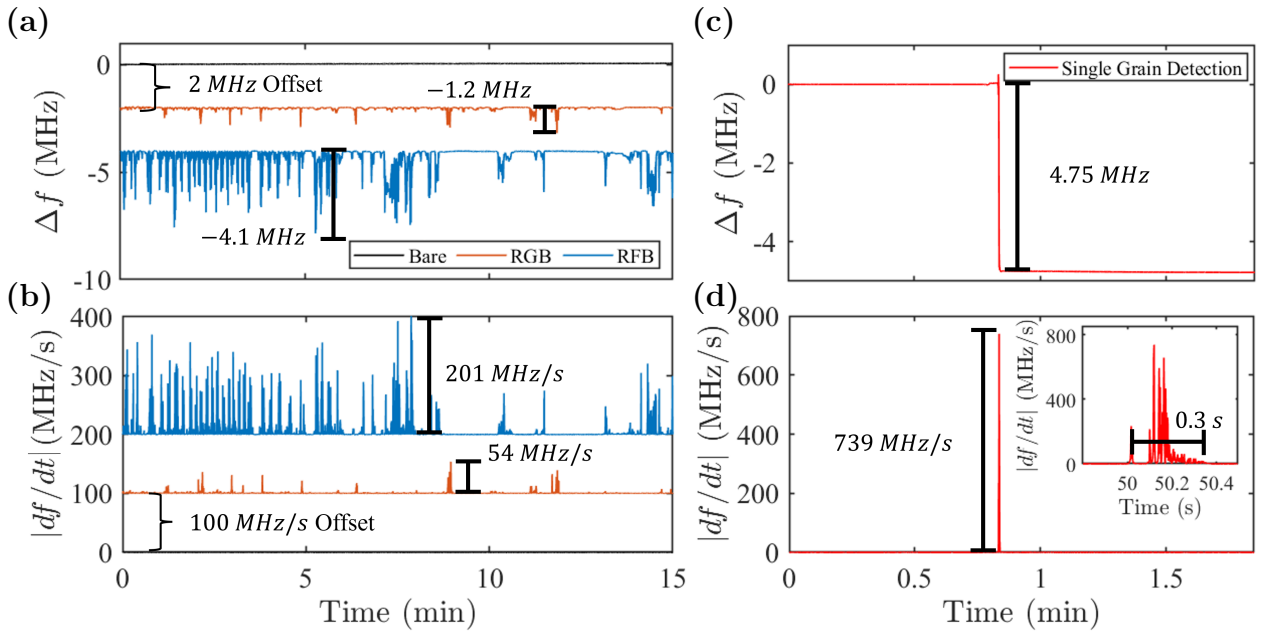


Figure 3.9: Analyte Detection Results. Multiple insect signal response events: (a) Frequency shift response Δf with 2 MHz Offset between trials and (b) Instantaneous insect activity level $|df/dt|$ with 100 MHz/s Offset. Bare sensor response with no insect is represented by black solid-line in (a) and (b), Single grain drop signal response event: (c) Δf. (d) $|df/dt|$ with inset of total transient time of grain drop event. Maximum values are provided by a black scale in each plot.

3.3 Grain Container and Microwave Probe Sensor

The portable insect detection system based on our microwave sensor can potentially provide grain handlers with an efficient tool for monitoring insect activity in stored grain. To demonstrate the system's capabilities, a mock-field test is performed in 10 kg of insect-infested grain at different levels of insect density. Using a modified sensor with an integrated probe trap, we demonstrate at what point in time the insect fell into and escaped from the trap. This could be used as an early warning detection technique to support grain handler decision-making and reduce the need for chemical treatments, helping to maintain grain quality and value.

3.3.1 Microwave Probe Sensor Setup

The portable insect detection system described in Figure 3.7 is modified slightly for the mock-field test. Firstly, the experimental setup consisting of the laptop with interactive GUI, HackRF receiver, and the modified sensor is embedded in 10 kg of wheat grain provided in Figure 3.10(a) As was discussed in Chapter 1, part of the challenge when using the dielectric perturbation technique is selectivity. For a field test, we can separate insects from grain by integrating the tried and true perforated probe trap (STORGARD® WB Probe II) with our sensor. In Figure 3.10(b), a vertical dissection cartoon of the probe trap placed directly above the sensor is presented as a packaged system. The microwave sensor is powered by a 3.7V lithium-ion battery and held within a cylindrical sensor housing. The perforated probe trap diameter is matched and clamped to the sensor housing vertically above the microwave sensor. Additionally, a thin shield was placed on the surface of the sensor with a 5 mm boundary around the sensing region to allow the captured insects to escape into the empty overflow space of the housing. An antenna port is connected via 50 Ω coaxial cable to an antenna which peaks the surface of grain (Figure 3.10(a)). Introducing the probe trap provides the additional benefit of artificially extending the near-field detection range of the sensor by increasing the probability that an insect will interact with the sensor in the grain environment.

3.3.2 RFB Capture Time Analysis

RFB insects were used only for the capture time analysis experiment, 10 insects were placed in 10 kg of clean 12.5% moisture grain and monitored with the insect detection system with the microwave probe sensor for 19.5 hrs at room temperature. This procedure was repeated by replacing the infested grain sample with cleaned grain and placing 5 insects in the 10 kg grain.

The analysis techniques included recording the instantaneous insect activity level, which was compared against a baseline measurement of a non-infested 10 kg of grain. Next, a

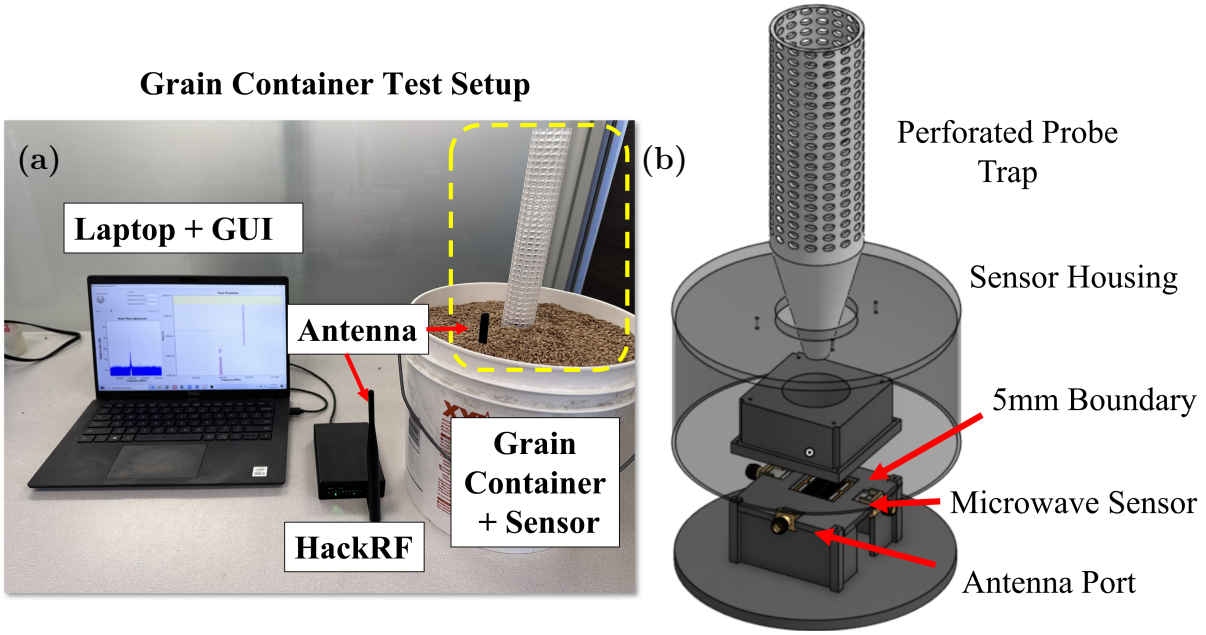


Figure 3.10: Grain Container and Microwave Probe Sensor Setup. (a) Experimental grain container test setup using the portable insect detection system with modified microwave sensor placed in container of 10 kg of wheat grain (dotted-yellow line). Communicating wirelessly via antenna. (b) Modified microwave probe trap sensor with 5 mm trapping boundary. Antenna output from sensor connects to antenna peaking outside of grain.

detection threshold D by setting twice the maximum $|df/dt|$ baseline measurement as a ratio is used to determine insect presence

$$D = \frac{|df/dt|}{2 \times max(|df/dt|_{Bare})} \tag{3.3}$$

By using a binary outcome as a detection level D_L, $D_L = 0$ when $D < 1$ (undetected) and $D_L = 1$ when $D \geq 1$ (detected). To determine the detection time T and capture time CT, two time constraints are imposed. The first constraint is used to differentiate the signal from grain and insect. A single detection event must be longer than 1 s ($> 3\times$ grain drop event Figure 3.9(d)). The secondary constraint requires that the time difference between two detections be less than or equal to $\Delta t \leq 15$ minutes for a single detection event to continue. Beyond 15 minutes, for a single detection, a new event begins and the two timing constraints are used to determine if the signal is an insect and the capture time CT from detection time

T. This second constraint is arbitrary and can be imposed to be stricter or looser, where here we just match our initial 15 minute insect measurements in Figure 3.9. This procedure was performed both at 0.5 insect/kg and 1 insect/kg to determine if insect density had an effect on capture time.

3.3.3 In-Grain RFB Detection using Microwave Probe Sensor

The portable insect detection system, utilizing the microwave probe sensor, has proven successful in detecting movement within stored grain seen in Figure 3.11. During 19.5 hrs, the frequency response of the bare sensor varied between $\Delta f_{Bare} \in [-84, 34]$ kHz; however, for the frequency response measurement in 0.5 insect/kg and 1 insect/kg, the frequency varied between $\Delta f_{0.5} \in [-1.4, 0.08]$ MHz and $\Delta f_1 \in [-3.3, 0.08]$ MHz in Figure 3.11(a), respectively. The maximum baseline $|df/dt|$ noise of the sensor was observed as $|df/dt|_{Bare} = 11.6$ MHz/s, which is much smaller than the maximum instantaneous insect activity level for the 0.5 insect/kg measurement of $|df/dt|_{0.5} = 385$ MHz/s and 1 insect/kg measurement of $|df/dt|_1 = 916$ MHz/s. In our measurement, it appears that in Figure 3.11(a) and (b) the signal response is much larger using the 1 insect/kg, which suggests a possibility that more than 1 insect was captured. Also, notice that the upper limit is positive in all three frequency shift responses, suggesting instability in the oscillation frequency. Although the frequency drift is minute, it indicates that external factors such as temperature and relative humidity may be affecting the oscillation frequency. However, since $|df/dt|$ observes the short-term time step dt the long-term drift is unobserved which is the metric we will use to analyze insect captures and their duration.

Now, we impose the timing constraint and the movement threshold calibrated to the baseline sensor to determine a detection level between 0 (undetected) and 1 (detected). There are 3 observed detections that were observed in both trials using different insect densities in Figure 3.12. At 0.5 insect/kg in Figure 3.12(a) the 3 detections were observed at time $T_{0.5}^{[1,2,3]} = [107.17,\ 158.93,\ 190.95]$ minutes with a capture time until es-

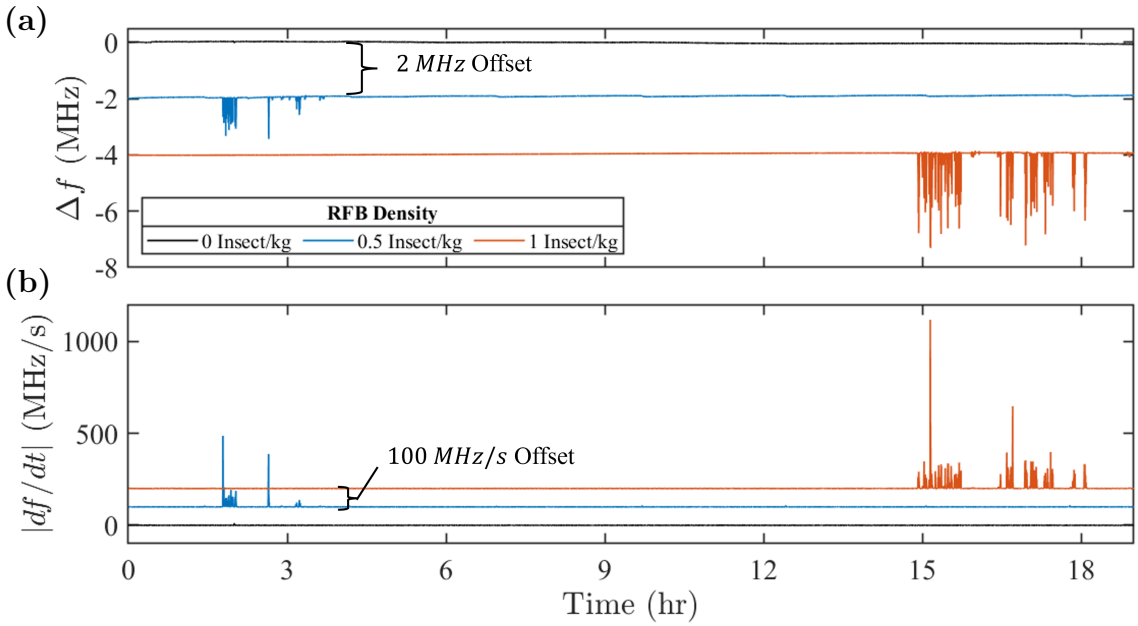


Figure 3.11: Microwave Probe Sensor $|df/dt|$ and Δf Results. 19.5 hrs time-series results for different RFB insect densities (blue line: 0.5 Insect/kg and orange line: 1 Insect/kg) and bare sensor/clean grain (black line). (a) Δf *vs. Time*. (b) $|df/dt|$ *vs. Time*.

cape $CT_{0.5}^{[1,2,3]} = [15.14,\ 0.50,\ 3.03]$ minutes. Similarly, at 1 insect/kg in Figure 3.12(b) the detected time $T_1^{[1,2,3]} = [895.28,\ 988.72,\ 1070.70]$ minutes with a capture time of $CT_1^{[1,2,3]} = [48.73,\ 59.59,\ 15.13]$ minutes.

Oddly, the first detection time occurs earlier using 0.5 insect/kg versus 1 insect/kg by over 13 hrs. This is contrary to the idea that more insects in the grain bulk will more likely be detected by the sensor, indicating either a lack of movement or different distribution within the grain bulk. The capture times, however, are about 3 to 4 times longer for the first two capture times at 1 insect/kg experiment versus the longest capture time at 0.5 insect/kg. This suggests that the 5 mm boundary is preventing escape longer at a higher insect density, or more likely that there is more than 1 insect captured at or near the span of time that a detection is considered a single event. Furthermore, this system does not distinguish between individual insects detected, meaning that captured insects that escape into the housing area can be reintroduced onto the sensor and mistakenly counted as a new detection. More than 1 insect captured for the 1 insect/kg density could be a reason for

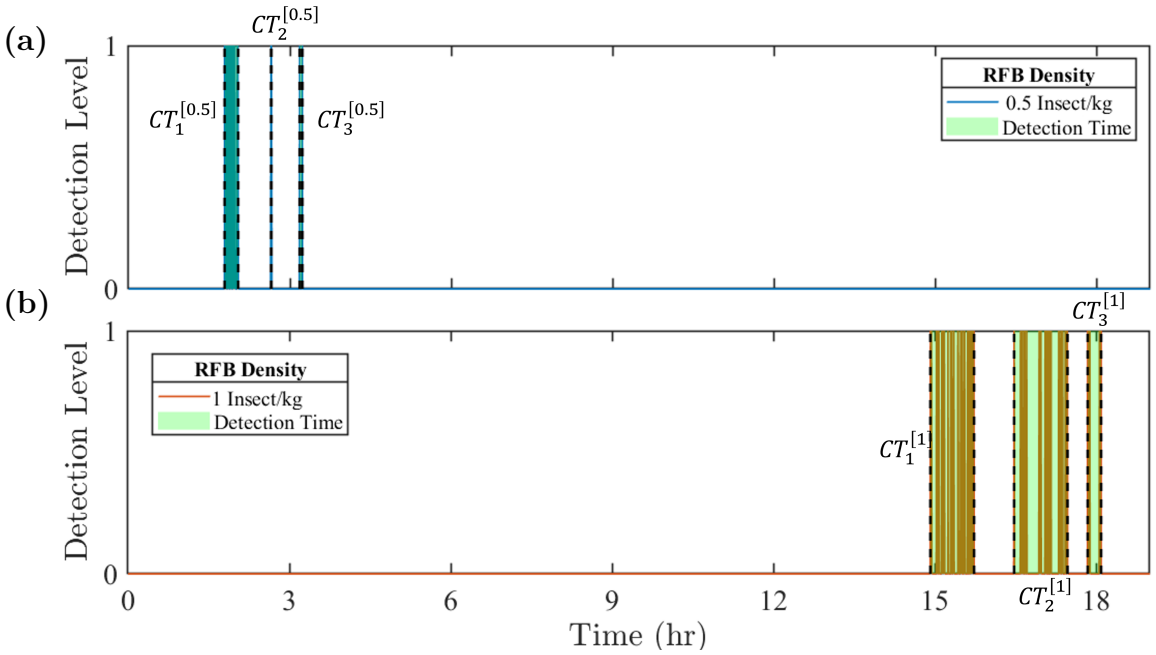


Figure 3.12: Threshold Detection Level Duration Example. Detection Level between 0 (undetected) and 1 (detected). Capture time constrained for duration $D > 1$ seconds and 15 minutes from last detection to be considered a single capture event. Detection time in shaded green region with Capture Time CT time bound between dotted-black lines. (a) 3 detection's at 0.5 insect/kg. (b) 3 detection's at 1 insect/kg.

the heightened insect frequency shift and instantaneous insect activity level in Figure 3.11 (a) and (b) and longer capture times in Figure 3.12 (b). Without visual confirmation and proper venting of captured insects, the system will be prone to miscounting. In addition, due to the small 10 kg mock-grain bin test environment, the distribution of insects within the grain bulk will be a factor that contributes when a detection occurs, which will be even more challenging for field tests with grain bins that hold more than 10s of thousands of kg of wheat. For grain bins on farms or in elevators, just how effective the system detects capture events will ultimately be limited by large amounts of insect and debris that accumulate on the sensor, which is an additional unknown limitation. A more thorough analysis of detection time, capture time, number of insects captured, and boundary size vs. escape time needs to be performed in conjunction with the complex distribution of insects within different sizes of grain bulk and in real grain environments. This analysis can then be extended for other

insect species, like the RGB, and for different insect densities. As of this work, a case for a proper counting procedure and method to differentiate between species will be provided in Chapter 4.

In conclusion, using the insect detection system with a microwave probe trap in 10 kg of grain, when infested, the probe trap successfully identified that there was movement on the surface. Indeed, the frequency shift and instantaneous insect activity level response were elevated from baseline regardless of the insect density used. External factors such as temperature or relative humidity had a minor frequency drift affecting Δf, but left $|df/dt|$ unaffected. Employing a timing constraint and detection level threshold, we observed 3 detection events in both densities with various capture times as short as 0.50 seconds to as long as 59.59 minutes. However, at first glance, the system is prone to miscounting multiple captured and reintroduced insects. The system requires thorough testing in lab and large scale grain environments for future-use considerations.

3.4 Conclusion

In this chapter, we have demonstrated the construction and functionality of this novel IDC microwave sensor. A simple receiver system consisting of a HackRF One SDR peripheral controlled via GNU Radio software can be used wirelessly to detect transmitted RF signals from the IDC microwave sensor. When used to detect the motion and presence of two insects of different sizes, the frequency shift response and instantaneous insect activity level were much stronger for the larger insect. In fact, multiple events of movement were detected for the insect in comparison to the single pronounced signal when grain was to fall onto the sensor. This distinction is important for debris build-up that plagues common stored grain insect detection systems. As a result, a modified microwave sensor integrated with a probe trap was used to assist in capturing and detecting the presence of insects within 10 kg of grain. Using a threshold analysis example, a total of three detections per field test experimental

trial showed capture times varying from 0.5 minutes to 59.59 minutes. This portable insect detection system demonstrates the potential of such a system to be used to assist insect pest management decisions for the grain handler by providing real-time information on the detected presence of insects.

The system currently performs as a motion detector, of which many exist on the market. Identifying the insect species helps determine a proper treatment, such as fumigation, and knowing the number of insects helps to determine the level of infestation severity. Movement of the insect and non-uniform electric field distribution accompanied by microwave sensors, in general, make these two a challenge. But this would provide real benefit to users and would stand out from other systems incapable of these feats. Chapter 4 will demonstrate that species identification and counting can be performed by characterizing the complexity of insect activity and confining their movement to localized sensitive regions on the sensor using boundaries. Then we will construct a method using both time-dependent frequency shift and insect activity metrics to compare two different species and their number for a plausible case for insect detection.

4

Insect Activity and Counting

Apart from remote detection presented in Chapter 3, vital to any grain handler or pest control operator, the identification of insect species and the number of captured species are arguably of equal importance. Knowledge of the species provides insight on treatment methods, and the number of captured insects provides information on the severity of the infestation.

In this chapter, the aim is to demonstrate a method to extract characteristic information from insect time-series data recorded with the portable detection system. First, we explain two different types of insect movement (Active and Spontaneous) using a positional detector analogy. Then we define two sensing boundaries using a positionally strong electric-field localization over a small bounded area and a mixture of weak-to-strong electric-field localization over a large bounded area. We then return to the movement types and demonstrate how to quantify that movement by relating it to an insect activity-duration relationship. Then we experimentally investigate the insect signals for the RFB and RGB insects and how the choice boundaries affect sensitivity separately. Then the insect activity-duration relationship is explored and characterized for 1-to-5 insects using both boundaries. We then demonstrate the sensors' sensitivity towards insect activity and frequency shift response metrics and their evolution over long time intervals. We use the fitted coefficients to make a comparison between both species and construct a simple model to determine the benefits and trade-offs using different-sized boundaries at the end of the Chapter.

4.1 Background on Insect Movement Dynamics and Sensor Interactions

Background on insect movement dynamics and the insect-sensor interaction is first provided. We begin by explaining how the position detected by the sensor varies depending on the type of insect movement, highlighting differences between stimulated movement (Active) and unstimulated movement (Spontaneous). Next, the sensor surface will be mapped with a dielectric probe to demonstrate how the sensor's frequency response correlates with the positional dependency of the electric-field, emphasizing how containment of strong and weak electric-field regions will influence signal strength based on the localization of the bounded sensing area. Lastly, we introduce the the insect activity-duration relationship, and analyze how stimulated and unstimulated movement conditions can affect the observed signal on the microwave sensor.

4.1.1 Position Detecting Insect Movement Dynamics

Presented first is a positional-based frequency response over a specific interval of time analogy to describe the motion of an insect confined to a sensing environment. For an enclosed sensing environment outlined by the boundary in Figure 4.1(a), the position of an insect is defined by $p(\vec{x}, t)$ for a given time t_m, with the total movement spanning the time interval t_1 to t_5 with evenly spaced time steps as an example. The positional sensor situated at $p_s(\vec{x}_s)$ detects the position of the insect at a specific t_m as it passes over the sensor within the time interval.

Scenario 1: In the absence of external stimuli, we say that the insect movement is unstimulated as shown in Figure 4.1(b), the insect moves with smaller changes in position and direction $\Delta p_i(\Delta\vec{x}, \Delta t)$. The movement is spontaneous or discontinuous, such as if it searches for food or mates at t_1, rests at t_2, and eventually passes near $p_s(\vec{x}_s)$ from t_2, to t_3, where it rests again at t_3 to t_4 before reaching its final resting position at t_5. Depending on the positional sensors' sensitivity, the insect may weakly interact at $p_s(\vec{x}_s)$ or go completely

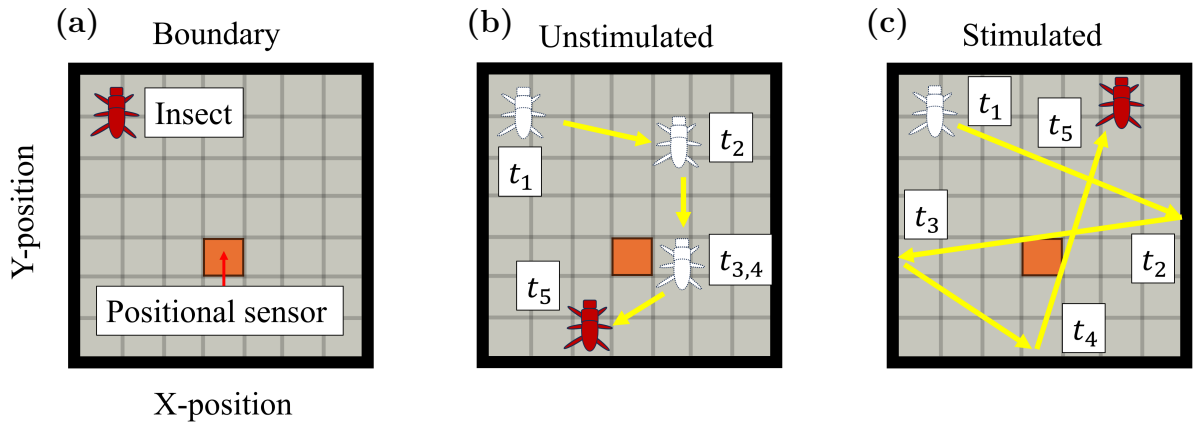


Figure 4.1: Sensing Environment. (a) An insect and a positional sensor in copper-orange has their positions defined by X and Y gray grid-line coordinates within a black boundary sensing environment. (b) Unstimulated movement of an insect with yellow arrows indicating a change in position of a change in time t_m. (c) Stimulated movement.

undetected.

Scenario 2: Consider a controlled external stimulus applied to the insect, we now say that its stimulated movement is active as shown in Figure 4.1(c), which the insect would naturally experience during habitat disturbance or predation [65]. This stimulus induces more active insect movement compared to Scenario 1 with larger changes to both position and direction $\Delta p_i(\Delta\vec{x}, \Delta t)$ with less time resting. Here we see that the insect clearly passes $p_s(\vec{x}_s)$ during time t_2 to t_3 and t_4 to t_5. Thus, there are more interactions at the position of the sensor $p_s(\vec{x})$ due to the increased insect position variability. The average position detected by the positional sensor between Scenarios 1 and 2 is more variable for the active case than for the spontaneous case, as indicated by the sample standard deviation $\sigma_p^{Act} > \sigma_p^{Sp}$.

4.1.2 Frequency and Position Relationship of a Dielectric Probe

The positional sensor argument is used as an analogy to the frequency shift response of a dielectric-perturbed microwave cavity sensor in this thesis. The structure proposed in Chapter 3 is based on the IDC design, with electric-field strength concentrated between the immediate adjacent regions of the electrodes. The frequency-selective nature of the IDC determines the transmitting carrier frequency signal (oscillation frequency f_0) of the microwave sensor. Thus, the implementation of dielectric material into the permeating electric-field lines induces a frequency shift proportional to the size, ϵ_r, and position of the object. Therefore, $p_s(\vec{x}) \equiv f(\vec{x})$, and the sensitivity of the sensor in relation to the object's position for a given point in time is defined by the frequency shift $\Delta f(\vec{x}, t)$ from Equation 2.29. For an insect that is very active, there will be large, rapid frequency fluctuations induced by stronger interactions with the microwave sensor, in contrast to a slow and spontaneously moving insect, with more erratic strong interactions, sensor interactions seen as smaller and gradual frequency fluctuations.

To demonstrate the positional dependence of the frequency response that varies with size and ϵ_r, a mapping of $\Delta f(\vec{x})$ was performed using a dielectric probe along the surface of the microwave sensor, as shown in Figure 4.2. The sensor, consisting of a Low-Noise Amplifier (LNA) and an IDC resonator, was horizontally scanned with a dielectric probe controlled electronically by an XYZ stage equipped with three PK245-01AA Vexta stepping motors (Figure 4.2(a)). Each sequential step was observed as a frequency shift response on a spectrum displayed by a Keysight N9010A Signal Analyzer, where the peak frequency of the IDC emission profile was recorded using MATLAB software.

The dielectric probe was positioned along the x- and y-axes in increments of 160 μm at a fixed height, ensuring that the bottom surface of the probe remained in contact with the IDC copper surface. Each probe had a fixed length of 30 mm and scanned a total area of (24×24) mm^2 (Figure 4.2(b)). Figures 4.2(c-e) show the resulting $\Delta f(\vec{x})$ mappings using three dielectric probes: two with identical contact surface areas C but different ϵ_r values and two with different C but identical ϵ_r values.

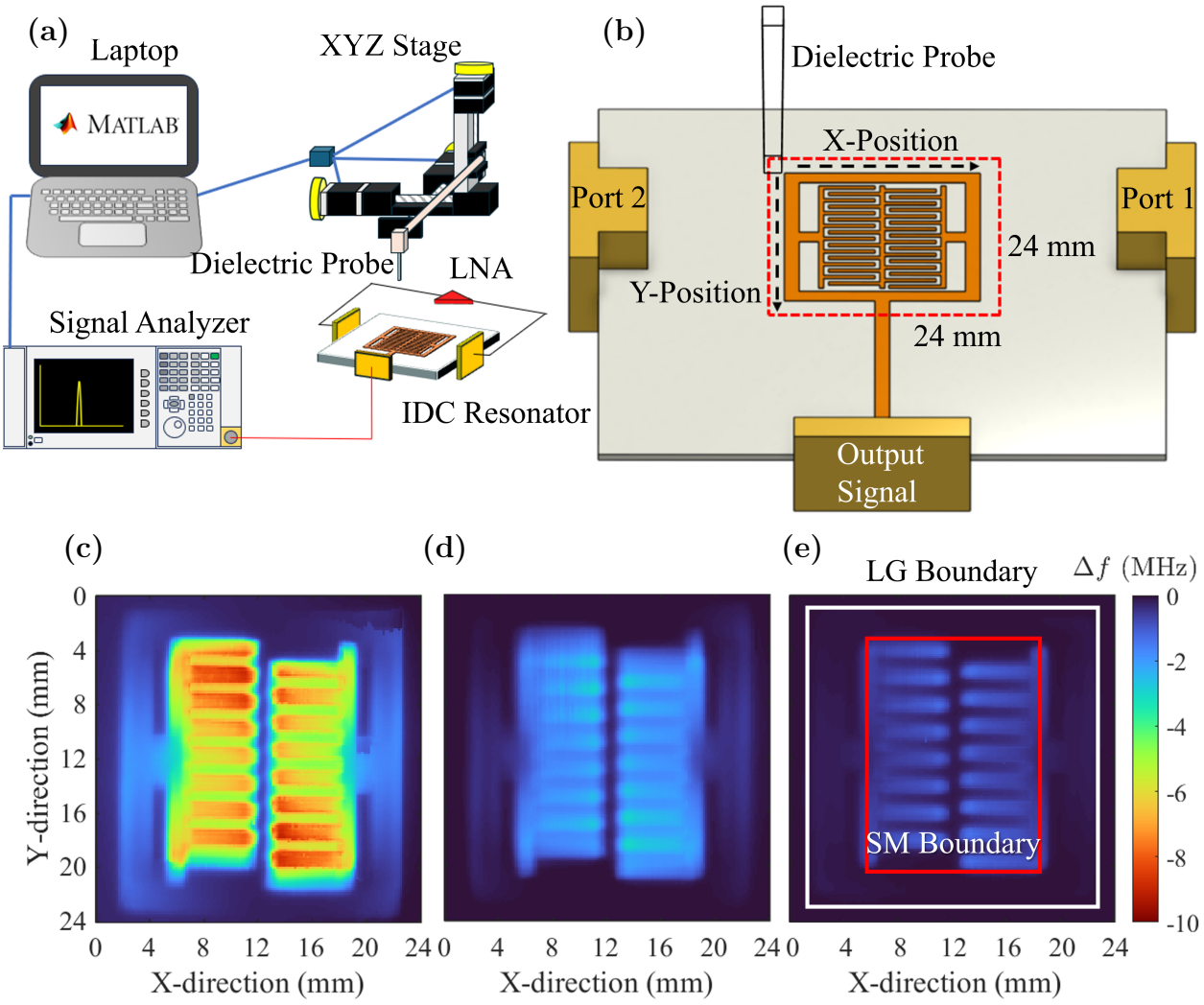


Figure 4.2: Dielectric Probe $\Delta f(\vec{x})$ Mapping. (a) Experimental setup using a dielectric probe and XYZ stage on the microwave sensor (LNA and IDC resonator). (b) $x-$ and $y-$ sweep direction along the $(24 \times 24)\,\mathrm{mm}^2$ Microwave sensor surface using a dielectric probe in contact with the IDC resonator. (c) $\Delta f(\vec{x})$ mapping of $(3 \times 1)\,\mathrm{mm}^2$ contact surface area and 30 mm height ROGERS TMM13i $\epsilon_r = 12.85$ dielectric probe. (d) $\Delta f(\vec{x})$ mapping of $(3 \times 10\,\mathrm{mm}^2)$ contact surface area and 30 mm height ROGERS TMM3 $\epsilon_r = 3.27$ dielectric probe. (e) $\Delta f(\vec{x})$ mapping of $(2 \times 1)\,\mathrm{mm}^2$ contact surface area and $30mm$ height ROGERS TMM3 $\epsilon_r = 3.27$ dielectric probe. Two artificial boundaries are defined: Large (LG) boundary containing area and the Small (SM) boundary area.

In Figure 4.2(c), the ROGERS TMM13i evaluation board ($\epsilon_r = 12.85$) with a contact surface area of (3×1) mm^2 is used. The $\Delta f(\vec{x})$ produced by the $\epsilon_r = 12.85$ probe is approximately three times more sensitive in the IDC structure compared to the ROGERS

TMM3 probe with $\epsilon_r = 3.27$ and identical contact surface area, as shown in Figure 4.2(d). Reducing the contact surface area to (2×1) mm^2 for the $\epsilon_r = 3.27$ probe negatively impacts the sensitivity by a factor of approximately three, as observed in Figure 4.2(e).

A comparison of the three mappings was performed by defining two boundaries: a Large (LG) boundary and a Small (SM) boundary, as exemplified in Figure 4.2(e). The LG boundary encompasses the entire $\Delta f(\vec{x})$ response constrained to the total IDC area (20×20) mm^2. The SM boundary is constrained to a (13×16) mm^2 area, which contains the IDC electrodes where the $\Delta f(\vec{x})$ is more pronounced.

Clearly, within the area where the IDC digits are located, the sensitivity is greater for probes with higher ϵ_r values of identical volumes and for larger volumes of identical ϵ_r. As shown in Table 4.1, the average sensitivity increases by approximately 1.6 (1.7) times and variability decreases by approximately 1.7 (2.1) times for $\epsilon_r = 12.85(3.27)$ with the same contact area C, whereas the variability decreases by approximately 1.3 times with an average sensitivity increase of approximately 1.7 for the smaller $\epsilon_r = 3.27$ with a smaller C.

	LGB (20×20)mm^2		*SMB* (13×16)mm^2	
	$\epsilon_r = 3.27$	$\epsilon_r = 12.85$	$\epsilon_r = 3.27$	$\epsilon_r = 12.85$
$C = (2 \times 1)$mm^2				
$\Delta\bar{f}(\vec{x})$ MHz	-0.33	-	-0.55	-
$\sigma^2_{\bar{f}}$ MHz	0.10	-	0.07	-
$C = (3 \times 1)$mm^2				
$\Delta\bar{f}(\vec{x})$ MHz	-0.97	-3.25	-1.66	-5.31
$\sigma^2_{\bar{f}}$ MHz	0.72	6.76	0.35	3.92

Table 4.1: $\Delta\bar{f}(\vec{x})$ and $\sigma^2_{\bar{f}}$ results of LG and SM boundaries of dielectric probes with Contact areas $C = (2 \times 1)\,\text{mm}^2$ and $C = (3 \times 1)\,\text{mm}^2$.

The purpose of defining these boundaries is twofold. Firstly, the SM bounded sensor shows less extreme $\Delta f(\vec{x})$ positional transitions, meaning less variability and higher average sensitivity compared to the LG bounded sensor. Lastly, certain insect species may tend

to traverse near the edges of space, potentially resulting in varying signals for the weaker sensitivity along the edges of the LG boundary compared to the stronger sensitivity of the SM boundary.

4.1.3 Power-Law Dynamics of Insect Activity-Duration Relationship

Tracking the movement or activity of an insect is analogous to observing the energy expenditure over a period of time. The power-duration relationship models the output power that is sustainable for a non-zero time until fatigued [49]. For induced insect movement, the insect activity σ_A can be modeled as a power-law

$$\sigma_A(t_{norm}) = At_{norm}^{-B}. \tag{4.1}$$

Where $A > 0$ is the initial activity parameter and B is the decay parameter. B can be rewritten as $B = |E - 1|$ where $E \in (0, 1)$ is the endurance parameter or how energy is efficiently used for a unit-less non-zero normalized time $t_{norm} > t_0 = 0$. Thus the insect activity-duration relationship can be explained diagrammatically in Figure 4.3, where we first relate the stimulated insect movement from Figure 4.1(c) to a region of time called the *Active Region*. The Active Region represents, from initial stimulation, that the insect is in an energetically unsustainable movement configuration where the insect activity is defined by a decaying power-law. Once the insect is no longer stimulated or unstimulated, the insect moves in an energetically sustainable configuration where the overall insect activity is constant for a time region called the *Spontaneous Region*. The Spontaneous Region of Figure 4.3 relates the discontinuous and spontaneous movement of Figure 4.1(b) where we call the activity as the spontaneous insect activity σ_A^{Sp}.

The purpose of defining the insect activity movement as active or spontaneous is to verify for the first time that insect activity does follow this fundamental law and can be detected by the sensor. Due to the dependence of the sensors frequency on the volumetric size of

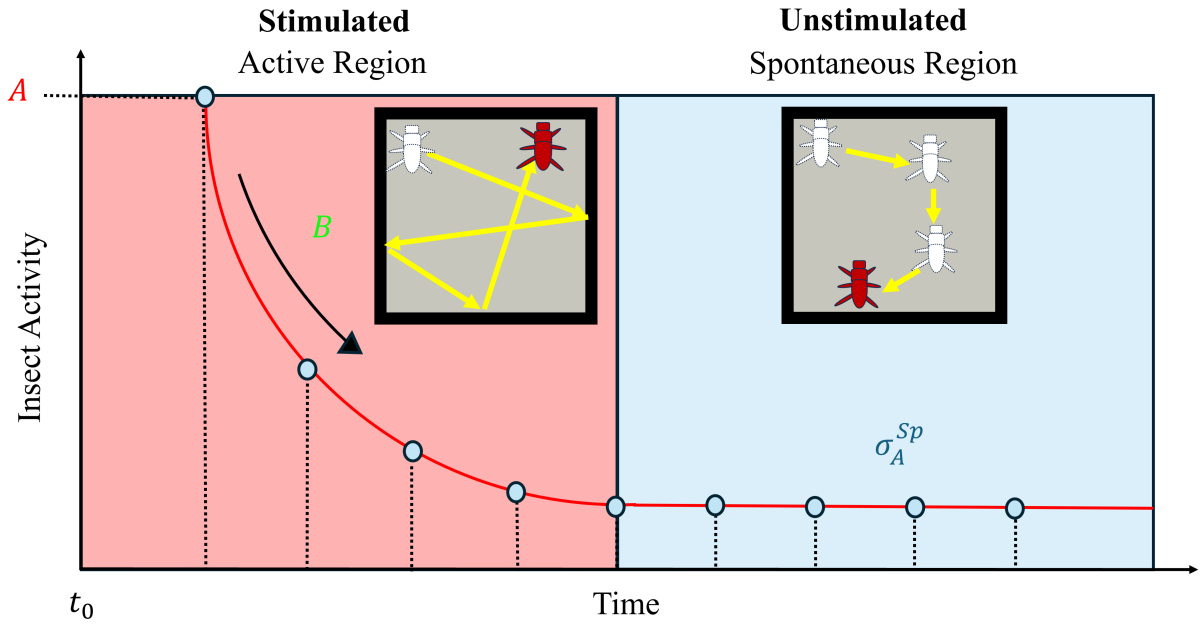


Figure 4.3: Insect Activity-Duration Relationship. (a) Insect activity as a function of time displaying a decaying red-line power-law with insect activity parameter A and decay parameter B for stimulated insect movement within an Active Region of time shaded in red. A flat red-line in shaded-blue Spontaneous Region of time represents the constant spontaneous insect activity σ_A^{Sp} corresponding to unstimulated insect movement.

the dielectric content and its position in contact on the sensor (Figure 4.2(c-e)), the type of insect movement detected will inadvertently influence the Δf and movement-based deviations *df* (Figure 3.8(b)). Hence, using the SM boundary configuration with strong electric-field locations may enhance the insect activity and frequency shift response, whereas the LG boundary configuration with weak electric-field locations along the edges of the boundary may reduce the insect activity and frequency shift response metrics. For insects of different sizes and movement behaviour, we need to test how these regions affect the sensitivity of our metrics.

4.2 Experimental and Measurement Methods

Now, we will discuss the experimental setup and methods used for Chapter 4. The insect detection system described by Figure 3.7 in Chapter 3 is used with minor modifications. A 50

Ω coaxial cable connected from the output port of the microwave sensor to the receiver port of the HackRF One SDR was attenuated with a 30 dBm attenuator to prevent overloading the SDR's ADCs. The digital signal was connected via USB to a laptop, which was programmed using open-source GNU software, identical in structure to the processing flowgraph Figure 3.6 in Chapter 3. Figure 4.4(a) represents the experimental setup used. The f_0 output power, after attenuation, was maintained around -20 dBm observed by the power spectrum of the GUI. The input voltage to produce sustained oscillations was provided by a 5 VDC 1A AC adapter recharging the 3.7 VDC lithium-ion battery that powered the LNA without interruption throughout the experiment. The instantaneous bandwidth of the HackRF set the power spectrum span to 20 MHz, which is the maximum allowable range to observe a frequency shift. After digital signal processing the power spectrum, a single peak frequency f_m data point with a frequency resolution of 610 Hz was recorded every $dt = 1.64$ ms.

The microwave sensor, consisting of the IDC resonator powered by a CPW-backed feedback loop, generated and amplified the microwave signal by an LNA and was fabricated identically to the design outlined in Chapter 3. The large (LG) and small (SM) boundary modifications to the sensing surface were composed of polylactic acid (PLA) filament constructed with a 3D printer, as shown in Figure 4.4(b-c). Both the LG and SM boundaries had outer dimensions of (24×24) mm^2 and a height of 24 mm. The LG boundary had inner dimensions of (20×20) mm^2 and encompassed both the strong electric-field region where the electrodes are located and the weak electric-field region of the outer ring (Figure 4.4(b)). The SM boundary had inner dimensions of (13×16) mm^2 and encompassed only the strong electric-field region of the electrodes (Figure 4.4(c)). The inner boundaries were lined with cellophane adhesive tape to reduce surface roughness and minimize the amount of insect climbing. These boundaries were placed in a holder constructed from PLA to fit the surface dimensions of the sensor.

In the study, two insects common to stored products in Canada were observed in the experiment: the larger adult *T. castaneum*/(Red Flour Beetle, RFB) and the smaller adult *C.*

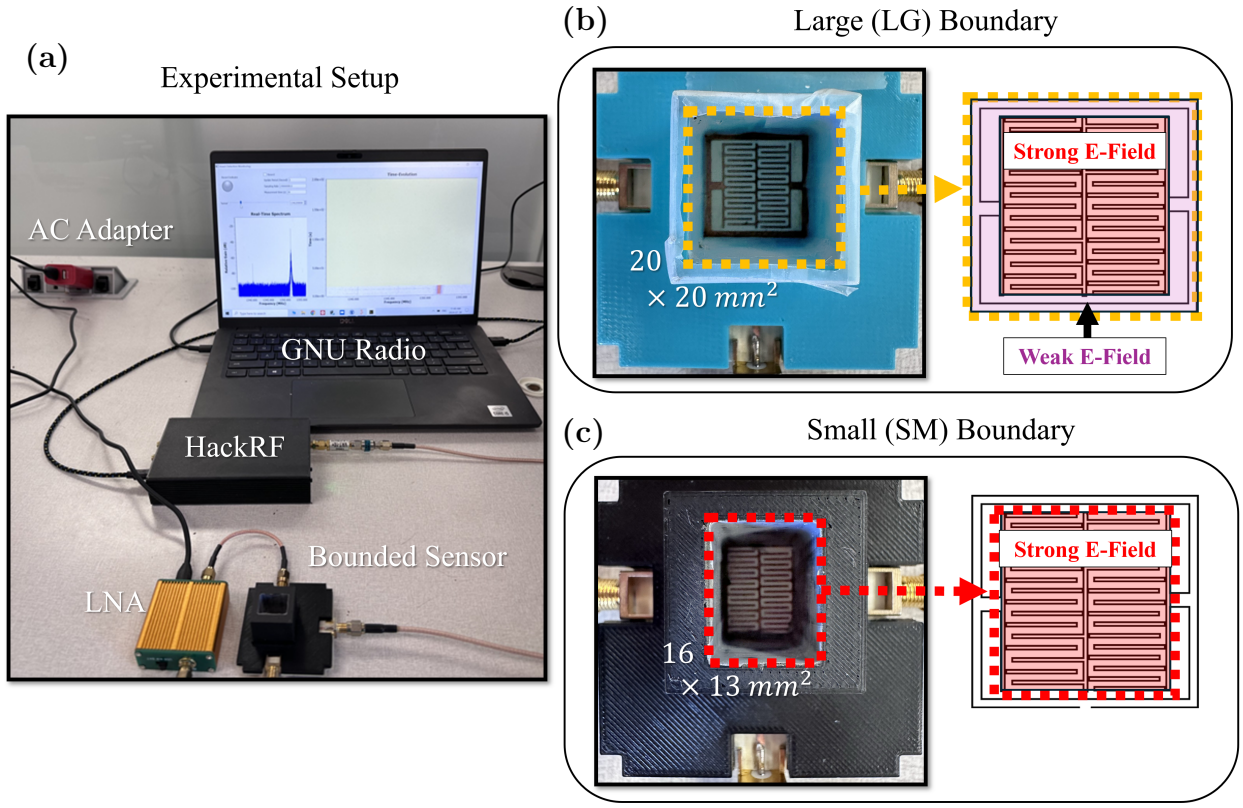


Figure 4.4: Portable Experimental Setup with Different Sized Boundaries. (a) Portable experimental system consisting of a bounded microwave sensor powered via LNA AC/DC rechargeable battery, HackRF One SDR receiver, and GNU interface. (b) Cellophane lined 20×20 mm^2 inner diameter large (LG) boundary sensor configuration. The orange-dotted line represents the bounded strong and weak electric-field locations on the sensor. (c) Cellophane lined 16×13 mm^2 inner diameter small (SM) boundary sensor configuration. The red-dotted line represents the bounded strong electric-field locations on the sensor. The height of both boundaries is 24 mm.

ferrugineus/(Rusty Grain Beetle, RGB). The insects were reared, replenished, and introduced into the sensor following the information provided in Chapter 3. To stimulate insect movement, the insects were forcibly removed from their habitat (sample vial) with metal tweezers, simulating habitat disturbance and predation [65], and dropped into the hole of a lid on the bounded sensor Figure 4.5. The hole was then shielded by a large air-permeable cover to prevent experimental interference from light stimuli of the lab and outdoor day/night cycle lights. For each boundary and each species, 10 independent measurements were taken over a 12-hour period for a single insect. In the counting experiment, 6 independent measurements

were taken for each increment in insect number ($M > 1$, $M = 2, 3, 4, 5$) for both species and both boundaries. To avoid complex results, the insects were added to the sensor at the same time, and the species were never intermingled. All insect and baseline measurements were taken at temperatures near 21°C.

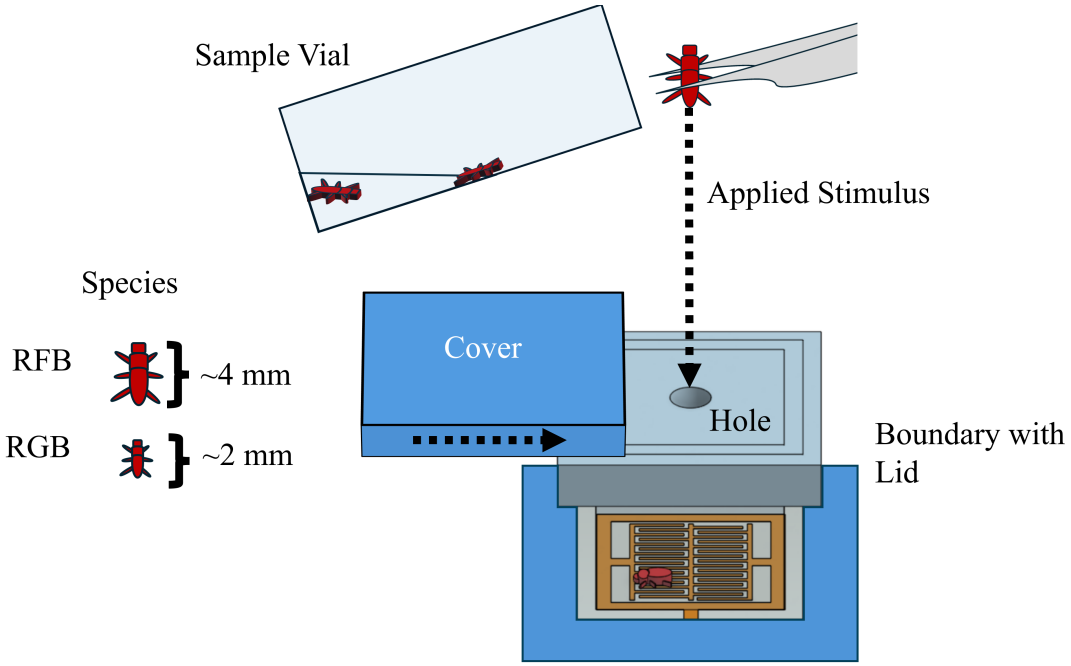


Figure 4.5: Stimulating Insect Movement. Sample vial containing insects of adult RFB (4 mm length) or adult RGB (2 mm length) are forcibly removed and dropped onto sensor to stimulate movement. Bounded microwave sensor with sealed on top by a lid with a hole that is covered to prevent visual light from interfering with insect samples.

The measurement method involves recording $f_m(t_m)$ for 12 hours to capture the system's activity dynamics. Each consecutive f_m data point is separated by $dt = 1.64\,\text{ms}$, ensuring the detection of any insect movement. Two key quantities are measured: the average frequency shift

$$\Delta\bar{f} = \frac{1}{N}\sum_{m=1}^{N}(f_m - f_0). \tag{4.2}$$

and the df/dt sample standard deviation or insect activity

$$\sigma_A = \sqrt{\frac{1}{N-1}\sum_{m=1}^{N}\left(\frac{df_m}{dt} - \frac{\bar{df}}{dt}\right)^2}. \tag{4.3}$$

Equation 4.2 and Equation 4.3 are observed for time intervals T by breaking data into smaller segments to visualize trends, reduce noise, and analyze patterns over time. Multiple static normalized time intervals $T_i = [t_{(i-1)N}, t_{iN-1}]$ are used to look at short-term behaviour for every i^{th} time interval of data size $m = N$. Where the time prior to insect detection is t_0 and the point of detection is t_1 defined previously by Figure 3.8(b). This timing method is first used experimentally with the insect activity Equation 4.3 to verify the insect activity-duration relationship of both insect species using both bounded sensor configurations. Later, when noisy frequency shift analysis is used with insect activity, a cumulative timing method based on expanding time intervals $T_{int} = [t_0, t_{iN-1}]$ will be implemented to look at long-term data trends and filter short-term fluctuations.

It is important to point out that in Chapter 3, we defined the instantaneous insect activity level as $|df/dt|$ for the full time-series. Now that we want to look at time intervals T of a time-series, we can examine the data distribution. This frequency time-derivative produces a distribution centred at $d\bar{f}/dt$ for a given T, with the spread of the data represented by the sample standard deviation $\sigma_A(T)$ or insect activity, which reflects the fluctuations in the frequency magnitude rate of change in Equation 4.3. A large σ_A indicates heightened activity, leading to many large frequency shifts associated with insect and sensor interactions. A low σ_A suggests less activity, closer to the noise level of the bare system, indicating less insect and sensor interactions with smaller frequency shifts. Thus, σ_A is our definition of insect activity and is used for the rest of this thesis.

The time-series was segmented into intervals to observe the overall dynamical trend with T_{int} values of $[1, 5, 15, 30, 60, 120, 240, 360, 480, 720]$ minutes. A baseline was established for $\Delta\bar{f}$ and σ_A for both LG and SM boundaries using 10 independent measurements taken over 12 hours (Figure 4.6). The df/dt at $T_{int} = 1$ minute distributions centred near $d\bar{f}/dt = 0$ showed

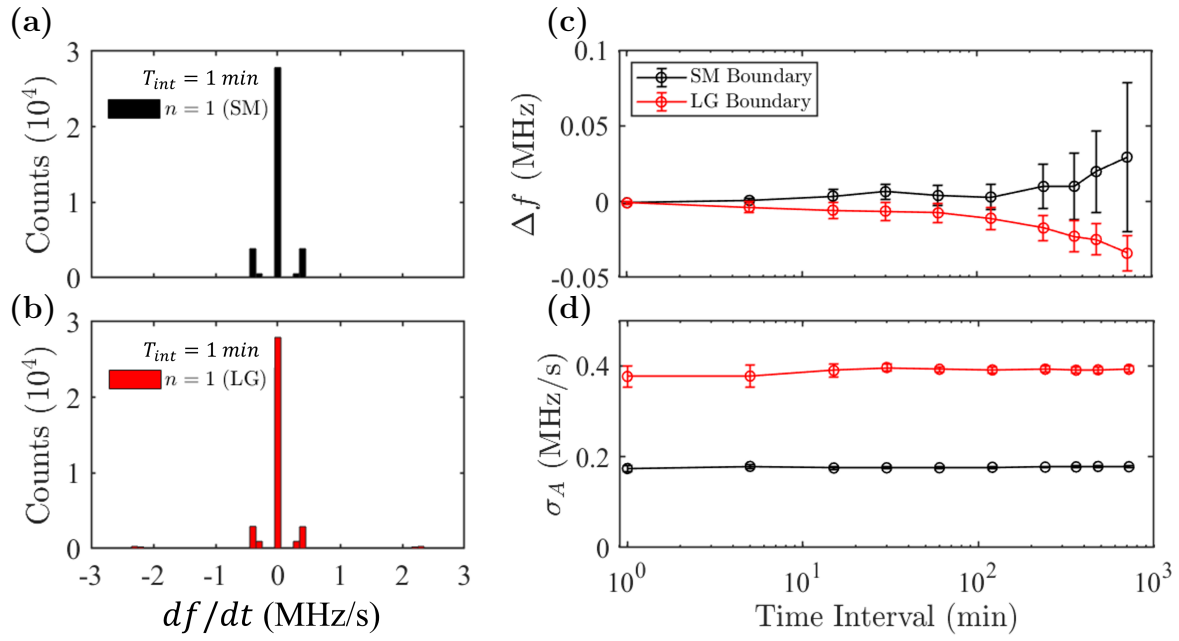


Figure 4.6: Baseline Sensor Measurements with both Boundaries σ_A and $\Delta\bar{f}$ absent insects over discrete time intervals T_{int}. (a) SM boundary df/dt histogram distribution at $T_{int} = 1$ min sample $n = 1$. (b) LG boundary df/dt histogram distribution at $T_{int} = 1$ minute sample $n = 1$. (c) $\Delta\bar{f}$ trend for 10 12hr SM and LG sample measurements over 10 time intervals.(d) σ_A trend for 10 12hr SM and LG sample measurements over 10 time intervals. Time intervals $T_{int}[min] = [1, 5, 15, 30, 60, 120, 240, 360, 480, 720]$.

minimal noise variation of the SM boundary (Figure 4.6(a)) with slightly elevated variability of the LG boundary (Figure 4.6(b)). Increasing T_{int}, there is a noticeable drifting frequency effect seen in Figure 4.6(c) for long T_{int} for both boundaries most likely due to environmental factors such as temperature. For instance, $\Delta\bar{f}^{Bare}_{SM} = (-700 \pm 60)$ Hz and $\Delta\bar{f}^{Bare}_{LG} = (-870 \pm 80)$ Hz at $T_{int} = 1$ minute, but $\Delta\bar{f}^{Bare}_{SM} = (30 \pm 40)$ kHz and $\Delta\bar{f}^{Bare}_{LG} = (-34 \pm 10)$ kHz at $T_{int} = 720$ minutes for the SM and LG boundary configurations, respectively. As well, the heightened variability of the LG boundary baseline signal $\sigma^{Bare}_{A,LG} = (0.38 \pm 0.02)$ MHz/s at $T_{int} = 1$ minute compared to the smaller $\sigma^{Bare}_{A,SM} = (0.174 \pm 0.007)$ MHz/s SM boundary signal is exemplified in Figure 4.6(d). This excess noise is possibly due to the different PLA boundary holders used in which case the holder could be in contact with SMA connector grounded components. In all cases, for an insect signal to be analyzed we seek $\Delta\bar{f}$ and σ_A values larger than baseline.

4.3 T.Castaneum / Red flour beetles (RFB)

The ability to infer the species of insect pest and the level of infestation non-destructively is crucial for determining appropriate treatment methods in integrated pest management (IPM), including applications in grain handling, food processing facilities, restaurants, and hotels. Microwave-based sensors have already demonstrated the capability to detect disturbance levels based on insect size, as discussed in Chapter 3, in a portable and practical manner. Moving forward, extracting quantifiable information from a continuously evolving system requires addressing the complexity of insect activity and frequency shift responses. Here we first investigate the Red Flour Beetle (RFB), around 4 mm in length, oval-shaped, and a common pest that feeds on damaged and whole grain kernels found in-and-outside of grain and food processing facilities [62].

4.3.1 RFB Insect Activity

The RFB's insect activity was recorded from the point of detection t_1 for 12 hours, divided into 720 intervals of $T_i = 1$ minutes each using the static time interval method. Two time regions were defined: the Active Region, characterized by energetically unsustainable transient activity, and the Spontaneous Region, where activity remains constant and energetically sustainable. This analysis was conducted for both the SM and LG boundaries, with $M \in [1, 5]$ RFB insects.

In Figure 4.7, we observed the activity of a single insect over 720 one-minute intervals. The Active Region was identified by elevated σ_A levels, while the Spontaneous Region was defined as the period before the active boundary, where σ_A remained relatively constant. A shaded interval is provided by:

$$\hat{y}^i = \hat{y} \pm t_{\alpha/2,df} \cdot \text{S.E.}(\hat{y}), \tag{4.4}$$

where $t_{\alpha/2,df}$ is the critical value of the Student's t-distribution for a given degree of freedom (df). The standard error for a 95% confidence level ($\alpha = 0.05$) is S.E.$(\hat{y}(\hat{\beta}))$ dependent on the estimated coefficients $\hat{\beta}$ for a confidence interval (C.I.) about $\hat{y}(\hat{\beta})$. Whereas a prediction interval (P.I) incorporates both the estimated coefficients and variability of the predictor $\mathbf{x}$ seen by the standard error S.E.$(\hat{y}(\mathbf{x}, \hat{\beta}))$, about $\hat{y}(\mathbf{x}, \hat{\beta})$. The P.I. shaded regions are bound around the predicted value of the insect activity $\hat{y}^{int} = \sigma_A$ using the predictor T_i from Equation 4.4 in Figure 4.7 to estimate where future data points may fall.

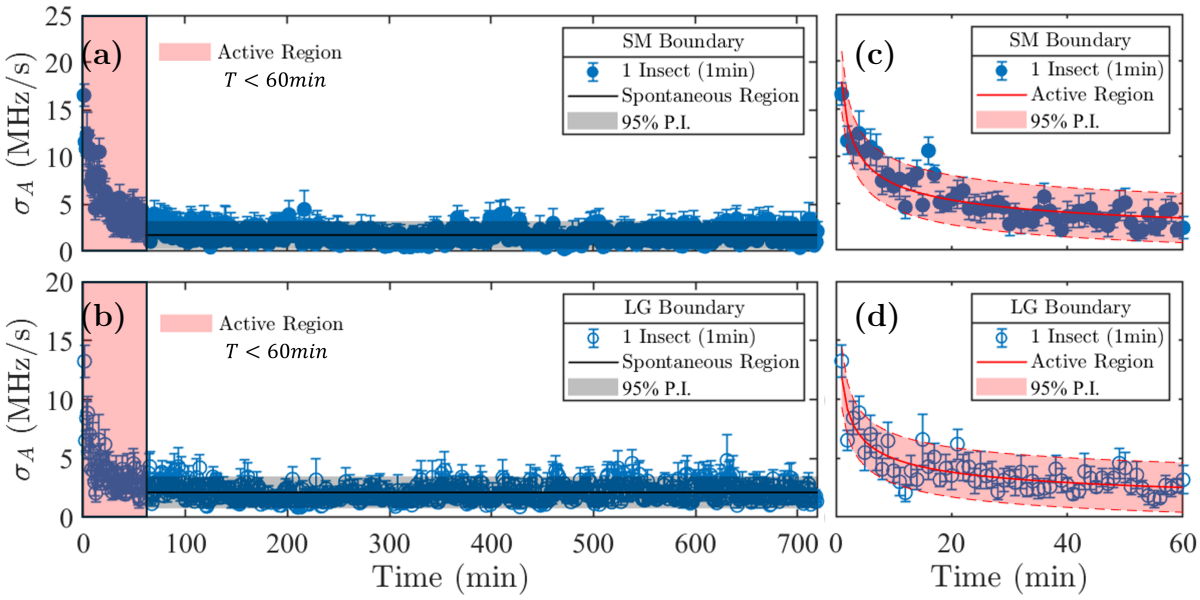


Figure 4.7: SM and LG Boundary RFB Insect Activity σ_A. (a,b) SM(LG) boundary σ_A for 720 minutes using $T_i = 1$ minute intervals. Heightened σ_A defined at $T < 60$ minute in shaded red as Active Region. Mean σ_A defined at $T > 60$ minute by solid black line with black shaded 95% Prediction Interval for the Spontaneous Region.(c,d) SM(LG) boundary σ_A within the Active Region fit with power law function $\sigma_A = At_{norm}^{-B}$ represented by a red line bounded by 95% Prediction Interval shaded in red.

In Figure 4.7(a,b), the transition from high to low insect activity occurs at $T = 60$ minutes of both boundaries, after which σ_A stabilizes, as shown by the horizontal black line and shaded prediction interval. Prior to 60 minutes, the Active Region is defined; beyond 60 minutes the Spontaneous Region is also defined. The values found within the Spontaneous

Region were $\sigma_{A,SM}^{Sp} = (1.7 \pm 0.8)\,\text{MHz/s}$ and $\sigma_{A,LG}^{Sp} = (2.1 \pm 0.7)\,\text{MHz/s}$ for the SM and LG boundaries, respectively. The results show that $\sigma_A^{Sp} > \sigma_A^{Bare}$, indicating that insect activity is significantly higher when an insect is present on the sensor.

Before $T = 60\,\text{min}$, σ_A^{Act} peaks at $T = 1\,\text{min}$ for both SM and LG boundaries within the Active Region, as shown in Figure 4.7(c,d). This suggests that the frequency shift rate of change is highly variable, reflecting intense insect movement that gradually decays to a constant level by $T = 60$ minutes. The movement dynamics are fitted using the insect activity-duration power-law model from Equation 4.1, represented by the solid red line and shaded prediction interval in Figure 4.7(c,d), where A is the initial activity parameter, and B is the decay constant. The unit-less time $t_{norm,i} = T_i/\tau$ from Equation 4.1 is used with τ being the time-normalization constant such that the initial activity parameter A retains its MHz/s units.

The goodness of fit for the power-law model in the Active Region was $R_{SM}^2 = 0.8192$ with $A_{SM} = (17.9 \pm 0.9)\,\text{MHz/s}$ and $B_{SM} = 0.40 \pm 0.02$ for the SM boundary, and $R_{LG}^2 = 0.7300$ with $A_{LG} = (11.9 \pm 0.7)\,\text{MHz/s}$ and $B_{LG} = 0.38 \pm 0.02$ for the LG boundary. $A_{SM} > A_{LG}$ indicates that the SM bounded sensor has a greater response towards single RFB insect activity.

This is investigated further, we examine the insect activity for $M = 1, 2, 3, 4, 5$ RFBs (with 6 sample measurements for $M = 2, 3, 4, 5$). We begin by assessing whether the power-law activity-duration relationship holds for multiples of M. As with the case for 1 RFB, $T < 60$ minutes was designated as the Active Region, $T > 60$ minutes was designated as the Spontaneous Region, the insect activity-duration relationship using a power-law fit was applied to the Active Region, and constant line insect activity fit was applied to the Spontaneous Region. Results are tabulated in Table 4.2, where it becomes clear that using the SM boundary configuration results in an initial activity A from the power-law fit that is much larger than the A fit using the LG boundary configuration. Additionally, the R^2 correlation coefficient fits much better to the data using the SM boundary. The decay coefficient B decreases and

activity coefficient A increases with RFB number from the fit. Since the $p-value$ for both A and B are below the significance threshold ($p < 0.05$), the power-law model fit is statistically significant. Similarly, the spontaneous insect activity σ_A^{Sp} increases with insect number, but the differences between choice of boundary appear marginal.

	Active Region				*Spontaneous Region*
	$A \pm S.E.$ (MHz/s)	$B \pm S.E.$	R^2	$p-value$ (A&B)	$\sigma_A^{Sp} \pm S.E.$ (MHz/s)
$SM(RFB)$					
1	17.9±0.9	0.40±0.02	0.8192	<0.001	1.7±0.8
2	23.7±0.9	0.347±0.015	0.8677	<0.001	3.0±1.2
3	29.7±1.0	0.282±0.012	0.8668	<0.001	4.4±1.9
4	36.1±1.1	0.306±0.011	0.9096	<0.001	5.5±1.7
5	31.9±1.0	0.300±0.012	0.8870	<0.001	5.8±1.4
$LG(RFB)$					
1	11.9±0.7	0.38±0.02	0.7300	<0.001	2.1±0.7
2	11.4±0.7	0.24±0.02	0.6276	<0.001	1.7±0.9
3	18.1±0.8	0.308±0.016	0.8141	<0.001	3±3
4	25.1±1.0	0.222±0.013	0.7965	<0.001	5.3±1.6
5	25.1±0.9	0.249±0.012	0.8487	<0.001	5±2

Table 4.2: σ_A^{Act} Active Region At_{norm}^{-B} fit and Spontaneous Region constant σ_A^{Sp} results for $M = 1, 2, 3, 4, 5$ RFBs in SM and LG boundaries.

To examine the fitted and statistical parameter relationships more closely, the A and σ_A^{Sp} were fit using the weighted least squares (WLS) linear regression functions of insect number by $A(M) = A'M + A'_o$ and $\sigma_A^{Sp}(M) = S_{\sigma_A^{Sp}}M + \sigma_o^{Sp}$, respectively. Here we use a 95% Confidence Interval (C.I.) from Equation 4.4. Insect activity is a non-linear function, as $\sigma_A \to 0$ for $M = 0$ insects; however, here we approximate a linear region for $M \in [1, 5]$. Graphical representations of A, B, and σ_A^{Sp} are provided in Figure 4.8, with corresponding fit

results in Table 4.3.

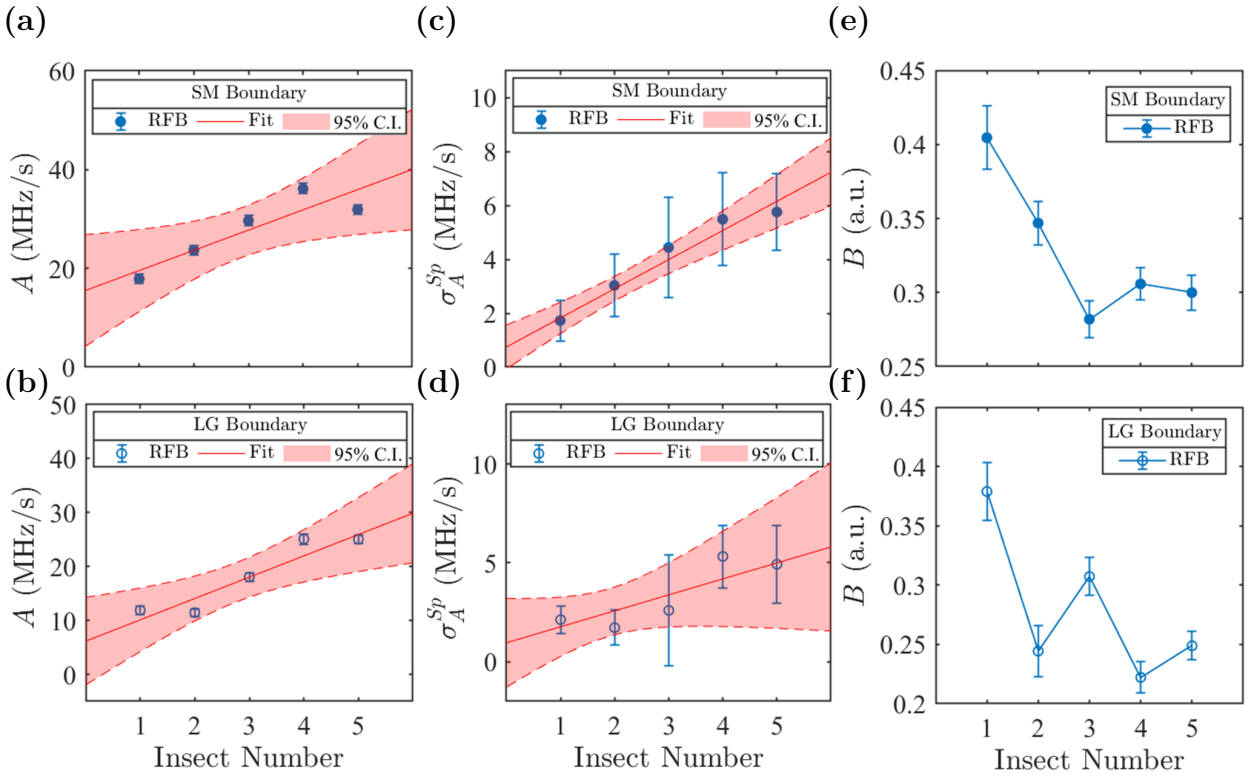


Figure 4.8: RFB Insect Activity Relationship with Insect Number. Plotted using fit results from Table 4.2 for $M = 1, 2, 3, 4, 5$ RFBs. $A(M) = A'M + A'_o$ fit via solid red line with shaded red 95% confidence interval region in (a) SM boundary and (b) LG boundary. $\sigma_A^{Sp}(M) = S_{\sigma_A^{Sp}} M + \sigma_o^{Sp}$ fit via solid red line with shaded red 95% confidence interval region in (c) SM boundary and (d) LG boundary. Decay coefficient B for (e) SM boundary case and (f) LG boundary case.

The initial activity $A(M)$ as a function of insect number demonstrates a positive correlation with insect number, as seen in Figures 4.8(a) and 4.8(b). A larger intercept $A'_{o,SM} > A'_{o,LG}$ is determined for the SM boundary case, but an equal sensitivity [1] $A'_{SM} \sim A'_{LG}$ is observed between both boundaries. In the Spontaneous Region, due to significant error, the sensitivity $S_{\sigma_A^{Sp}}$ and intercept σ_o^{Sp} are similar using both boundaries; however, they do display a positive correlation with insect number 4.8(c,d). The $p - value$ associated with sensitivity and $A'_{o,SM}$ was statistically significant, but had weak significance in $S^{Sp}_{\sigma_{A,LG}}$ and the intercepts within the

[1] Throughout this thesis, when using linear fits, sensitivity refers to the slope of the fit.

Active and Spontaneous Region. Although no fit was applied to the decay constant B, it appears to decrease with insect number for both boundaries, as shown in Figures 4.8(e) and 4.8(f). Let $B = |E - 1|$, where E is the endurance parameter [50]. This would indicate that E increases with insect number, suggesting that a greater number of insects, regardless of the boundary used, affects movement on a collective scale.

	Initial Activity $A(M)$					*Spontaneous Activity* $\sigma_A^{Sp}(M)$				
	$A' \pm S.E.$ (MHz/s)	$A'_o \pm S.E.$ (MHz/s)	R^2	$p-value$ A'	$p-value$ A'_o	$S_{\sigma_A^{Sp}} \pm S.E.$ (MHz/s)	$\sigma_0^{Sp} \pm S.E.$ (MHz/s)	R^2	$p-value$ $S_{\sigma_A^{Sp}}$	$p-value$ σ_o^{Sp}
$SM(RFB)$	4.1±1.1	15±4	0.8177	0.04	0.02	1.08±0.10	0.7±0.3	0.9759	0.0016	0.06
$LG(RFB)$	4.0±0.8	6±3	0.8852	0.017	0.09	0.8±0.3	1.0±0.7	0.6897	0.08	0.3

Table 4.3: Initial Activity $A(M) = A'M + A'_o$ and Spontaneous Activity $\sigma_A^{Sp}(M) = S_{\sigma_A^{Sp}}M + \sigma_o^{Sp}$ fit results for $M = 1, 2, 3, 4, 5$ RFBs in SM and LG boundaries from Figure 4.8.

In summary of this subsection, we observed that the power-law activity-duration relationship holds for 1-to-5 RFBs using both SM and LG bounded microwave sensors in the Active Region. Beyond 60 minutes, the insect activity is lower and is constant within the Spontaneous Region. In the approximately linear region for $M \in [1, 5]$ RFBs, the initial activity $A(M)$ is positively correlated with RFB number, and the initial activity sensitivity does not change with the chosen boundary. However, the intercept or initial activity level to the RFB insect is much larger when using the SM boundary. Additionally, the endurance parameter E appears to increase collectively with insect number, suggesting that more insects affect movement on an individual level for RFBs. Lastly, in the Spontaneous Region, the spontaneous insect activity $\sigma_A^{Sp}(M)$ is positively linearly correlated with insect number and has a sensitivity and spontaneous insect activity level (intercept) that do not depend on the type of boundary used, indicating a preference for the SM boundary onset insect activity of the RFB.

4.3.2 RFB σ_A *vs.* $\Delta\bar{f}$ Relationship

The evolutionary dynamics of insect activity provide insight into the amount of detectable movement occurring on the sensor. To gather information about the size of the dielectric content being detected, we examine $\Delta\bar{f}$ and σ_A, specifically, how the transition from more movement to less movement influences the frequency response. This is best observed by using the cumulative timing method for expanding the interval over which data are collected to filter out smaller short-term fluctuations and reveal long-term trends for σ_A and $\Delta\bar{f}$ first for a single RFB insect, then for 1-to-5 RFBs.

Here, observing the time-series data of a single RFB for both SM and LG bounded sensors, as the time interval expands to include more data, insect activity retains visually its general decaying power-law trend, as shown in Figure 4.9 (a, c), with the highest activity at $T_{int} = 1\,\text{min}$ decaying over time to the lowest activity at $T_{int} = 720\,\text{min}$, remaining constant for both boundaries. The frequency response, shown in Figure 4.9 (b, d), is at a minimum (maximum absolute $\Delta\bar{f}$) at $T_{int} = 1\,\text{min}$, increasing to a maximum (minimum absolute $\Delta\bar{f}$) at $T_{int} = 60\,\text{min}$, after which $\Delta\bar{f}$ decreases for the remaining time intervals for both SM and LG boundary configurations. Correlating the dynamics of both σ_A and $\Delta\bar{f}$ in Figure 4.9 (e, f) shows that as insect activity decreases, the absolute values of the frequency shift response also decrease. A turning point appears at $T_{int} = 60\,\text{min}$, which we define as the inflection interval T_{inf}, marking the transition from a negative to a positive correlation between σ_A and $\Delta\bar{f}$.

The errors plotted in Figure 4.9 are represented by the standard error $S.E. = \frac{1}{\sqrt{n}}\sqrt{\text{Var}(\bar{x})}$, where x is the predictor and n is the number of experimental trials. A more detailed description of the error, accounting for movement distributed around $\Delta\bar{f}$, is shown by the blue-shaded region in Figure 4.9 (e, f), with the pooled standard error $S.E._p = \frac{1}{\sqrt{n}}\sqrt{\text{Var}(\Delta\bar{f}_n) + \text{Avg}(\sigma_f^n)}$. This pooled error arises from the total movement needed to generate the central tendency of $\Delta\bar{f}$, which is already accounted for by σ_A, and thus is excluded from any further error propagation.

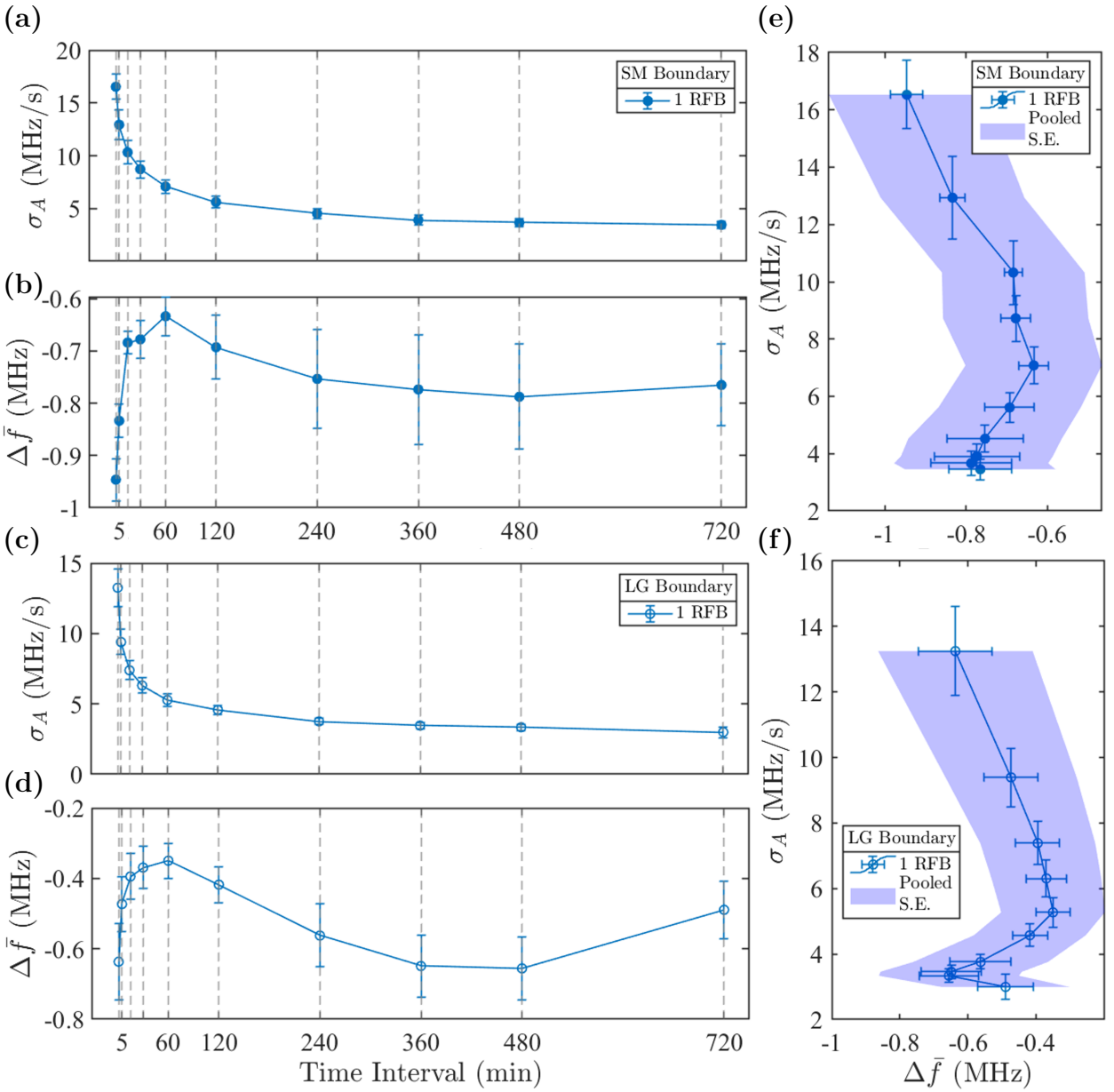


Figure 4.9: σ_A **and** $\Delta\bar{f}$ **Dynamics as a Function of Time Interval for a Single RFB.** The time interval $T_{int}[min] = [1, 5, 15, 30, 60, 120, 240, 360, 480, 720]$ is represented by the vertically dashed gray lines in (a-d), with standard error of the mean represented by error bars in (a-f), and blue shaded $\Delta\bar{f}$ pooled standard error. (a) σ_A *vs.* T_{int} for SM bounded sensor. (b) $\Delta\bar{f}$ *vs.* T_{int} for SM bounded sensor.(c) σ_A *vs.* T_{int} for LG bounded sensor. (d) $\Delta\bar{f}$ *vs.* T_{int} for LG bounded sensor. (e,f) σ_A *vs.* $\Delta\bar{f}$ plots with vertically descending data points for ascending T_{int} intervals. (e)σ_A *vs.* $\Delta\bar{f}$ for SM boundary. (f) σ_A *vs* $\Delta\bar{f}$ for LG boundary.

These results suggest that for $T_{int} < T_{inf}$, the system is in the Active Region, where $\Delta\bar{f}$ reflects the insect's interaction with a large portion of the sensing area. The maximum

frequency shift $\Delta\bar{f}_{SM} = (-0.95 \pm 0.04)$ MHz and $\Delta\bar{f}_{LG} = (-0.64 \pm 0.11)$ MHz occurring at $T_{int} = 1$ minute when the insect activity is at its highest $\sigma_{A,SM} = (16.5 \pm 1.1)$ MHz/s and $\sigma_{A,LG} = (13.2 \pm 1.4)$ MHz/s. When $T_{int} = T_{inf}$, the system is transitioning to a time region that is dominated by spontaneous movement of the Spontaneous Region and the frequency shift is at a minimum of $\Delta\bar{f}_{SM} = (-0.63 \pm 0.04)$ MHz and $\Delta\bar{f}_{LG} = (-0.35 \pm 0.05)$ MHz occurring at $T_{int} = 60$ minutes, with a near minimum insect activity seen within both boundaries. Hence, when $T_{int} = T_{inf}$, the system is approaching the Spontaneous Region and the frequency shift response is influenced by sparse insect activity and interaction with the sensor. This indicates that the frequency shift response is affected by where the insect spends most of its time relative to specific sensor locations.

For the continuously decreasing insect activity with time before stabilizing at long time intervals, the frequency shift is initially decreasing in magnitude but begins to increase at the inflection interval before stabilizing at longer time intervals. An interpretation of the inflection point at inflection interval $T_{inf} = 60$ minutes suggests the transition from active dominated movement towards spontaneous dominated movement. Where once the movement of the insect is spontaneous and discontinuous, their resting positioning becomes unpredictable and may stay stationary on more sensitive areas of the sensor for prolonged periods of time, resulting in an increase in frequency shift magnitude at longer time intervals.

Now we investigate whether additional features emerge in the σ_A vs. $\Delta\bar{f}$ relationship as the number of RFBs increases. Additionally, we will examine the relationship between $\Delta\bar{f}(M)$ and $\sigma_A(M)$ as a function of the insect number and examine how the boundary size can influence the sensor's sensitivity to particular insect movement.

As was done for a single RFB insect, the $\sigma_A\, vs.\, \Delta\bar{f}$ characteristic curve was constructed using longer time intervals. For 1-to-5 RFBs, using the SM and LG bounded microwave sensors, the characteristic curves were plotted in Figure 4.10. Within each curve for a specific insect number, each sequential data point is connected graphically by a line to indicate the progression from the left-to-right (small-to-large) time intervals used. As before, the shaded

region represents the pooled standard error due to insect movement, which is excluded from the error analysis. Figure 4.10(a) indeed shows a larger frequency shift response $\Delta\bar{f}$ and insect activity σ_A that are dependent on T_{int}. As insect activity decreases, a negative-to-positive correlation inflection point in the frequency response occurs at $T_{\text{inf}} = 60$ minutes ($T_{\text{inf}} = 30$ minutes for $M = 2$) for 1-to-5 RFBs. This suggests that the inflection point is a repeating feature with 1-to-5 insects using the SM bounded configuration. Conversely, using the LG bounded sensor, the inflection point is lost beyond $M > 1$ RFBs, and any characteristic curve repetitiveness is unobserved with increased insect number, as shown in Figure 4.10(b). It is observable that $\Delta\bar{f}$ and insect activity σ_A do increase with insect number using the LG bounded sensor, but the magnitude is smaller compared to the SM bounded sensor. Additionally, modeling the behavior of insects with an increasing number of RFBs using these curves is significantly more complex with the LG bounded case, as the curves begin to intersect with each other as insect numbers increase.

Next, we aim to demonstrate how the frequency shift response and insect activity are sensitive to insect number and whether this changes with longer time intervals used in Figure 4.10. From Equation 2.30, a WLS linear fit was applied via $\Delta\bar{f}(M) = S_{\Delta\bar{f}}M$ as a function of $M \in [1, 5]$ RFB insects with 95% confidence intervals for all time intervals and both sized boundaries. Starting with the SM bounded microwave sensor, Figure 4.11(a) at $T_{\text{int}} = 1$ minute shows the greatest sensitivity $S_{\Delta\bar{f}} = (-1.08 \pm 0.03)$ MHz. The LG bounded case is much less sensitive, as seen in Figure 4.11(b), where $S_{\Delta\bar{f}} = (-0.51 \pm 0.07)$ MHz at $T_{\text{int}} = 1$ minute. We approximate a linear region of the insect activity for $M \in [1, 5]$ RFB insect numbers. Insect activity was fit using a WLS linear regression model via $\sigma_A(M) = S_{\sigma_A}M + \sigma_o$ as a function of RFB number with 95% confidence intervals. Starting with the SM bounded case again, Figure 4.11(c) shows the sensitivity and intercept in relation to RFB number where found to be $S_{\sigma_A} = (4.5 \pm 0.9)$ MHz/s and $\sigma_o = (14 \pm 3)$ MHz/s at $T_{\text{int}} = 1$ minute. Similarly, for the LG bounded case, the sensitivity was observed in Figure 4.11(d) at $T_{\text{int}} = 1$ minute, where $S_{\sigma_A} = (4 \pm 1)$ MHz/s and $\sigma_o = (6 \pm 3)$ MHz/s. Notice here the greater

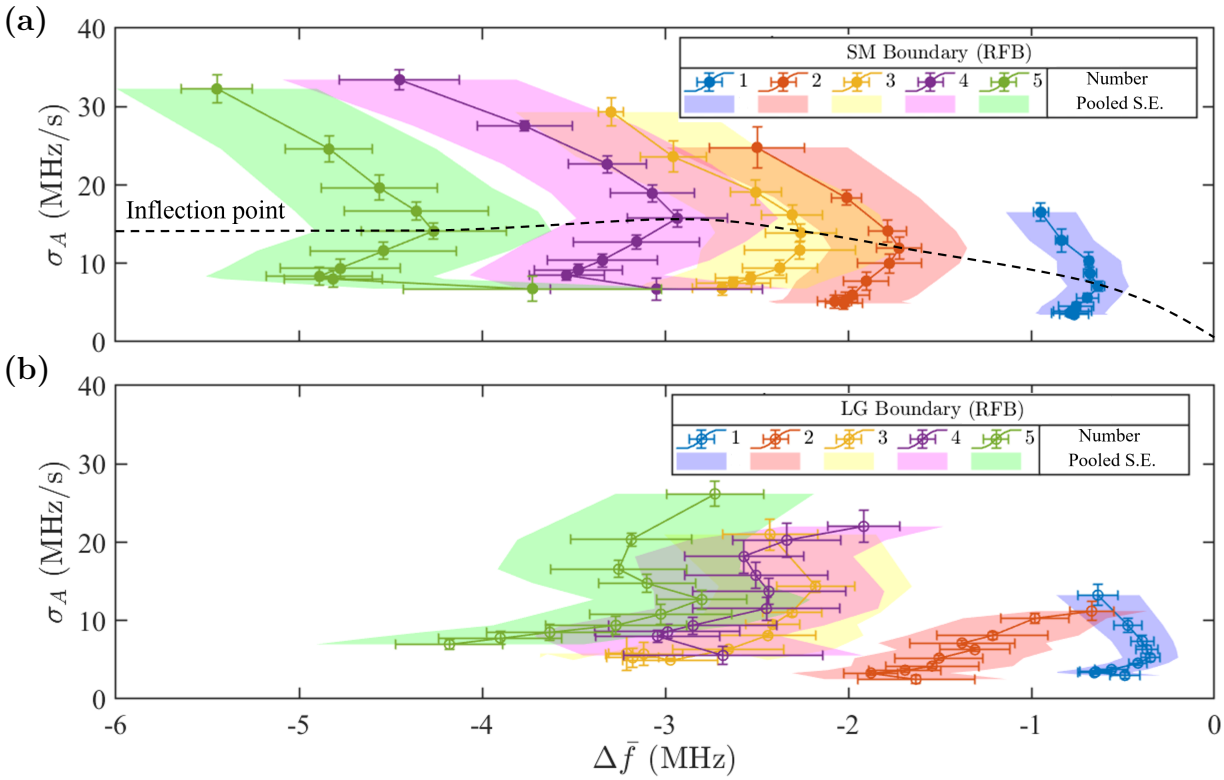


Figure 4.10: σ_A *vs.* $\Delta\bar{f}$ **Plot for** $M = 1, 2, 3, 3, 5$ **RFBs.** σ_A *vs.*$\Delta\bar{f}$ relationship colour-coded for multiple RFBs using different boundaries with shaded $\Delta\bar{f}$ pooled standard errors (a) SM boundary. Inflection point represented by dotted black line at $T_{inf} = 60$ minutes ($T_{inf} = 30$ minutes $M = 2$). (b) LG Boundary. Absent consistent inflection point.

frequency shift sensitivity in Figure 4.11(a) compared to 4.11(b) as well as the near identical insect activity sensitivity in 4.11(c) and 4.11(d), but much larger intercept in 4.11(c) at a 1 minute time interval.

Expanding the number of linear fits applied to the frequency shift response and insect activity by the number of time intervals used in Figure 4.10, demonstrates that $\Delta\bar{f}$ and σ_A are time interval-dependent. This time dependency is directly observed in Figure 4.12 for both SM and LG bounded sensors; each data point corresponds to the fitted sensitivities ($S_{\Delta\bar{f}}$, $S_{\sigma A}$, and σ_o) and S.E. as a function of T_{int}. Figure 4.12(a) demonstrates the greater frequency shift sensitivity $S_{\Delta\bar{f}}$ of the SM boundary than the LG boundary. Where the greatest $S_{\Delta\bar{f}}$ occurs at $T_{int} = 1$ minutes. The inflection point is retained at $T_{int} = t_{inf} = 60$ minutes with absolute minimum frequency shift sensitivity for the SM bounded sensor. The

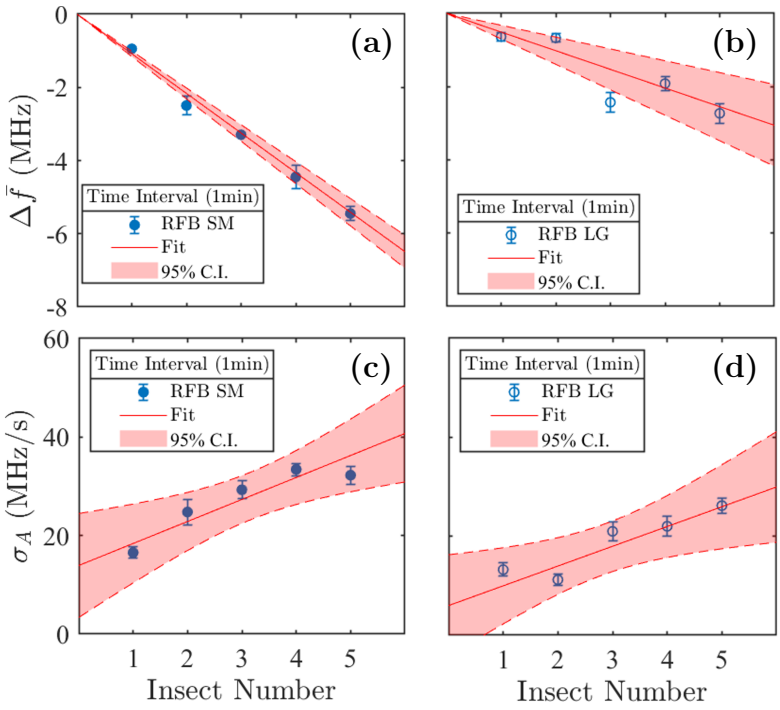


Figure 4.11: $\Delta\bar{f}$ and σ_A *vs.* M RFB at $T_{int} = 1$ minute. Weighted least-squares regression solid red line fit of frequency shift $\Delta\bar{f} = S_{\Delta\bar{f}}M$ and insect activity $\sigma_A = S_{\sigma_A}M + \sigma_o$ with 95% confidence interval shaded red region for $T_{int} = 1$ minute (a) $\Delta\bar{f}$ SM boundary (b) $\Delta\bar{f}$ LG boundary. (c) σ_A SM boundary. (d) σ_A LG boundary.

LG bounded sensor exhibits a non-linear-like decreasing $S_{\Delta\bar{f}}$ trend for longer time intervals, losing the inflection point at $T_{inf} = 60$ minutes from Figure 4.9(d). In general, the fitted $S_{\Delta\bar{f}}$ is statistically significant with all $p - values < 0.01$; however, the $\Delta\bar{f}$ linear regression coefficient R^2 fits the data for all time intervals much better using the SM bounded sensor than the LG bounded sensor seen in Appendix A. For instance, at $T_{int} = 1$ minute, the R^2 of $\Delta\bar{f}$ using the SM bounded sensor exhibits an $R^2_{SM} = 0.9919$ much closer to 1 when compared to the weaker $R^2_{LG} = 0.7885$ of the LG bounded sensor. Figure 4.12(b) represents the insect activity sensitivity S_{σ_A}, retaining the power-law like activity-duration relationship trend, shows no real significant enhancement towards sensitivity depending on boundary size used. However, the insect activity level observed by the intercept σ_o is enhanced using the SM boundary microwave sensor (Figure 4.12(c)). In Appendix A, the linear fitted R^2 is not too dissimilar between the choice of boundary, rarely larger than $R^2 > 0.9$ suggesting a weaker fit.

However, for the fitted $S_{\sigma A}$ they are generally statistically significant ($p-value \leq 0.05$) for all time intervals, but the p-value for the fitted σ_o is for the most part not statistically significant and performs worse for the LG bounded configuration (Appendix A). The non-significant $p-values(> 0.05)$ suggests that either the current linear model may not adequately describe the data or additional samples are needed to provide a more reliable estimation of the insect activity relationship with number.

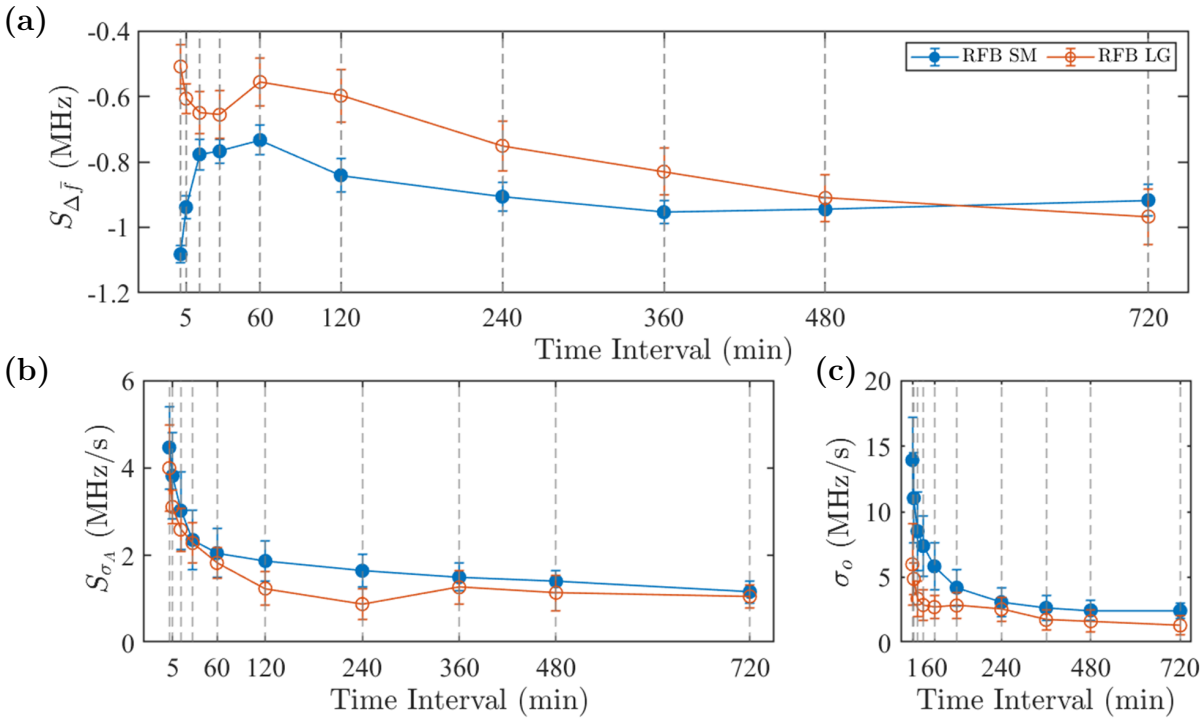


Figure 4.12: $S_{\Delta\bar{f}}$, $S_{\sigma A}$, **and** σ_o, *vs.* T_{int} **for RFB.** Linear fitting parameters of Figure 4.10 with S.E. as a function of T_{int} for both boundaries. (a) $S_{\Delta\bar{f}}$, (b) $S_{\sigma A}$, and (c) σ_o.

In summary, for a single RFB insect forcibly placed in the sensor, the insect activity-duration followed a power-law relationship within the Active Region and became constant in the Spontaneous Region. Increasing the number of RFB insects to 1-to-5 resulted in a sensitivity towards insect activity that did not depend on the boundary configuration, although the magnitude of the initial activity parameter was larger with the SM boundary case. Additionally, the overall system's endurance appeared to increase with the number of

RFB insects, suggesting that a greater number of insects will influence the energy expenditure on an individual level. Constructing a σ_A vs. $\Delta\bar{f}$ characteristic curve to model the RFB behaviour of the response signal over longer time intervals revealed an inflection point at $T_{\text{inf}} = 60$ minutes in both bounded configurations. This characteristic inflection point signified the transition from Active-to-Spontaneous movement from the continuously decreasing insect activity that in turn influenced the frequency shift by the unpredictability of the resting position of the insect. However, the inflection interval was only retained in the SM bounded configuration for increased RFB insect numbers, while the LG bounded configuration did not display any characteristic features. Furthermore, WLS linear fits applied to the frequency shift response and insect activity as a function of insect number demonstrated a time interval-dependency. The frequency shift matched the linear model well, and the sensitivity using the SM boundary was greater than the LG boundary and demonstrated a retained inflection interval characteristic, whereas the LG boundary did not. The insect activity sensitivity did not depend on the boundary used, but the initial insect activity level is much larger using the SM bounded sensor. However, the linear model need be investigated further to verify activity and number relationship. Thus, the SM bounded sensor provides greater enhancement towards frequency shift and insect activity for shorter time intervals for the RFB and demonstrates time-dependent characteristics when compared to the LG bounded sensor.

4.4 C. Ferrugenius / Rusty grain beetles (RGB)

A common primary feeder of stored products, the much smaller *Cryptolestes ferrugineus*, or Rusty Grain Beetle (RGB), is found across Canada and is also prevalent worldwide [39]. Approximately 2 mm in length, with a rusty brown colour and a flat, rectangular body shape, these beetles tend to feed on damaged whole grains such as oats, barley, and wheat [63]. They have a severe economic impact by feeding on the nutrient-rich germ within the grain,

reducing its weight and quality. The experimental approach from the previous section is repeated here to make a qualitative and quantitative comparison of insect activity, frequency shift response, and their relationship with insect number to be compared with the larger RFB at the end of this chapter.

4.4.1 RGB Insect Activity

To begin this subsection, the Rusty Grain Beetle (RGB) insect activity was first investigated using both LG and SM boundary configurations. The insect activity for a single RGB insect and multiple RGB insects $M \in [1, 5]$ using both bounded microwave sensors was performed identically to the experimental technique applied to the RFB.

In Figure 4.13, there is an initial heightened insect activity that decreases over time in both boundary scenarios. For the SM boundary configuration, Figure 4.13(a) shows that there is a visually defined heightened region prior to $T < 60$ minutes which we have identified as the Active Region before. Beyond $T > 60$ minutes, the insect activity is constant which was previously called the Spontaneous Region; the activity $\sigma_{A,SM}^{Sp} = (1.3 \pm 0.4)$ MHz/s with shaded prediction intervals becomes energetically sustainable for the RGB. For $T < 60$ minutes, the RGB insect activity is heightened or energetically unsustainable, decaying according to the power law in Equation 4.1 using $t_{norm} = T/\tau$, as seen in Figure 4.13(c), which is identical in form to the SM and LG boundary RFB cases. The RGB insect activity within the active region using the SM boundary had an initial amplitude of $A = (6.0 \pm 0.3)$ MHz/s and a decay constant of $B = 0.262 \pm 0.017$ for the first 60 1-minute intervals, with a correlation coefficient of $R_{SM}^2 = 0.7500$ and shaded prediction interval. Contrasting with the LG boundary configuration, the power-law insect activity-duration relationship was unobservable (indicating a poor fit) for 10 RGB trials.

Examining the LG boundary configuration, we find two regions of heightened activity before reaching the energetically favorable activity in the Spontaneous Region beyond $T > 270$ minutes. Each region was associated with a 95% prediction interval, where the Spontaneous

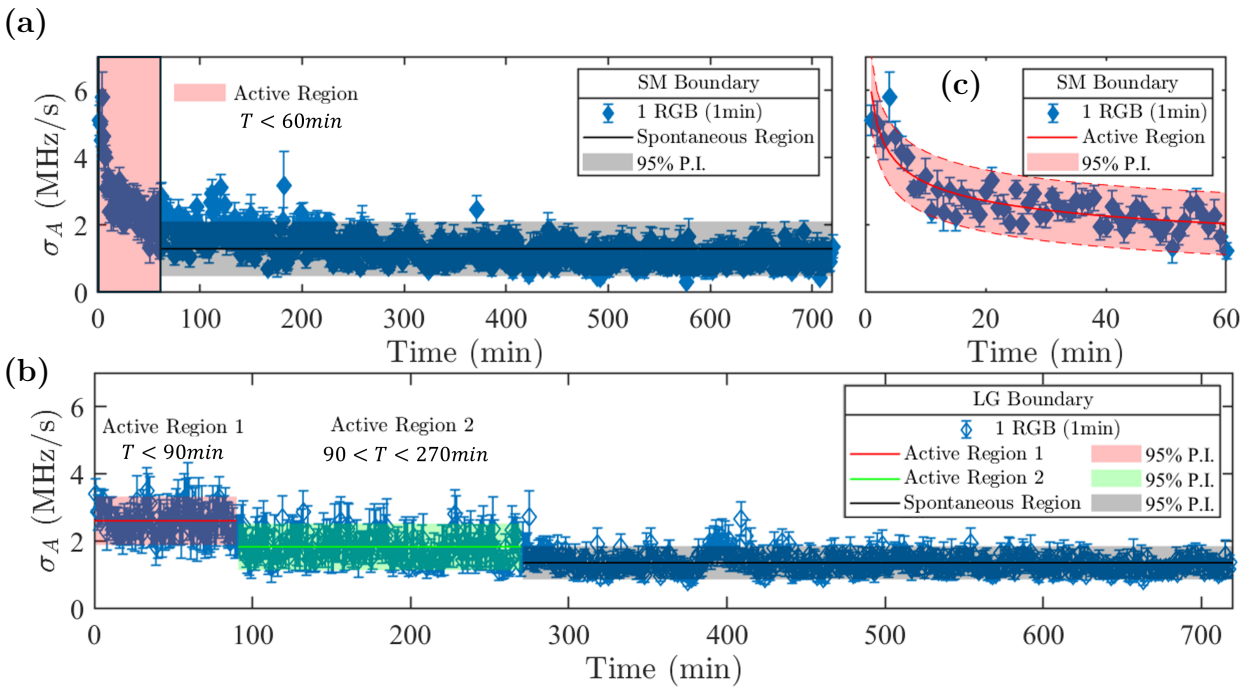


Figure 4.13: SM and LG Boundary Insect Activity σ_A of RGB for $T_i = 1$ minute. (a) SM boundary σ_A over 720 minutes. The heightened decaying σ_A is marked as the Active Region for $T < 60$ minutes, shaded in red. The mean σ_A for $T > 60$ minutes, representing the Spontaneous Region, is shown as a solid black line with a 95% prediction interval shaded in black. (b) LG boundary σ_A over 720 minutes, showing two active regions. Active Region 1 is defined for $T < 90$ minutes, and Active Region 2 is between $90 < T < 270$ minutes. The mean σ_A in Active Region 1 is represented by a solid red line with a 95% prediction interval shaded in red, while the mean σ_A in Active Region 2 is shown by a solid green line with a 95% prediction interval shaded in green. The Spontaneous Region for $T > 270$ minutes is indicated by a solid black line with a 95% prediction interval shaded in black. No decaying σ_A is observed. (c) SM boundary σ_A in the Active Region is fit with a power-law function $\sigma_A = At_{norm}^{-B}$, represented by a solid red line with a 95% prediction interval shaded in red.

Region insect activity becomes constant at $\sigma_{A,LG}^{Sp} = (1.4 \pm 0.3)$ MHz/s, as shown in Figure 4.13(b). Active Region 1 occurs from the time of detection to $T < 90$ minutes, and Active Region 2 occurs between 90 minutes $< T <$ 270 minutes. Both regions exhibit constant activity levels of $\sigma_{A,SM}^{Act1} = (2.6 \pm 0.4)$ MHz/s and $\sigma_{A,LG}^{Act2} = (1.8 \pm 0.4)$ MHz/s, respectively.

The power-law activity duration model is primarily inconsistent for the LG boundary case due to the sensor's inability to detect smaller insects in areas with weaker sensitivities

from the poor insect-electric-field interaction, such as the outer IDC along the LG boundary wall-sensor interface. However, there is no difference between the choice of boundary within the Spontaneous Region $\sigma^{Sp}_{A,SM} \sim \sigma^{Sp}_{A,LG}$. In contrast, the SM boundary confines the area to regions with stronger dielectric interactions, indicating an SM boundary preference for detectable insect movement. In addition to 10 sample trial measurements for a single RGB in each boundary scenario, 6 further samples were recorded, each lasting 720 minutes, for up to $M = 2, 3, 4, 5$ RGBs in both the SM and LG boundaries. With $T_i = 1$ minute intervals, we examine how activity duration changes with the number of insects.

In both boundary scenarios, insect activity changes with an increasing number of RGBs, though this effect is less pronounced in the LG boundary configuration. A power-law relationship of the activity-duration was used to model the RGB insect activity within the Active Region $T < 60$ minutes, as indicated by the solid line fits in Figure 4.14(a). Unlike in the SM boundary case, the power-law relationship within LG boundary's active region does not fit well for 1 RGB (see Figure 4.13(c)) and also for 2 RGBs (fit for $T < 60$ minutes). Therefore, power-law fitting was omitted for RGB insect activity for LG boundary case, as illustrated in Figure 4.14(b). The spontaneous region activity for 1 to 5 RGBs in the LG boundary [2] is consistently defined for $T > 270$ minutes. All fit results are summarized in Table 4.4. The $p - value < 0.001$ associated with the fitted coefficients indicated a statistical significance within the Active Region of the insect activity power-law fit.

For RGB numbers $M \in [1, 5]$, the initial activity parameter A in the SM bounded sensor and the spontaneous insect activity σ^{Sp}_{A} of both boundaries are positively correlated, as shown in Figures 4.15(a), (c), and (d). A WLS linear regression model was applied to the data, with shaded 95% confidence intervals for the fits. In Figure 4.15(a), the SM bounded sensor's Active Region fits are applied for $A(M) = A'M + A'_o$, where A' is the initial activity slope (sensitivity) and A'_o is the initial insect activity level. Similarly, for the Spontaneous Region insect activity of both bounded sensors, the fits are given by $\sigma^{Sp}_{A}(M) = S_{\sigma^{Sp}_{A}} M + \sigma^{Sp}_{o}$ seen in

[2] The total time is from 270 min to 720 min only for the spontaneous region measurements

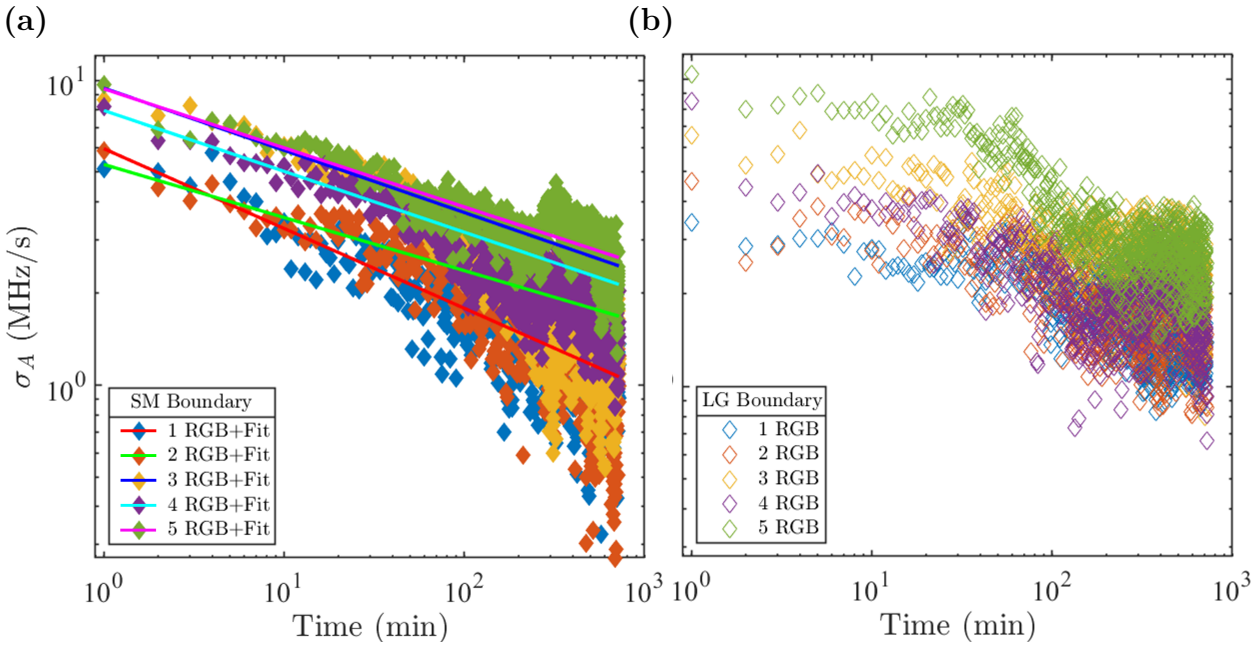


Figure 4.14: Insect Activity Dynamics for Multiple RGBs. A log-log plot of σ_A time evolution for $M = 1, 2, 3, 4, 5$ RGBs using a time interval $T_i = 1$ minute fit with a power law duration relationship $\sigma_A^{Act} = At_{norm}^{-B}$ for each M. Absent error bars and prediction interval for clarity. (a) σ_A time evolution for SM boundary configuration for $M = 1, 2, 3, 4, 5$ RGBs with solid markers and solid line fits. (b) σ_A time evolution for LG boundary configuration for $M = 1, 2, 3, 4, 5$ RGBs with hollow markers and no fits.

Figures 4.15(c) and (d). All fitting results are tabulated in the accompanying Table 4.5.

A'_{SM} is approximately three times more sensitive than $S_{\sigma_A^{Sp}}$ towards RGB movement within the Spontaneous Region for both boundaries. Likewise, the intercept $A'_{o,SM}$ in the Active Region is greater than both intercepts σ_o^{Sp} of the Spontaneous Region. A comparison can be made with the intercept $A'_{o,SM}$ with the constant insect activity $\sigma_{A,LG}^{Act1}$ of the LG boundary; and it was found that $A'_{o,SM} > \sigma_{A,LG}^{Act1}$, although, due to the poor fit for $A(M)$ the large intercept error results in a not very significant comparison. In addition to the statistically weak $p - values$ of both fitted $A(M)$ coefficients, it suggests that more data be acquired or a different model be investigated. Similarly, the spontaneous insect activity sensitivity $S_{\sigma_A^{Sp}}$ for both boundaries is indistinguishable and consistent within their experimental error. Here, the fitted coefficients of the spontaneous insect activity are statistically significant ($p \leq 0.05$). Extracted from the power-law activity-duration relationship, the decay constant

	Active Region				*Spontaneous Region*
	$A \pm S.E.$ (MHz/s)	$B \pm S.E.$	R^2	$p-value$ (A&B)	$\sigma_A^{Sp} \pm S.E.$ (MHz/s)
$SM(RGB)$					
1	6.0±0.3	0.262±0.017	0.7469	<0.001	1.3±0.4
2	5.3±0.2	0.174±0.014	0.6748	<0.001	1.5±0.5
3	9.4±0.3	0.204±0.009	0.8742	<0.001	1.7±0.6
4	8.0±0.2	0.200±0.008	0.8886	<0.001	1.9±0.4
5	9.4±0.3	0.194±0.011	0.8368	<0.001	3.0±0.7
$LG(RGB)$					
1	-	-	-	-	1.4±0.5
2	-	-	-	-	1.7±0.9
3	-	-	-	-	2.5±1.1
4	-	-	-	-	1.9±0.9
5	-	-	-	-	2.6±1.0

Table 4.4: σ_A^{Act} Active Region At_{norm}^{-B} fit and spontaneous region constant σ_A^{Sp} results for $M = 1, 2, 3, 4, 5$ RGBs in SM and LG boundaries.

B demonstrates as a decreasing function with RGB number, as seen in Figure 4.15(b). This suggests that as the number of insects and initial activity increase, the rate at which insect activity decays over time becomes more rapid to reach a constant insect activity within the Spontaneous Region. The decay constant B when written in the endurance parameter form $B = |E - 1|$ indicates, like for the RFB case, that as more RGBs are added, the system endurance E collectively increases, meaning that a greater number influences insect movement individually.

To summarize this section, the power-law activity duration relationship held using the SM bounded microwave sensor for 1-to-5 RGBs. However, was not used to model the activity duration relationship for the LG boundary configuration and observed 2 separate Active Regions for a single RGB. The SM boundary case was observed to exhibit a positive correlation

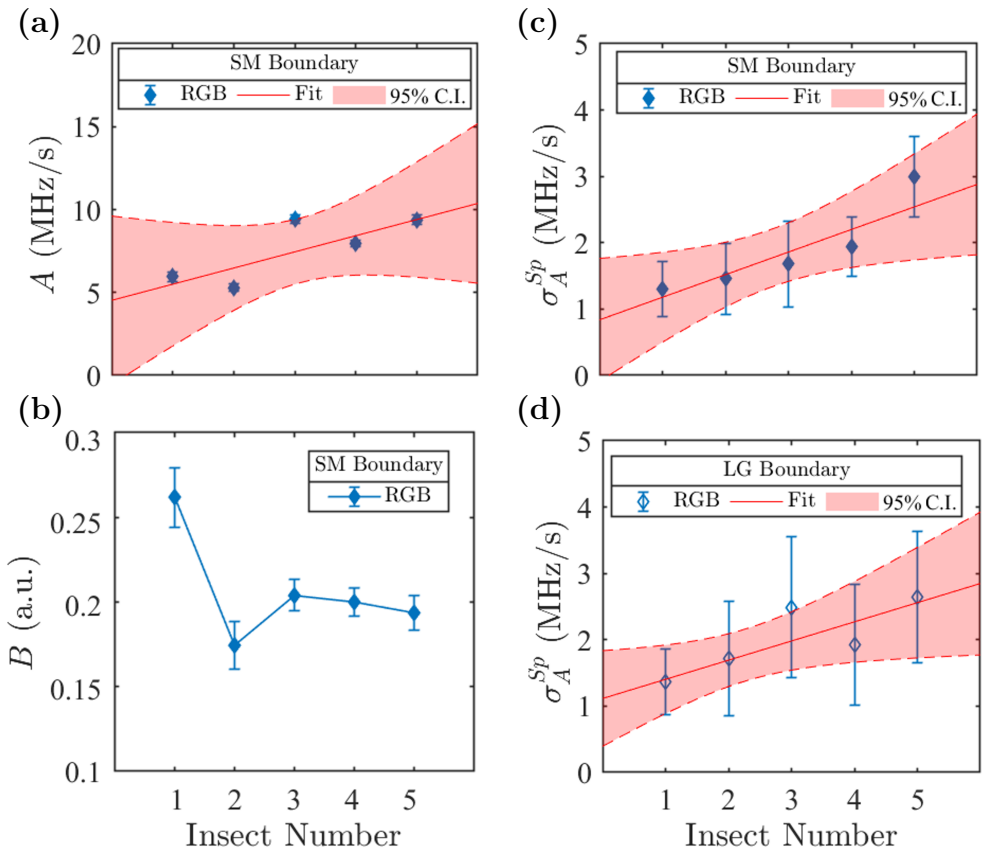


Figure 4.15: RGB Insect Activity Relationship with Insect Number. Plotted using fit results from Table 4.4 for $M = 1, 2, 3, 4, 5$ RGBs. (a) $A(M) = A'M + A'_o$ fit via solid red line with shaded red 95% confidence interval region for SM boundary case. (b) Scaling power law decay coefficient for SM boundary case. (c) $\sigma_A^{Sp}(M) = S_{\sigma_A^{Sp}} M + \sigma_o^{Sp}$ fit via solid red line with shaded red 95% confidence interval region for SM boundary case. (d) $\sigma_A^{Sp}(M) = S_{\sigma_A^{Sp}} M + \sigma_o^{Sp}$ fit via solid red line with shaded red 95% confidence interval region for LG boundary case.

with initial insect activity $A(M)$ and RGB number. The Active Region 1 constant insect activity was found to be smaller than the intercept of the fitted $A(M)$ of the SM bounded sensor, but was much larger than the LG boundary cases' spontaneous activity intercept. This indicates that the onset RGB activity has a higher detectability using the SM boundary. However, there appeared to be no enhancement noticeable towards sensitivity and initial activity response for a chosen boundary within the Spontaneous Region. The endurance parameter E appeared to increase with the increase of RGB number.

	Initial Activity $A(M)$					*Spontaneous Activity* $\sigma_A^{Sp}(M)$				
	$A' \pm S.E.$ (MHz/s)	$A'_o \pm S.E.$ (MHz/s)	R^2	$p-value$ A'	$p-value$ A'_o	$S_{\sigma_A^{Sp}} \pm S.E.$ (MHz/s)	$\sigma_o^{Sp} \pm S.E.$ (MHz/s)	R^2	$p-value$ $S_{\sigma_A^{Sp}}$	$p-value$ σ_o^{Sp}
$SM(RGB)$	1.0±0.5	4.5±1.6	0.5823	0.13	0.07	0.34±0.09	0.8±0.3	0.8153	0.04	0.05
$LG(RGB)$	-	-	-	-	-	0.29±0.08	1.1±0.2	0.7967	0.04	0.016

Table 4.5: Initial Activity $A(M) = A'M + A'_o$ and Spontaneous Activity $\sigma_A^{Sp}(M) = S_{\sigma_A^{Sp}}M + \sigma_o^{Sp}$ fit results for $M = 1, 2, 3, 4, 5$ RGBs in SM and LG boundaries from Figure 4.15.

4.4.2 RGB σ_A vs. $\Delta\bar{f}$ Relationship

To understand how insect activity influences the frequency shift response for a single RGB, the values of σ_A and $\Delta\bar{f}$ are averaged over increasing time intervals from the t_0 the point prior to first detection t_1 to smooth out short-term fluctuations to reveal long-term trends via the previously used cumulative timing method. The time intervals used are identical to those in the RFB case, $T_{int} = [1, 5, 15, 30, 60, 120, 240, 360, 480, 720]$ minutes. We begin again with a single RGB insect sampled 10 times over 720 1-minute time intervals using both SM and LG bounded microwave sensors.

Using the cumulative timing method reveals that insect activity, using the SM boundary, visually follows a power law-like trend, as shown in Figure 4.16(a). For the SM boundary, there is a maximum insect activity occurring at $T_{int} = 1$ minute, which then decays to a minimum at $T_{int} = 720$ minutes. The RGB frequency shift response in Figure 4.16(b) shows a brief dip in $\Delta\bar{f}$ at $T_{int} = 1$ minute, followed by an increase to a maximum absolute $\Delta\bar{f}$ at $T_{int} = 5$ minutes, before decreasing to a minimum absolute $\Delta\bar{f}$ at $T_{int} = 60$ minutes within the Active Region. Beyond $T_{int} > 60$ minutes, the absolute $\Delta\bar{f}$ begins to increase again. Figure 4.16(e) demonstrates the correlation between σ_A and $\Delta\bar{f}$, with standard error bars indicating central tendency and a blue-shaded area representing pooled standard error of total movement variability which is neglected in the error analysis. A negative-to-positive correlation inflection point at $T_{int} = T_{inf} = 60$ minutes emerges between σ_A and $\Delta\bar{f}$. However, between $T_{int} = 1$ minute and $T_{int} = 5$ minutes, there is a positive correlation between activity and frequency response, which shifts to a negative correlation in the following time interval

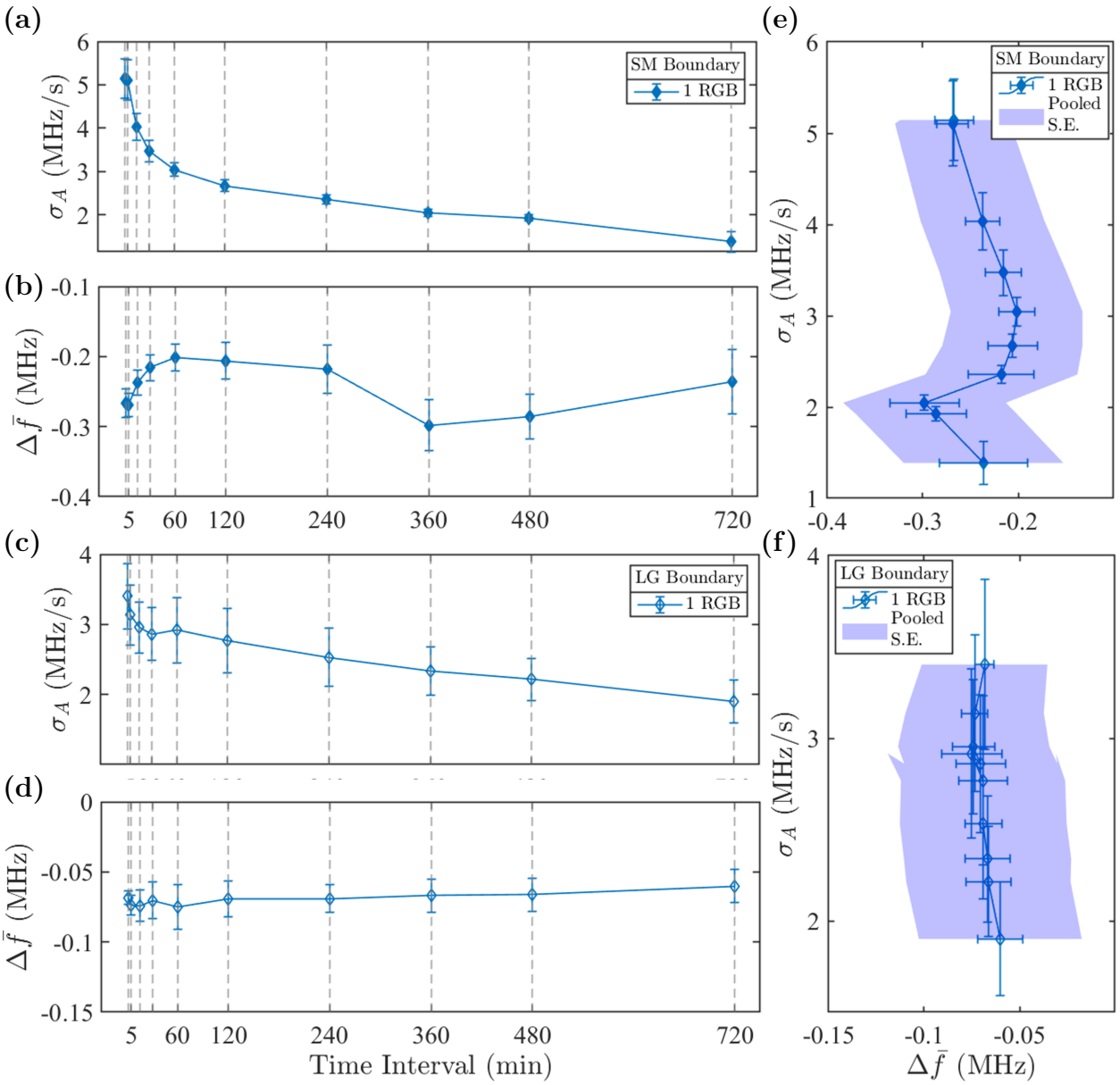


Figure 4.16: σ_A and $\Delta\bar{f}$ Dynamics as a Function of Time Interval for a Single RGB. The time interval $T_{int}[min] = [1, 5, 15, 30, 60, 120, 240, 360, 480, 720]$ is represented by the vertically dashed gray lines in (a-d), with standard error of the mean represented by error bars in (a-f), and blue shaded $\Delta\bar{f}$ pooled standard error. (a) σ_A *vs.* T_{int} for SM boundary. (b) $\Delta\bar{f}$ *vs.* T_{int} for SM boundary.(c) σ_A *vs.* T_{int} for LG boundary. (d) $\Delta\bar{f}$ *vs.* T_{int} for LG boundary. (e,f) σ_A *vs.* $\Delta\bar{f}$ plots with vertically descending data points for ascending T_{int} intervals. (e) σ_A *vs.* $\Delta\bar{f}$ for SM boundary. (f) σ_A *vs.* $\Delta\bar{f}$ for LG boundary.

T_{int} = 15 minutes. Although the error prohibits a clear determination of the correlation between T_{int} = 1 minute and T_{int} = 5 minutes, $T_{int} = T_{inf'} = 5$ minutes are defined as

the anti-inflection interval occurring at the anti-inflection point, which may not be readily apparent for a single RGB but will become clearer with multiple RGBs in the following section.

In contrast to the SM case, as shown in Figure 4.16(c), the LG boundary exhibits a decrease in insect activity with increasing time intervals that does not visually follow the power-law trend observed in the SM boundary case. Similarly, the $\Delta\bar{f}$ response appears approximately constant regardless of time intervals, as seen in Figure 4.16(d). This relationship is clearly observable in Figure 4.16(e), where, as σ_A decreases, $\Delta\bar{f}$ remains insensitive to activity, maintaining a constant $\Delta\bar{f} \sim -0.75$ MHz. The pooled standard error shaded region remains small, with an interval size of approximately 0.75 MHz, roughly $\sim |\Delta\bar{f}|$.

An interpretation of the inflection point occurring at $T_{inf} = 60$ minutes for the RGB remains the same for the RFB case; that as insect activity is decreasing, there is a transition from active dominated movement to spontaneous dominated movement. Where the insect may begin to rest more on areas with stronger electric-field regions, causing the previously decreasing frequency shift magnitude to increase at longer time intervals. The anti-inflection interval at $T_{inf'} = 5$ minutes suggests a different behaviour from the signal detected than the RFB. During the experiment, it was observed that at the onset of RGB insect movement, they often traced the perimeter of the boundary and could be later found closer to the middle where the strong electric-field regions are within the electrodes. This suggests that the RGB insect on average approaches the positions of the electrodes at $T_{inf'} = 5$ minutes, causing the increase in frequency shift magnitude. This and the fact that the LG boundary configuration has significantly weaker electric-field regions along the perimeter and the frequency shift does not seem to respond to insect movement for all time intervals is a possible indicator that the RGB insect is prone to locations near the edges of the bounded sensor.

Now, we look at insect activity and frequency shift response as a function of longer time intervals for $M \in [1, 5]$ RGBs. The 5 characteristic RGB curves of σ_A vs. $\Delta\bar{f}$ are bounded by shaded pooled standard errors for the corresponding insect number, as shown in Figure 4.17.

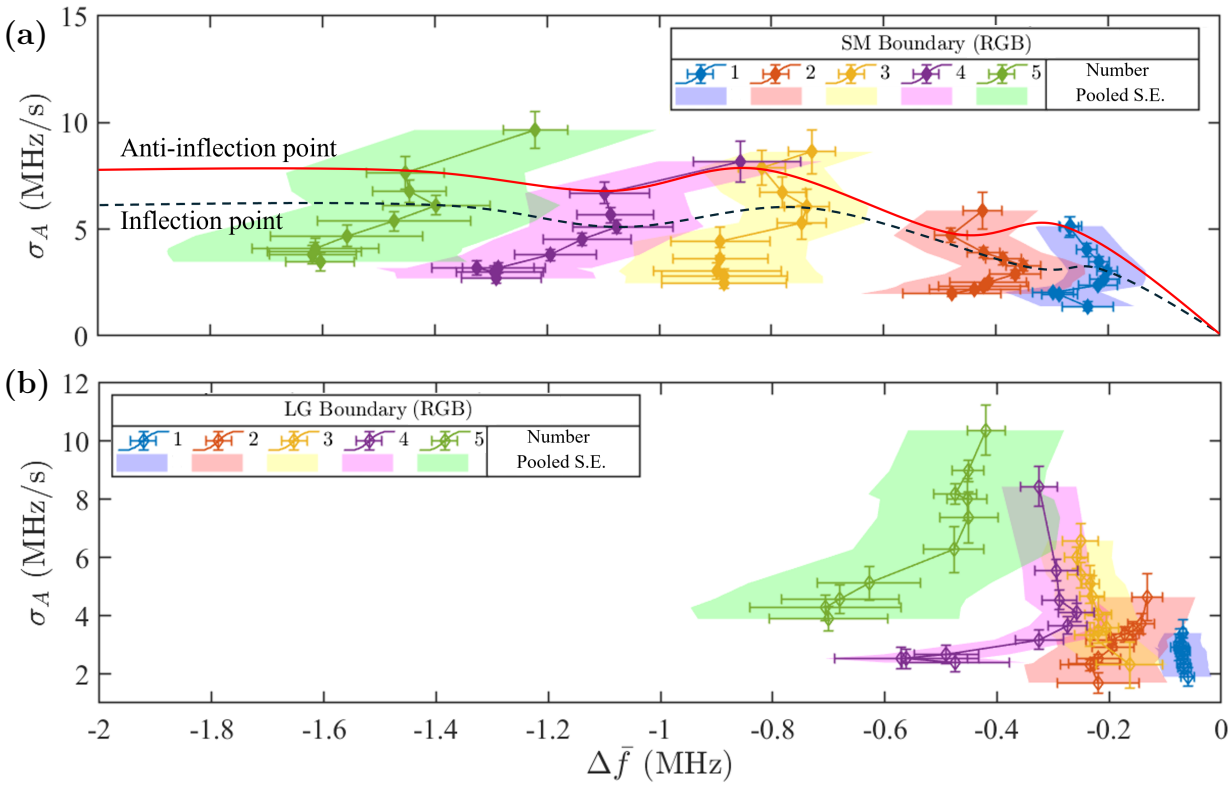


Figure 4.17: σ_A *vs.* $\Delta\bar{f}$ **plot for** $M = 1, 2, 3, 3, 5$ **RGBs.** σ_A *vs.*$\Delta\bar{f}$ relationship colour-coded for multiple RGBs using different boundaries with shaded $\Delta\bar{f}$ pooled standard errors (a) SM boundary case: inflection point represented by dotted black dotted line at $T_{inf} = 30$ minutes ($T_{inf} = 60$ minutes $M = 1 and 2$. Anti-inflection point represented by a red solid line through $T_{inf'} = 5$ minutes. (b) LG boundary case: Absent consistent inflection and anti-inflection point.

Inferred previously, there is an anti-inflection point that occurs at $T_{inf'} = 5$ minutes for all measurements, and a regular inflection point at $T_{inf} = 60$ minutes for 1-to-2 RGBs using the SM boundary. For 3-5 RGBs, the inflection point occurs at $T_{inf} = 30$ minutes Figure 4.17(a). These two inflection points were discussed previously and derive a characteristic relationship different from that of the RFB. This suggests that at longer time intervals outside of the Active Region, when insect activity is decreasing, $\Delta\bar{f}$ is greatly influenced by spontaneous movement for 1-to-5 RGBs. As expected, for the LG boundary case, increasing T_{int} shows an absence of any inflection or anti-inflection points, even with an increasing number of RGBs Figure 4.17(b). Additionally, the characteristic curves for 2 and 3 RGBs, and to a lesser extent 3 and 4 RGBs, intercept, increasing the challenge of distinguishing insect numbers.

The low sensitivity and intersecting characteristic curves produce a greater challenge in differentiating RGB numbers for the LG boundary case compared to the SM boundary case.

The frequency shift response as a function of RGB number varies with the length of the time interval chosen. WLS linear regression fits are performed for both the frequency shift sensitivity and insect activity sensitivity of both boundaries for all time intervals. The reported errors belong to the S.E. from fitted coefficients. Looking at the first time interval $T_{int} = 1$ minute, the frequency shift sensitivity is fit using $\Delta\bar{f}(M) = S_{\Delta\bar{f}}M$ with a 95% confidence interval. Figure 4.18(a) represents the SM boundary case results of $S_{\Delta\bar{f}} = (-0.237 \pm 0.008)$ MHz, which is more sensitive than $S_{\Delta\bar{f}} = (-0.077 \pm 0.004)$ MHz observed for the LG boundary case in Figure 4.18(b). Within the approximate linear regime for insect activity of $M \in [1, 5]$ RGBs, the insect activity is fit by $\sigma_A(M) = S_{\sigma_A}M + \sigma_o$ with 95% confidence intervals. In Figure 4.18(c) $S_{\sigma_A} = (1.14 \pm 0.15)$ MHz/s and $\sigma_o = (4.0 \pm 0.4)$ MHz/s for the SM boundary case. Whereas Figure 4.18(d), representing the LG boundary, had $S_{\sigma_A} = (1.74 \pm 0.08)$ MHz/s and $\sigma_o = (1.5 \pm 0.2)$ MHz/s. We see that there is a negative correlation between the frequency shift sensitivity and RGB number, contrary to the positive correlation with the insect activity and RGB number as was found for the RFB case.

Similar to the RFB, the linear fits are produced for longer time intervals with their S.E., demonstrating that $\Delta\bar{f}$ and σ_A are time dependent. There is a frequency shift insensitivity $S_{\Delta\bar{f}}$ with longer time intervals when using the LG bounded sensor in Figure 4.12(a). Although, we retain $T_{inf'} = 5$ minutes and $T_{inf} = 60$ minutes of the much greater frequency shift sensitivity using the SM bounded sensor. From Appendix A, the linear regression coefficient R^2 is generally higher than 0.9 for both bounded sensors indicating a good fit for all time intervals. Where the fitted $S_{\Delta\bar{f}}$ was found to be statistically significant for all time intervals as well. Now, for the fitted insect activity, there is a visual power-law like trend of the insect activity sensitivity $S_{\sigma A}$ in Figure 4.12(b) where there appears to be slight enhancement in $S_{\sigma A}$ using the LG bounded sensor for $T_{int} < 30$ minutes, but at longer time intervals S_{σ_A} appears inconsequential to boundary choice. Lastly, the intercept σ_o is much greater for the

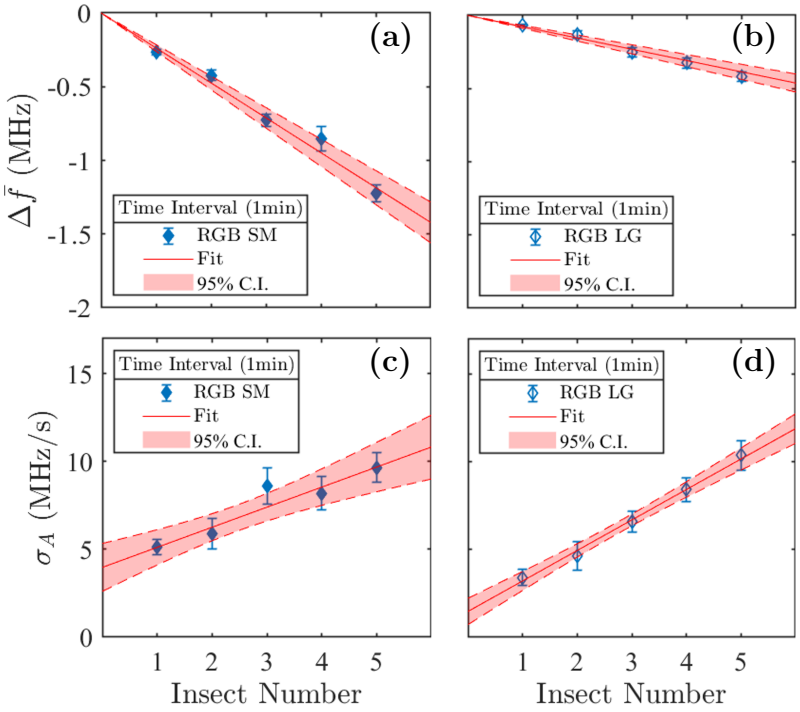


Figure 4.18: $\Delta\bar{f}$ and σ_A *vs.* M RGB at $T_{int} = 1$ minute. Weighted least-squares linear regression solid red line fit of frequency shift $\Delta\bar{f} = S_{\Delta\bar{f}}M$ and insect activity $\sigma_A = S_{\sigma_A}M + \sigma_o$ with 95% confidence interval shaded red region for $T_{int} = 1$ minute (a) $\Delta\bar{f}$ SM boundary case (b) $\Delta\bar{f}$ LG boundary case. (c) σ_A SM boundary case. (d) σ_A LG boundary case.

SM boundary Figure 4.12(c). Referring to Appendix A, at $T_{inf'} = 5$ minutes there is a poor fit indicated by $R^2_{SM} = 0.6959$ and statistically insignificant S_{σ_A} with $p = 0.08$ indicating a different model or more statistical analysis be required. It was seen for most time intervals the $R^2 > 0.9$ and $p - values$ of fitted insect activity coefficients are all statistically significant using the SM bounded sensor, possibly due to a low overall insect activity when compared to the RFB. However, when using the LG bounded sensor, $R^2_{LG} \to 0.5$ with increasing time interval and beyond $T_{int} = 15$ minutes the fitted insect activity coefficients have $p - values$ all statistically insignificant ($p > 0.05$). Suggesting that the LG bounded sensor using the linear fitting procedure works poorly for RGB number and a new model or further samples be used to strengthen the relationship.

The SM boundary RGB case exemplifies increased sensitivity to insect activity and frequency response, specifically showing a signal much larger than the baseline σ_A and $\Delta\bar{f}$

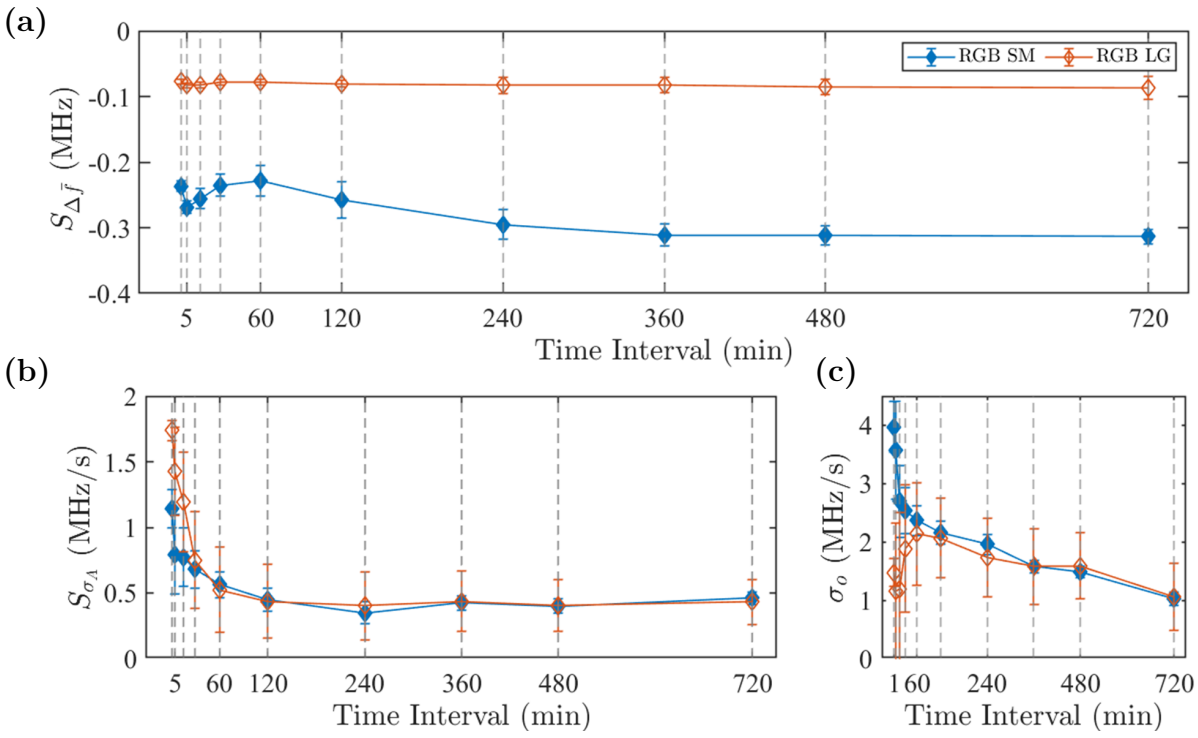


Figure 4.19: $S_{\Delta\bar{f}}$, $S_{\sigma A}$, **and** σ_o, **vs.** T_{int} **for RGB** Linear fitting parameters of Figure 4.10 with S.E. as a function of T_{int} for both boundaries. (a) $S_{\Delta\bar{f}}$, (b) $S_{\sigma A}$, and (c) σ_o.

in Figure 4.6. However, the LG boundary case appears to exhibit an insensitive frequency response to RGB insect activity, indicating low sensitivity to the analyte in short time intervals and a possible frequency drift masking effect over long time intervals, as seen in the baseline $\Delta\bar{f}$ measurements in Figure 4.6.

To conclude this section, similar to the RFB, the single RGB insect when induced to move from placing the insect into the sensor, observes an activity-duration relationship that follows a power-law within the Active Region and becomes constant in the Spontaneous Region. However, unlike the RFB case, the LG bounded sensor observes two constant Activity Regions that do not coincide with the selected $T < 60$ minutes Active Regions from previous. There is however, a Spontaneous Region for $T > 270$ minutes. 1-to-5 RGB insects resulted in an initial activity parameter taken at $T = 1$ minutes that was larger for the SM boundary case compared to the LG boundary case and the sensitivity and intercept had no

significant advantage with the choice of boundary used. Similar to the RFB case, the Active Region initial activity is much more responsive to the movement of additional insects in the Spontaneous Region. Additionally, observed for the SM bounded configuration, the influence of multiple insects affected the movement of the RGB individually, producing a collective endurance that increased with RGB number. The σ_A vs. $\Delta\bar{f}$ characteristic curve modeling the RGB behavior signal for increasing longer time intervals unveiled two inflection points: anti-inflection point at $T_{inf'} = 5$ minutes and regular inflection point at $T_{inf} = 60$ minutes. These inflection points were observed only using the SM bounded case for a single RGB as well as for multiple RGB. The LG bounded case did not contain much more information other than an increase in insect activity and frequency response with added RGB number.

4.5 Comparison between RFB and RGB

Differentiating between insect species is incredibly important for effective pest management, as treatment methods may only be effective for specific insects. Additionally, applying a treatment method, such as a fumigant, may require a specific concentration to ensure proper eradication of the pest. Failure to accurately treat the level of infestation of a particular insect species can result in costly mistakes for the user, such as increased dockage fees and the need for reapplication of the fumigant. Moreover, this can have serious consequences for the consumer, including increased exposure to mycotoxins, the growth of more resilient pests, and the consumption of fumigant residue. Therefore, it is essential for a sensor to be capable of distinguishing between species, counting the number of captured insects, and determining the level of infestation. These are crucial criteria for a post-harvest insect pest sensor.

To begin the comparison between two common post-harvest insect pests, RFB and RGB, the relative sensitivity towards insect activity and frequency shift response for a single insect will be analyzed to determine how the signals differ. Additionally, the impact of boundary choice on the signal for each species will be examined. By considering criteria based on

movement, dielectric size, and shape, both insect activity and frequency response sensitivities will be used to demonstrate how 1-to-5 RGBs can be differentiated from 1-to-5 RFBs as their capture time increases.

4.5.1 Relative Sensitivity for a Single RGB and RFB

In the previous sections, it was observed that σ_A and $\Delta\bar{f}$ per time interval were weaker for RGBs in both boundary scenarios. By utilizing the relative sensitivity and by maintaining the same boundaries for signal comparison between RFBs and RGBs, the insect activity relative difference, $R_{In}^{\sigma_A} = (\sigma_{RFB} - \sigma_{RGB})/\sigma_{RGB} \times 100\%$, was initially larger for $T_{int} < 15$ minutes when comparing the LG boundary to the SM boundary, as shown in Figure 4.20(a). $R_{In,LG}^{\sigma_A}$ decreases more rapidly than $R_{In,SM}^{\sigma_A}$ with increasing time intervals, with the curves intersecting at $T_{int} = 15$ minutes ($R_{In}^{\sigma_A} \sim 150\%$). Beyond this point, $R_{In,SM}^{\sigma_A} > R_{In,LG}^{\sigma_A}$ at longer time scales. The frequency shift response relative difference, $R_{In}^{\Delta\bar{f}} = (\Delta\bar{f}_{RFB} - \Delta\bar{f}_{RGB})/\Delta\bar{f}_{RGB} \times 100\%$, is significantly stronger using the LG boundary compared to the SM boundary, as shown in Figure 4.20(b). Notably, the RFB-to-RGB signal difference is approximately 830% when using the LG boundary, compared to approximately 250% when using the SM boundary at $T_{int} = 1$ minute, and $R_{In,SM}^{\Delta\bar{f}} > R_{In,LG}^{\Delta\bar{f}}$ for all measured T_{int}. The SM boundary produces consistent $R_{In}^{\sigma_A}$ measurements, while a greater differentiation $R_{In}^{\Delta\bar{f}}$ between smaller and larger insects is more suitable for using the LG boundary.

The signals from different insects of the same species can vary depending on the boundary used to enclose the sensing environment. In general, a larger detection area with weak electric-field concentrations of the sensing environment results in a poor quality signal, which is the case with the LG boundary configuration, as shown in Figure 4.20. Here, the relative insect activity difference, $R_{Bd}^{\sigma_A} = (\sigma_{SM} - \sigma_{LG})/\sigma_{LG} \times 100\%$, is enhanced for both RGBs and RFBs when comparing SM-to-LG boundary signals of the individual species. Initially, $R_{Bd,RGB}^{\sigma_A} > R_{Bd,RFB}^{\sigma_A}$ for $T_{int} < 15$ minutes, but $R_{Bd,RGB}^{\sigma_A}$ decreases rapidly again, intersecting $R_{Bd,RGB}^{\sigma_A} = R_{Bd,RFB}^{\sigma_A} \propto 40\%$ at $T_{int} = 15$ minutes and performing worse at very long time

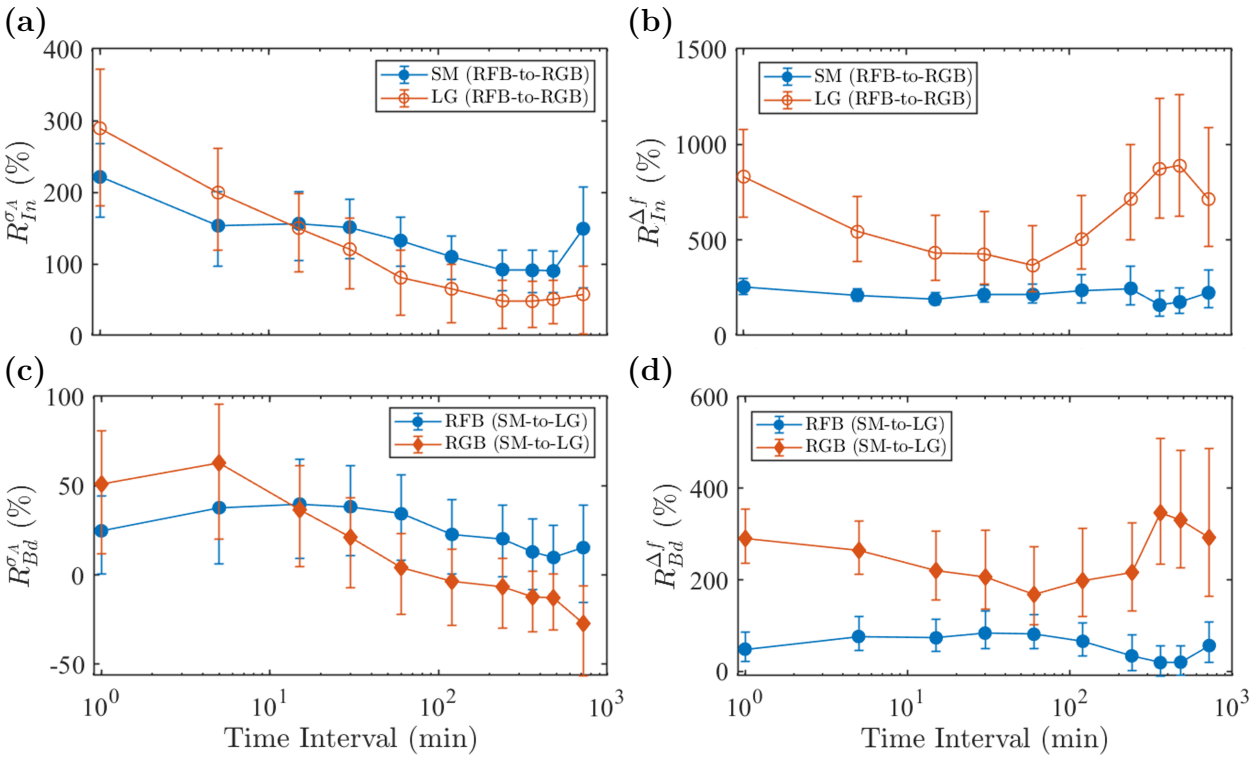


Figure 4.20: Relative Sensitivity Single RGB and RFB Measurements. Single RFB and RGB 10 sample measurements comparison based on relative sensitivity. (a) Relative insect activity sensitivity with insect species comparison for same boundaries. (b) Relative frequency response sensitivity with insect species comparison for same boundaries. (c) Relative insect activity sensitivity with for individual insect using different boundaries. (d) Relative frequency response sensitivity with for individual insect using different boundaries.

intervals, as shown in Figure 4.20(c). Conversely, $R^{\sigma_A}_{Bd,RFB} \sim (40 \pm 10)\%$ remains roughly constant for all time intervals. In general, the relative frequency shift response difference $R^{\Delta\bar{f}}_{Bd} = (\Delta\bar{f}_{SM} - \Delta\bar{f}_{LG})/\Delta\bar{f}_{LG} \times 100\%$ is enhanced for both species, and $R^{\Delta\bar{f}}_{Bd,RGB} > R^{\Delta\bar{f}}_{Bd,RFB}$ for all time intervals. Figure 4.20(d).

Using two differently sized boundaries generally enhances the signal of individual species when using the sensor with the SM boundary, which confines the insects to specific strong electric-field regions. In this case, the smaller RGB's insect activity and frequency shift response are greatly enhanced when using the SM boundary, while the signal enhancement for the larger RFB is less significant. However, when comparing two species of using the same sized boundary, the signal differentiation is less significant but evolves more slowly over time

for the SM boundary configuration. Conversely, the LG boundary sensor can greatly enhance frequency shift response differentiation between small and large insects (RGB and RFB), but with diminishing differentiation of the insect activity signal. In the previous section, RFB and RGB exhibited two different characteristic curves using the SM boundary for 1-to-5 insects, identifying two critical inflection points at specific time intervals. Here, the differing signal levels based on insect activity and frequency response are demonstrated. Next, using $S_{\Delta\bar{f}}$, S_{σ_A}, and σ_0 determined through fitting, we will demonstrate how 1-to-5 insects can be differentiated between RFB and RGB species.

4.5.2 Sensitivity Comparison between 1-to-5 RFBs and RGBs

As demonstrated in the previous section, the insect activity and frequency shift response evolved by increasing the time interval to acquire data. Here, the sensitivities for the SM and LG boundaries will be used to compare 1 RFB to 1-to-5 RGBs and then 1-to-5 RFBs to 1-to-5 RGBs over T_{int} using the frequency shift sensitivity $S_{\Delta\bar{f}}$, insect activity sensitivity S_{σ_A}, and insect activity level σ_o previously determined.

The insect activity sensitivity S_{σ_A} is a secondary but necessary parameter when a non-stationary analyte is used for microwave sensing. Together with the primary parameter, the frequency shift response sensitivity $S_{\Delta\bar{f}}$, both are time-dependent, adding another layer of complexity. However, they become particularly useful when the analyte has characteristic features. In this context, for the RFB and the RGB, we first analyze the insect activity sensitivity using different boundaries.

A comparison between 1 RFB and up to 5 RGBs using both the predictor (fitted) equations $\sigma_A(M) = S_{\sigma_A}M + \sigma_o$ and $|\Delta\bar{f}(M)| = |S_{\Delta\bar{f}}M|$[3] is made to create a simple model. A bar plot that compares the magnitude from the predictor equations for the corresponding insect number is grouped by time intervals with conservative 95% confidence interval error bars determined by the S.E. Figure 4.21. Subjectively, the least interesting results are using the

[3]Here the absolute value used for easier representation of the bar plots.

LG bounded configuration in Figure 4.21(a). The $|\Delta\bar{f}(M)|$ differentiation between 1 RFB and 1-to-5 RGBs is clear such that $|\Delta\bar{f}_{RFB}(1)| > |\Delta\bar{f}_{RGB}(1 \rightarrow 5)|$ for all T_{int}. This coincides with the previous reasoning that the frequency shift response differentiation of species using the LG boundary is significantly enhanced in Figure 4.20(d). The $\sigma_A(M)$ differentiation using the LG boundary in Figure 4.21(b) demonstrates $\sigma_{A,RFB}(1) > \sigma_{A,RGB}(1 \rightarrow 4)$ at $T_{int} = 1$ minute, but the difference quickly diminishes and for multiple RGBs and single RFB becomes indistinguishable for all RGB numbers beyond $T_{int} \geq 15$ minutes.

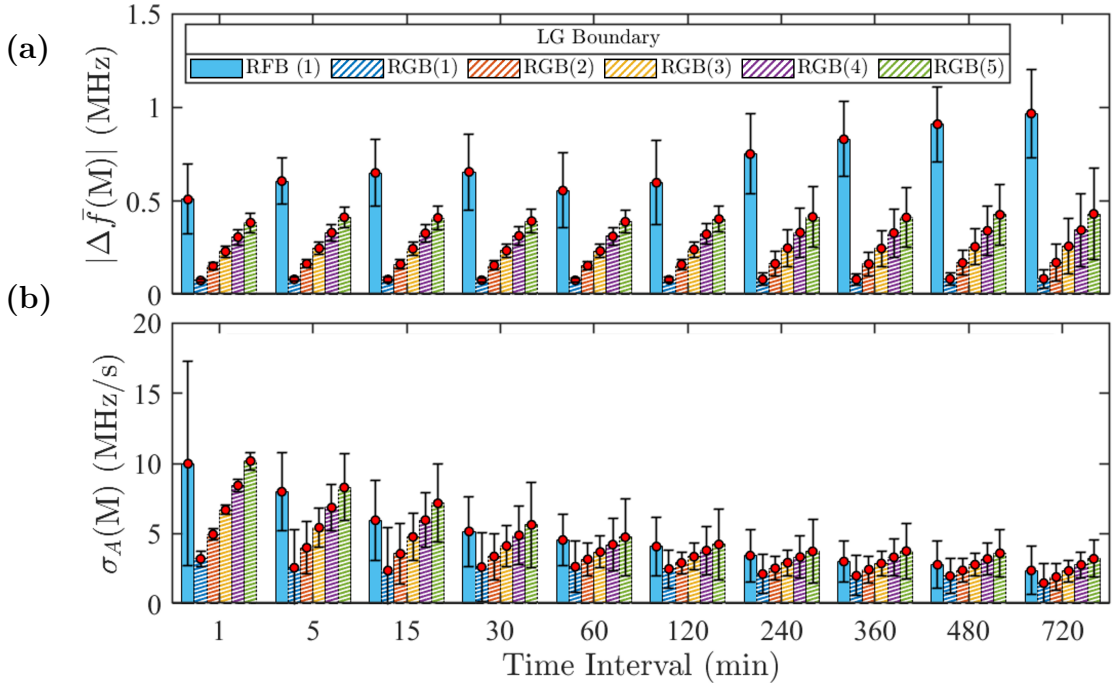


Figure 4.21: LG Boundary:1 RFB vs. 1-to-5 RGB $|\Delta\bar{f}(M)|$ and $\sigma_A(M)$ Bar Plot Comparison Bar plot comparison using LG bounded configuration for 1 RFB to 1-to-5 RGB. RFB has solid bar colouring and RGB has hatched coloured bar coloring. The error bars are the 95% C.I. using the S.E from Figure 4.12 and Figure 4.19. (a) $|\Delta\bar{f}(M)|$ comparison. (b) $\sigma_A(M)$ comparison.

Figure 4.22 demonstrates the advantage of choosing the SM bounded microwave sensor. Here, it is first worth mentioning the much greater enhancement of the $|\Delta\bar{f}(M)|$ RGB signal for all M Figure 4.22(a). Although, $|\Delta\bar{f}_{RFB}(1)| \sim |\Delta\bar{f}_{RFB}(3)|$ for $T_{int} \geq 15$ minutes, before this time interval 1 and 3 RFB are discernible. Apart from what scenario was just mentioned,

1-to-5 RGB are $|\Delta\bar{f}|$ distinguishable with 1 RFB. The SM bounded sensor demonstrates a greater insect activity enhancement for all time intervals, thus for up to a time interval of $T_{int} = 240$ minutes, we see that $\sigma_{A,RFB}(1) > \sigma_{A,RGB}(1 \rightarrow 5)$. This means that although we observe a similar frequency response between 1 RFB and 3 RGB for a time interval greater than or equal to 15 minutes, the insect activity response can be used a secondary distinguishing parameter.

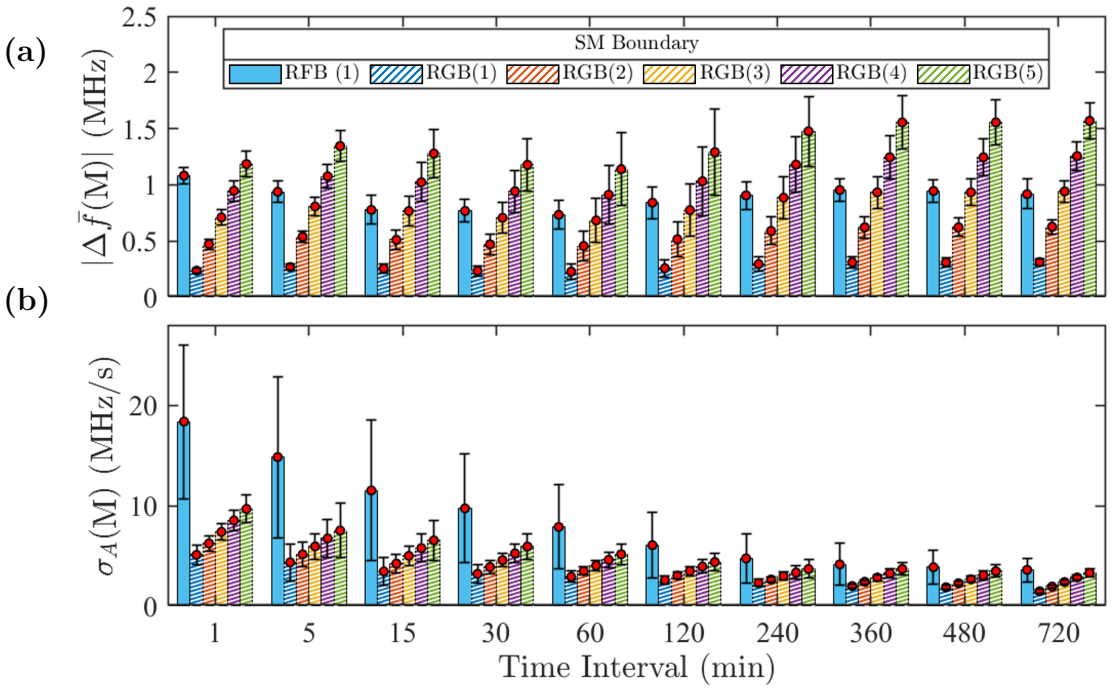


Figure 4.22: SM Boundary:1 RFB vs. 1-to-5 RGB $|\Delta\bar{f}(M)|$ and $\sigma_A(M)$ Bar Plot Comparison Bar Plot comparison using SM bounded configuration for 1 RFB to 1-to-5 RGB. RFB has solid bar colouring and RGB has hatched coloured bar coloring. The error bars are the 95% C.I. using the S.E from Figure 4.12 and Figure 4.19. (a) $|\Delta\bar{f}(M)|$ comparison. (b) $\sigma_A(M)$ comparison.

To examine how well this basic model is at distinguishing RFB and RGB insects, we expand this comparison to 1-to-5 RFBs and RGBs. An example in Figure 4.23 (a) of how this comparison is performed is using the SM boundary bar plot $|\Delta\bar{f}(M)|$ predictor results for 1 RFB and 3 RGBs at $T_{int} = 1$ minute. To ascertain by how much our predictors (x_{In}) are distinguishable between any number of species that we are comparing, we examine

the amount of overlapping error δx_{In} relative to the predicted difference Δx_{In}. Figure 4.23(a) demonstrates our predictors $|\Delta\bar{f}_{RFB}(1)|$ and $|\Delta\bar{f}_{RGB}(3)|$ and errors, which we use a conservative 95% C.I., $\delta|\Delta\bar{f}_{RFB}(1)|$ and $\delta|\Delta\bar{f}_{RGB}(3)|$ to find that the total error $\sum\delta|\Delta\bar{f}|$ is smaller than the predicted difference $\Delta|\Delta\bar{f}|$ indicating a non-overlapping error region.

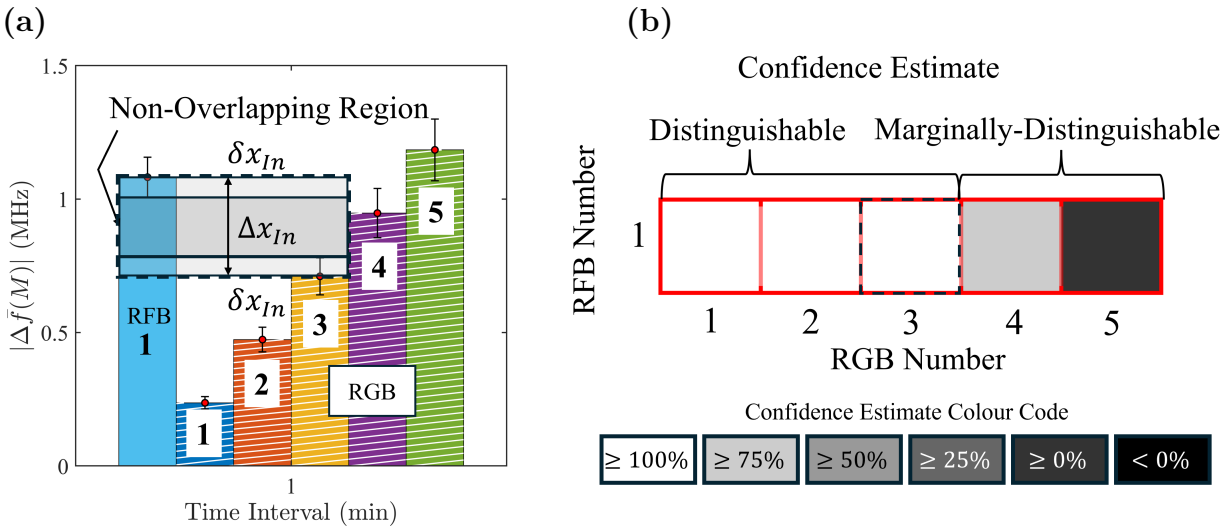


Figure 4.23: SM Boundary $|\Delta\bar{f}(M)|$ Confidence Estimate Comparing 1 RFB with 5 RGB Example (a) Constructing C.E. using $|\Delta\bar{f}(M)|$ of 1 RFB and 5 RGB at $T_{int} = 1$ minute bar plot comparing overlapping space of one-sided 95% C.I. (δx_{In}) light gray shaded regions to shaded gray measured difference Δx_{In} region between 1 RFB to 3 RGB example (1 RFB and 3 RGB has a non-overlapping region). (b) Colour coded distinguishability comparing overlapping region of 1 RFB to 5 RGBs with$C.E. \geq 100, \geq 75, \geq 50, \geq 25, \geq 0, and < 0\%$. Black indicating indistinguishability for a $C.E. < 0\%$ not shown here.

Using the 95% C.I. as an estimate of how well the RFB model is differentiable from the RGB model a confidence estimate is constructed:

$$C.E. = (1 - (\sum \delta x_{In} - |\Delta x_{In}|)/|\Delta x_{In}|) \cdot 100\% \tag{4.5}$$

where C.E. is normalized to 100% percent or threshold from non-overlapping C.I. region to partially overlapping C.I. region. Using a gray scale colour code in Figure 4.23(b) a $C.E \geq 100\%$ is coloured white means that the to predictors are completely distinguishable

seen when comparing $|\Delta\bar{f}|$ predictor for 1 RFB and 1,2, and 3 RGBs, whereas $C.E. \geq 75\%$ $\geq 50\% \geq 25\%$, and $\geq 0\%$ are colour coded from light-to-dark gray with decreasing percentage indicates a marginally-distinguishable C.E. which was observed for 1 RFB compared with 4 and 4 RGBs. A $C.E. < 0\%$ is colour coded in black indicating the the two predictors are indistinguishable from each other and no comparison can be drawn. Here, we have set our C.E. using a 95% C.I of both predictors we can manipulate our level of certainty that the predicted values are indeed distinguishable by controlling the C.I. percentage such as a higher(lower) C.I. would increase(decrease) the C.I. interval size which would decrease(increase) distinguishability.

5 by 5 matrices with gray scale elements representing a $C.E.\%$ are constructed by comparing 1-to-5 RFBs and 1-to-5 RGBs for the fitted prediction equations $|\Delta\bar{f}(M)|$ and $\sigma_A(M)$. Each matrix represents a specific time interval in which the predictor comparisons are performed. Examining the LG boundary first, the $\sigma_A(M)$ predictor indicates that beyond $T_{int} \geq 15$ minutes 1 RFB and 2-to-5 RGB are indistinguishable and even 1 RGB with 1 RFB is marginally-distinguishable for short time intervals Figure 4.24(a). Greater than 1 RFB however, exhibits distinguishable C.E.s with most RGB numbers, but for 4-5 RGBs at longer time intervals does distinguishability become worse when compared to large numbers of RFB. In Figure 4.24(b), using the $|\Delta\bar{f}(M)|$ predictor, demonstrates that in general RFB and RGB have $C.E.$s with distinguishabilities greater than or equal to 100% for most T_{int} that enable 1-to-5 RFB and 1-to-5 RGB to be differentiated with certainty. The 4-to-5 RGB $|\Delta\bar{f}(M)|$ comparison with 1 RFB has some marginal distinguishability at the onset time interval and some 30 to 240 minutes. Indicating that by using the LG boundary prediction model, there is greater differentiation between species and insect number using the $|\Delta\bar{f}(M)|$ predictor, but is almost unusable for the $\sigma_A(M)$ model apart from a 1-to-1 RGB and RFB comparison at short time intervals.

Previously, we have seen that the SM boundary model enhances the smaller RGB signal, which can pose a challenge using the $|\Delta\bar{f}(M)|$ predictor and that the secondary

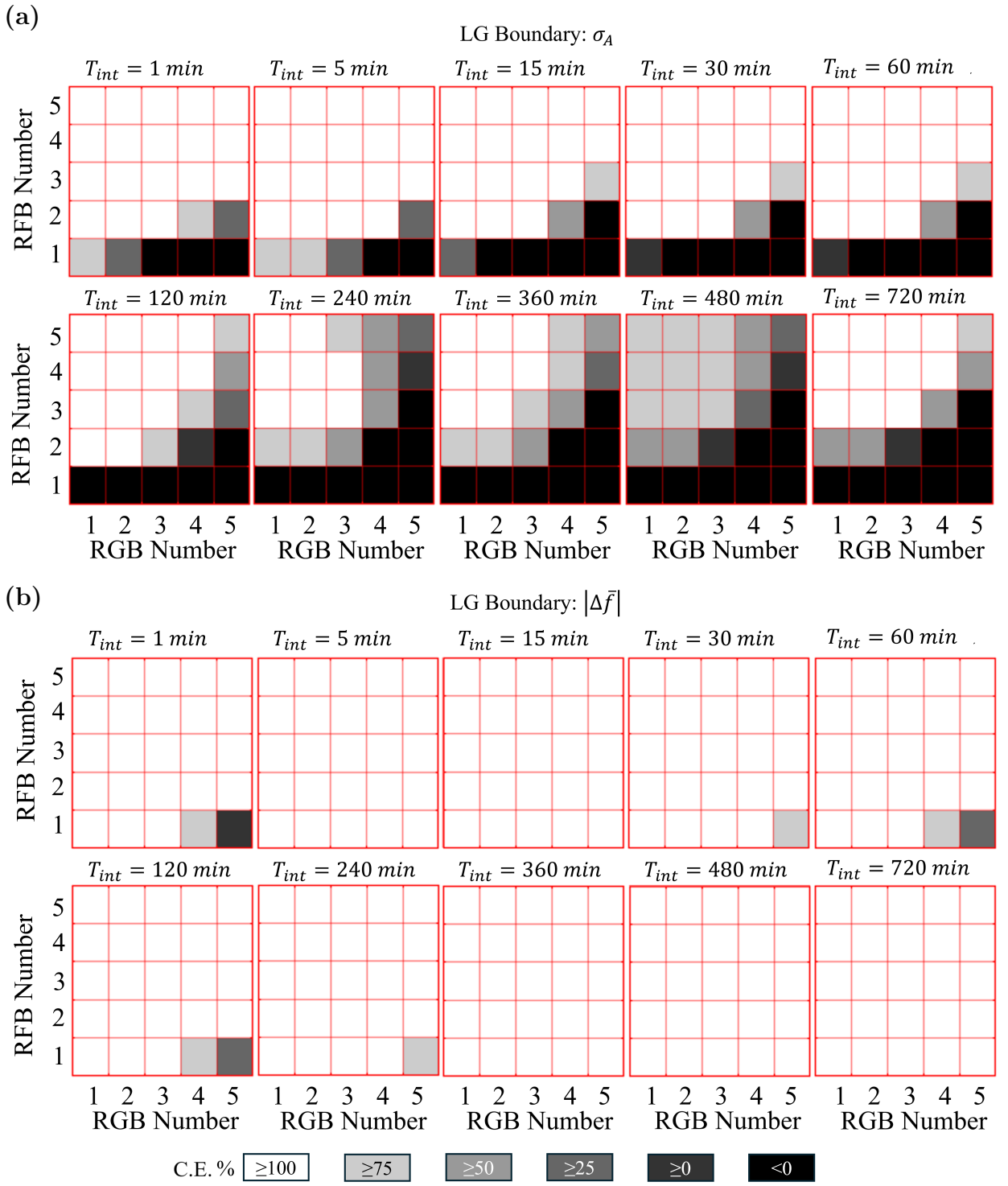


Figure 4.24: LG Boundary C.E. Matrices for 1-to-5 RFB and RGB Comparisons. Confidence Estimate matrices for RFB vs. RGB using LG boundary, showing distinguishability levels by predictor across time intervals. Color-coded percentages: $C.E. \geq 100$, ≥ 75, ≥ 50, ≥ 25, ≥ 0, and $< 0\%$, with high values indicating distinguishability and low/negative values indicating indistinguishability. (a) Insect activity comparison. (b) Frequency response comparison.

predictor $\sigma_A(M)$ should be used to aid differentiation of species and number. It can be seen in Figure 4.25(a), that using the predictor $\sigma_A(M)$, apart from $T_{int} = 1$ minute, there is marginal-distinguishability between 1 RFB and 1-to-5 RGB below $T_{int} \geq 60$ minutes, and 1-to-3 RGB for all time intervals. There are $C.E. \geq 50\%$ for $T_{int} \geq 5$ minutes, and complete distinguishability ($C.E. \geq 100\%$) using the $\sigma_A(M)$ predictor between 2-to-5 RFB and 1-to-5 RGB. Using the $|\Delta\bar{f}(M)|$ predictor in Figure 4.25(b), 2 RFB and 1-to-5 RGB have a $C.E. \geq 100\%$ for all time intervals with some marginal-distinguishability between 2 RFB and 5 RGB ($T_{int} >= 15$ minutes). Apart from 1 RFB compared with 3 RGB for $T_{int} \geq 15$ minutes (4 RGB for $T_{int} \geq [60\ 120]$ minutes), $C.E. \geq 100\%$ for most RGB number comparison to 1 RFB for the other time intervals. By sacrificing $|\Delta\bar{f}(M)|$ differentiability using the SM boundary, we gain an enhancement in $\sigma_A(M)$ predictor as a secondary parameter to compare species and insect number.

For a granular summary of the 1-to-1 RFB and RGB comparison to determine the effectiveness of the SM and LG bounded sensors, we say that the choice of boundary size on the sensor affects the insect signal strength. This signal depends on the size of insect and its detectable movement within the boundary relying on the insect-electric-field interaction. A general frequency shift and insect activity enhancement is observed when using the SM bounded sensor for both insects, but the RGB frequency shift response is much more enhanced than the RFB response. This indicates the SM bounded electric-field confinement of the sensor is more receptive towards RGB movement than it did previously with the weaker electric-field confinement using the LG bounded sensor. As such, the LG bounded sensor is more receptive towards the larger size of the RFB due to a size-position overlap increase with the strong electric-field regions resulting in an enhanced frequency shift. The insect activity SM bounded configuration enhancement benefit the RGB experiences initial sees at short time intervals decreases rapidly as the time interval is expanded when compared to the near-constant enhancement the RFB experiences when using the SM bounded sensor. Indicating the short time interval benefit when performing the insect activity comparison

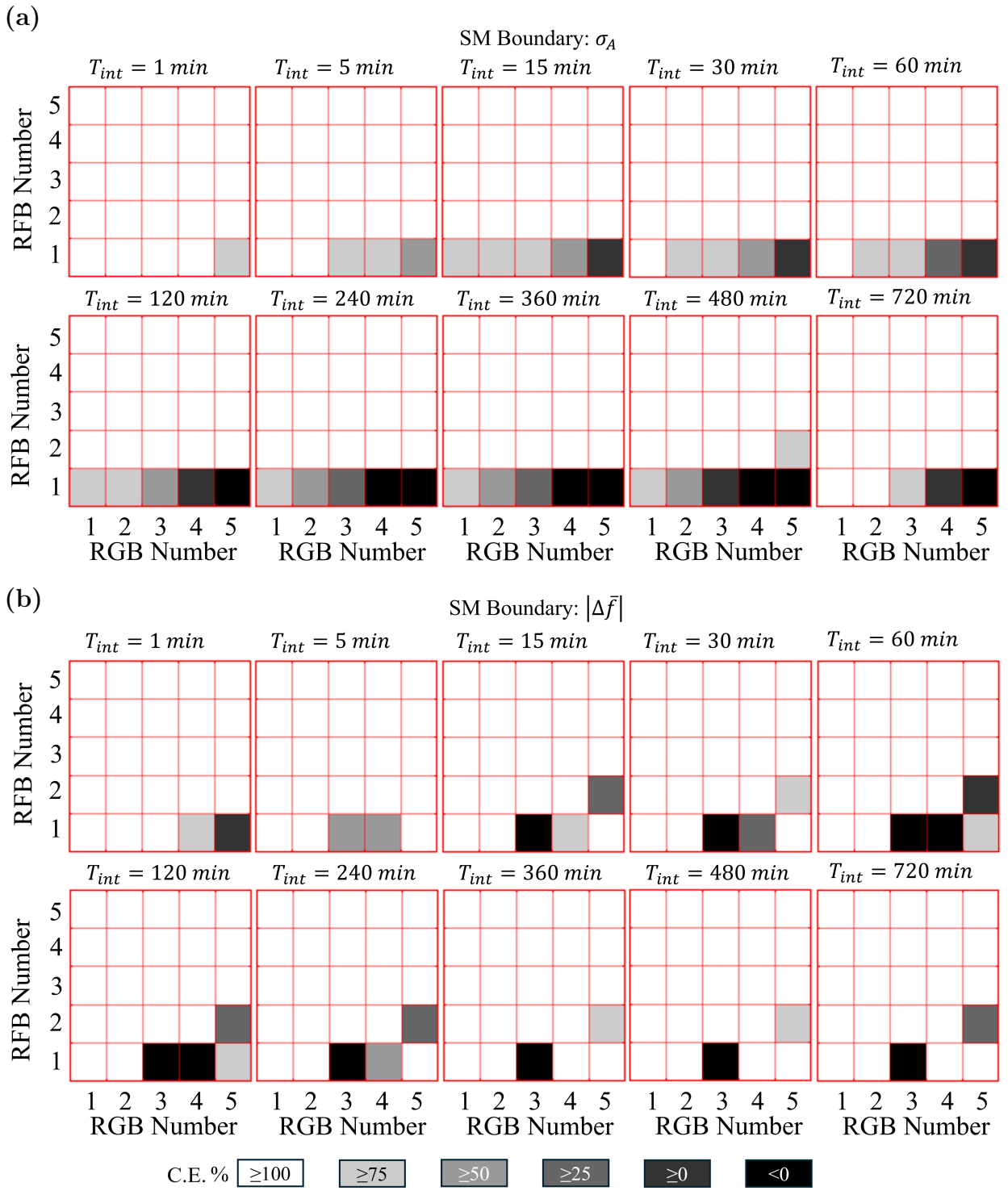


Figure 4.25: SM Boundary C.E. Matrices for 1-to-5 RFB and RGB Comparisons. Confidence Estimate matrices for RFB vs. RGB using SM boundary, showing distinguishability levels by predictor across time intervals. Color-coded percentages: $C.E. \geq 100$, ≥ 75, ≥ 50, ≥ 25, ≥ 0, and $< 0\%$, with high values indicating distinguishability and low/negative values indicating indistinguishability. (a) Insect activity comparison. (b) Frequency response comparison.

of species using both boundary types. We see that due to the confinement of the strong electric-fields of the SM bounded sensor the signals are overall enhanced and the weak electric-field regions demonstrate a potential special insect size filtering application.

A broad conclusion on the comparisons between RFB and RGB LG and SM bounded sensor models can be summarized as follows. The LG bounded $|\Delta\bar{f}(M)|$ good distinguishability for all RFB and RGB combinations and that the model performs better when distinguishing larger RFB insects to smaller RGB insects. Whereas the SM bounded $\sigma_A(M)$ can distinguish 1 RFB with 1-to-5 RGBs that gets progressively worse at longer time intervals but 2 RFBs are distinguishable for nearly all combinations of RGBs indicating that the model excels and makes use of the insect activity metric as a secondary comparison parameter. Such that the SM bounded $|\Delta\bar{f}(M)|$ and $\sigma_A(M)$ models excel when used as a combined metric when one model fails to distinguish between a certain combination of insect number and species (1 RFB with 3 RGBs for $T_{int} \geq 15$ minutes), which the inadequate LG bounded $\sigma_A(M)$ model is unable to perform for nearly all T_{int} comparisons with 1 RFB and multiple RGBs even with larger RFB numbers at longer time intervals. Hence, the weak electric-field regions of the LG bounded sensor struggle with accurately detecting movement that negatively affect insect activity and even affect the frequency shift response more so for the smaller insect in this RFB and RGB comparative experiment. Overall, the key interaction occurs between 1 RFB and 1-to-5 RGBs. And the optimal time interval to perform these comparisons occurs for $T_{int} = 1 - 5$ minutes when insects are most active due to stimulation, which indicates the timeliness of this procedure. However, these optimal time intervals can be larger or smaller depending on the smaller or larger size of confidence intervals used, respectively.

4.6 Conclusion

The entirety of Chapter 4 was quite extensive, with the multidimensional experiments taken (boundary size, insect activity, frequency shift, and insect species and number), requires

reiteration. The important findings are highlighted.

Activity-Duration Power Law: When stimulated by removing the insect forcefully from their habitat, the RGB and RFB insects exhibited an energetically unsustainable time-dependent insect activity that followed a decaying power-law trend within the high-movement dominated Active Region. Within that time region, the initial activity was positively correlated with insect number and endurance of the system increased. This was observable for both LG and SM boundaries for the RFB, but only the SM bounded sensor detected this for the RGB. Outside of the Active Region where the insect is no longer stimulated, the energetically sustainable Spontaneous region had an insect activity that was constant for the remainder of the experiment. Here, the spontaneous insect activity exhibited positive correlation with insect number for both insects and both boundaries. The initial insect activity level is greatly enhanced using the SM bounded sensor within the Active Region, but the initial insect activity sensitivity has no choice of boundary preference for the RFB. The spontaneous insect activity level had no preferential choice of boundary nor insect species, but was had enhanced sensitivity towards the larger RFB insect. But in all cases, all fitted coefficients were much larger for the power-law fitted data when compared to the spontaneous activity fitted data.

Characteristic σ_A *vs.* $\Delta\bar{f}$ RFB and RGB Curves: The frequency shift and insect activity response recorded for increasing time intervals from point of detection produced time dependent responses. The SM bounded sensor produced repetitive characteristics seen for 1-to-5 RGB and RFB insects, which was not observed for the LG bounded sensor. The insect activity decreased visually via power-law with increasing time intervals, whereas the frequency shift magnitude is initially decreasing at shorter time intervals before increasing in magnitude again after a special time interval has elapsed. This special inflection interval T_{inf} produces an inflection point that was observed for both RGB and RFB curves of multiple insects suggesting a transition from an active-to-spontaneous dominated movement where the frequency shift magnitude increases due to

the insect being more likely to rest on strong electric-field field regions on the sensor for prolonged periods of time. However an anti-inflection point $T_{inf'}$ was only observed in the RGB curves where the initial frequency shift magnitude increases before decreasing again to T_{inf} suggesting the the RGB insects are moving into the strong electric-field regions of the IDC electrodes. Linear fits were applied to both the frequency shift and insect activity response of both boundaries. RFB frequency shift sensitivity retained the inflection point at $T_{int} = 60$ minutes using the SM boundary and had greater sensitivity than the LG boundary. Similarly, the RGB frequency shift response retained both $T_{inf'} = 5$ minutes and $T_{inf} = 60$ minutes of the SM boundary and was more sensitive than LG boundary which exhibited insensitivity with increasing time intervals. The insect activity activity sensitivity made no preference of boundary choice for RFB, but was slightly more sensitive for $T_{int} < 30$ minutes using the LG boundary when observing RGB sensitivity. The initial insect activity was enhanced using the SM boundary, but made no difference at longer time intervals for both RFB and RGBs.

Comparison: The choice of boundary size significantly influences the sensor's ability to differentiate insect signals based on frequency shift and insect activity metrics. Using the LG boundary, frequency shift differentiation between the smaller RGB and larger RFB is enhanced. However, the LG boundary struggles to distinguish insect activity signals, particularly for 1 RFB compared to 1-to-5 RGBs across all time intervals, with is challenged further for 2 RFBs at longer intervals. In contrast, the SM boundary provides enhanced frequency shift responses, particularly for the smaller RGB, and demonstrates good versatility in comparing species and insect numbers. While the SM boundary model has limitations, such as distinguishing 1 RFB from 3 RGBs at $T_{int} \geq 15$ minutes using frequency shift alone, the insect activity metric compensates by remaining distinguishable to marginally distinguishable at these time intervals. Notably, the SM boundary $|\Delta\bar{f}(M)|$ model is still functional when comparing 1 RFB to multiple RGBs for most time intervals and excels when increasing to 2-to-5 RFBs

for all time intervals In general, both boundaries exhibit strengths and limitations: the LG boundary relies primarily on frequency shift but struggles with insect activity differentiation, while the SM boundary effectively combines frequency shift and activity metrics for better overall performance. The optimal time for insect number and species comparison of both boundary types occurs at $T_{int} = 1 - 5$ minutes, when the insects are most active. Overall, the SM boundary demonstrates greater versatility and reliability in distinguishing species and insect numbers.

In closing, here we have demonstrated the importance of utilizing insect activity in conjunction with the typical dielectric frequency shift response. We have demonstrated the crucial time interval dependence of these measurements that were used to construct a simple prediction model to distinguish between 1-to-5 RFBs and 1-to-5 RGBs, with the proper modifications such as mechanism to induce insect movement (heater or mechanical/electric vibrator) for a field application, the model can be tested, built upon, and validated to assist in assessing the number of insects and types of insects for proper treatment procedures.

5

Outlook

The portable insect detection system presented in this thesis has demonstrated the capability to detect the presence of insects in a field application and the methods to assist in differentiating the number of insects and these two species. The ability to monitor activity-duration relationships as a power law is a novel experimental finding. However, whether the system as a whole can be effectively applied depends on the context and to whom it is applicable.

We present anecdotal market research as part of a Lab2Market entrepreneurial outreach program, which demonstrated a duality with insect pest monitoring of stored grains. One key question is the cost comparison between the detection system and the cost associated with dockage and treatment. Of 54 interviews, in four different industry sectors (grain supply, research, ag technology, and IPM), 50% were Canadian, 35% American, and roughly 15% were from Germany, Greece, Israel, and India. These interviews indicated a need for an insect detection system, although important factors to consider include environmental climate, cost, agricultural advancement, and type of commodity stored. Of which a subset of farmers and pest control companies could see the most benefit of such a system.

A portable insect detection system could be beneficial to farmers or grain handlers who store their products for long periods of time. This is often the case for farmers seeking better market prices. A related issue with storage times is climate. In Canada, cold weather is beneficial for long-term storage, but in places with warmer and more humid climates, such

as the southern U.S., the Mediterranean climates of Israel and Greece, and the subtropical-tropical climates of India, there is a higher risk of insect infestations. The key issue here is the level of agricultural advancement. If grain farming and storage infrastructure is advanced and has systems in place to facilitate monitoring, there may be less need for an insect detection system. For example, temperature and moisture monitoring cables are already on the market to monitor grain bin conditions, and carbon dioxide monitors are used to track mold and insect growth. Proper bin cleaning procedures, aeration, and conditioning guidelines also help manage grain moisture and temperature. However, countries that lack grain handling standards and agricultural infrastructure and have warm and humid climates, such as parts of Africa and India, could benefit from a low-cost insect detection system.

The economic consideration of investing in such a system depends on the commodity being stored. Durable grains such as wheat, barley, and rice have low global market prices, so the cost of a preventive system must be weighed against acceptable post-harvest losses. High-value products such as nuts or non-durable fruits carry a higher monetary risk from insect infestations and, therefore, would see a better return on investment than low-cost grains.

As grain is bought and sold along the supply chain, the costs of chemical treatments increase, from farmer to grain elevator, from elevator to grain terminal, and then to international shipment. Domestic and international food processing plants must meet government standards and avoid monetary loss due to plant shutdowns, product rejection, or damage to company reputation. Thus, the financial risk associated with insect infestations increases as more money is spent from field to table. Many companies implement Integrated Pest Management (IPM) strategies, either in-house or through third-party pest control companies. Whether in storage silos, warehouses, or both indoor and outdoor areas of processing facilities, IPM strategies are designed to reduce insect infestations before chemical treatments become necessary.

Interviews with four food processing facilities and nine pest control companies identified

key desired features in an insect detection system: early warning detection, assistance with insect number thresholds, and species identification. The system must determine whether there is a problem, what insect is causing it, and how many insects are present to help correct the decision-making process by IPM strategists. This would (1) reduce the monetary loss that a company might face and (2) reduce the environmental impact of chemical treatments. Additional desirable features include deployment in difficult-to-reach places (such as inside grain silos) and the ability to provide electronic health reports. If such a system can meet these criteria in a cost-effective package, a portable insect detection system could be useful. This is the goal of our prototype, which demonstrates threshold detection, counting, and species identification using a basic model.

5.0.1 Cost-Benefit Analysis Example

To assess the financial gain or loss of one of the aforementioned target users for a portable insect detection system, we can perform a cost-benefit analysis. Since insider pest-control information on food processing is challenging to obtain and farmers living in developing countries may be hard to get accurate information on, we use a small grain farm where the farmer holds on to his\her harvest for long periods of time in hopes to get a better market price.

An average grain farm size in North America is around 39k bushels and a common grain storage silo size is 40k bushels. This 1-to-1 ratio is not ideal, but for the sake of this analysis it is sufficient. In 2024, the market high in Canada was around $7.6 per bushel in CDN dollars. Assume now that the silo has an insect infestation such that 2% of the grain is lost (typically low average value in Canada). Using a low-cost fumigant 6.5¢per bushel to fumigate his entire bin would result in a profit loss of $8.5k in materials alone (neglecting labour). Now, if the farmer uses our portable insect detection system, we could provide an early warning notification that his/her grain silo was infested such that they were able to reduce the loss by 50%, reduce the need for fumigation, and implement cost-effective treatment methods

(unknown cost). A rough material cost estimate of the total sensor package (neglecting laptop) using 5 sensors typically placed at the cardinal points in the silo is around $670 CDN. Using the proposed deliverables would save the farmer $4.9k at a minimum in material costs alone. For the farmer to break-even and realistically still apply the fumigant to treat his/her grain, the loss reduction grain silo would need see to see is 11.3% at minimum. A realistic scenario is that the farmer diversifies his storage using 4 10k bushels grain silos where each silo has a sensor package. With only one silo infested experiencing a 2% loss and fumigant applied, the farmer would need a loss reduction of approximately 63.9% over a 2 year period at minimum. This is a significant improvement required by the portable insect detection system.

We see that the margins for the farmer to turn a profit are narrow. In the realistic case, the percentage demands for the loss reduction are high on the untested portable detection system, so that it may not be in the best interest of the farmer to adopt such a system even in the idealistic scenario that the farmer gets the best market price. However, if the farmer experiences losses on a much larger scale such as 20% in developing countries or has significantly more stored product, it could be beneficial for the farmer. This is also true for food processing plants, where the cost of their product will be much higher than the cost of unprocessed grains and will be more exposed to risk than the average farmer. To make a proper judgment of whether the cost outweighs the benefit or vice versa, the portable detection system needs to be tested in the field.

5.0.2 Future Work

The work done in Chapter 3 identified the construct and functionality of an insect detection system. Future improvements to advance the portable insect detection system for real-world applications require more technical considerations.

Power Management and Mulptle Sensors: Currently, the battery lifetime of the system is limited, requiring a connection to a power grid for long operating times. Field operations where access to power is not guaranteed become a challenge. Lithium ion

batteries with greater capacity (mili-Amp-hours) is an option (15.6 days at 12000 mAh), but increases the size of the system. Another option would be operating in a pulsed-power mode, where an IC chip can power cycle the on-off state of the LNA, hence conserving power. In a theoretical 5 minutes on and 55 minutes off power cycle using a 1000 mAh battery, the operation lifetime is extended to 21.6 days. However, cycling power in microwave oscillators affects the stability of the oscillation frequency, particularly at the onset "warm-up" state. However, the discontinuous signal generated when an insect is captured needs to be investigated further to determine how insect activity and frequency shift response differ in this mode. More importantly, for a real grain silo application, to extend the likelihood of detecting insects in infested grain, more sensors need to be employed. A problem with multiple sensors is the signal processing method only capable of recording a single peak. This problem can be mitigated by operating the group of sensors in an intermittent pulsed-power mode only recording the peak frequency of one of the sensors for a short amount of time before shutdown and recording the peak of another sensor. These factors should be considered for the further development of a field-capable insect detection system.

Data Transmission and Analysis: This problem is two-fold. First, if the system were to be used in a "metal" grain silo, the reflection and absorption properties of conductive metal would hinder any RF signal sent to the receiver system. That means that either the placement of the receiver would be in a cumbersome position inside of the silo or modifications would be needed of the silo structure. Second, is the data analysis; indeed, many people have host PCs and running GNU Radio would not be an issue, however, it is inconvenient especially when a PC is unavailable to be used for this task. The HackRF can be used in conjunction with on-the-market microcontrollers who can run the GNU Radio framework, and further DSP tasks in GNU Radio are feasible such as the threshold analysis, but would be significantly hindered due to the MCUs processing speed. The current method requires a large amount of memory and

a fast CPU to perform continuous FFT tasks, which for a poor spec'd system would cause a buffering overflow leading to data loss. Regardless, to access the MCU data, Bluetooth technology can be integrated with Cloud technology to get real-time updates on a personnel smart phone which is common practice today.

Sensor Robustness: Effects such as temperature, humidity/moisture, debris build-up,physical compressive stress, and even corrosion from fumigants will negatively impact the performance of the microwave sensor. The microwave probe sensor is a preliminary setup, but a robust system that can compensate for those performance-degrading effects need to be implemented in a field design. So far, we have examined how the sensor performs in ideal ambient air, grain temperature, and moisture conditions, but the system's performance in different environments needs to be considered. For example, the sensor housing's structural components can be reinforced to withstand the inward pressure it will experience in a grain environment, a mask need be applied to the copper components to prevent corrosion, or a reactive heater circuit could be added for cold or varying climates to help stabilize the oscillation frequency of the microwave sensor and local oscillator of the SDR. A comparative analysis between the current system and a more portable version should be performed to determine if there is any data degradation in different environmental scenarios.

Chapter 4 demonstrated how insect activity can be used in conjunction with the insect frequency shift to distinguish between 1-to-5 RFB and RGB insects using different boundary sizes. Such a complex technique and lengthy analysis method possibly require the implementation of artificial intelligence to simplify and speed up processing times. Neglecting A.I. for now, the steps to advance this technique are as follows:

1. Determine characteristic σ_A *vs.* $\Delta\bar{f}$ curves for more common post-harvest insect species, particularly those similar in size to RFB and RGB.

2. Analyze the time dependency of the frequency shift and insect activity at points during

and after first detection. Other insect activity-stimulating methods, such as using a heater circuit or mechanical/electric vibrator can be explored. This could enable a new analytical method using the pulsed-power operation of the sensor.

3. Observe these phenomena under different environmental and phenotypical conditions, such as varying temperatures and humidity levels, since insect activity is directly related to these factors. For different sizes of an insect during its life cycle, the breadth of the sensor's response will vary.

4. For in-grain purposes, account for the grain factor, as insect movement within grain differs from their movement outside grain bins.

If the system can first improve species identification and counting techniques, the hardware specifications can then be refined through field trials to fully demonstrate the capability of a microwave sensor as a portable insect detection system. Then, creating a catalogue of various insects signals for specific sensor configurations under certain conditions can use A.I. technology to create a comparative analysis of field data vs. studied data in the pursuit to be truely useful for society.

Appendices

A

Time-Interval Dependent Sensitivity

Tables are constructed based on the $\Delta\bar{f}(M) = S_{\Delta\bar{f}}M$ and $\sigma_A(M) = S_{\sigma_A}M + \sigma_o$ fits for RFB and RGB insects with number $M \in [1, 5]$ using both SM and LG boundaries. The fitted coefficients with S.E., $p - values$, and R^2 model fit are in columns with increasing time interval T_{int}. Table A.1 and Table A.2 refer to the SM and LG boundary measurements taken for RFB, respectively. Table A.3 and Table A.4 refer the the SM and LG boundary measurements taken for the RGB, respectively. Within both boundaries for both insects the $\Delta\bar{f}(M)$ fits are statistically significant based on the p-value for all time intervals. However, for $\sigma_A(M)$, the p-values for S_{σ_A} are generally statistically significant except for longer than 15 minute time intervals for the LG boundary RGB case. Likewise, most intercepts σ_o are statistically weak except for the SM boundary RGB case. Thus, more investigations towards insect activity are needed.

Time Interval (min)	*Insect Activity* $\sigma_A(M)$					*Frequency Shift* $\Delta\bar{f}(M)$		
	$S_{\sigma_A} \pm S.E.$ (MHz/s)	$p-value$	$\sigma_o \pm S.E.$ (MHz/s)	$p-value$	R^2	$S_{\Delta\bar{f}} \pm S.E.$ (MHz)	$p-value$	R^2
1	4.5±0.9	0.018	14±3	0.02	0.8824	-1.08±0.03	<0.01	0.9919
5	3.8±1.0	0.03	11±3	0.05	0.8338	-0.94±0.03	<0.01	0.9830
15	3.0±0.9	0.04	9±3	0.06	0.7943	-0.78±0.05	<0.01	0.9562
30	2.4±0.7	0.04	7±2	0.05	0.7968	-0.77±0.04	<0.01	0.9741
60	2.1±0.6	0.03	5.8±1.8	0.05	0.8192	-0.73±0.05	<0.01	0.9582
120	1.9±0.5	0.03	4.2±1.4	0.06	0.8509	-0.84±0.05	<0.01	0.9548
240	1.6±0.5	0.02	3.1±1.1	0.06	0.8680	-0.91±0.04	<0.01	0.9544
360	1.5±0.3	0.018	2.7±0.9	0.06	0.8818	-0.95±0.04	<0.01	0.9577
480	1.4±0.3	0.011	2.5±0.7	0.04	0.9119	-0.95±0.04	<0.01	0.9698
720	1.2±0.3	0.02	2.5±0.6	0.02	0.8751	-0.94±0.05	<0.01	0.9412

Table A.1: Time interval dependent insect activity and frequency shift RFB response using SM boundary

Time Interval (min)	*Insect Activity* $\sigma_A(M)$					*Frequency Shift* $\Delta\bar{f}(M)$		
	$S_{\sigma_A} \pm S.E.$ (MHz/s)	$p-value$	$\sigma_o \pm S.E.$ (MHz/s)	$p-value$	R^2	$S_{\Delta\bar{f}} \pm S.E.$ (MHz)	$p-value$	R^2
1	4.0±1.0	0.03	6±3	0.15	0.8447	-0.51±0.07	<0.01	0.7885
5	3.1±0.4	<0.01	4.9±1.2	0.03	0.9580	-0.91±0.04	<0.01	0.9464
15	2.6±0.5	0.014	3.4±1.3	0.09	0.9010	-0.65±0.06	<0.01	0.9195
30	2.3±0.5	0.016	2.9±1.2	0.10	0.8910	-0.66±0.07	<0.01	0.9019
60	1.8±0.4	0.014	2.7±0.9	0.06	0.9000	-0.56±0.07	<0.01	0.8825
120	1.2±0.4	0.05	2.8±1.0	0.07	0.7735	-0.60±0.08	<0.01	0.8636
240	0.9±0.4	0.09	2.6±0.9	0.07	0.6749	-0.75±0.08	<0.01	0.8995
360	1.3±0.4	0.04	1.8±0.8	0.10	0.7882	-0.83±0.07	<0.01	0.9141
480	1.1±0.4	0.07	1.7±0.8	0.14	0.7247	-0.91±0.07	<0.01	0.9116
720	1.1±0.3	0.03	1.3±0.7	0.17	0.8484	-0.97±0.08	<0.01	0.9010

Table A.2: Time interval dependent insect activity and frequency shift RFB response using LG boundary

Time Interval (min)	*Insect Activity* $\sigma_A(M)$					*Frequency Shift* $\Delta\bar{f}(M)$		
	$S_{\sigma_A} \pm S.E.$ (MHz/s)	$p-value$	$\sigma_o \pm S.E.$ (MHz/s)	$p-value$	R^2	$S_{\Delta\bar{f}} \pm S.E.$ (MHz)	$p-value$	R^2
1	1.14±0.15	<0.01	4.0±0.4	<0.01	0.9526	-0.237±0.008	<0.01	0.9826
5	0.8±0.3	0.08	3.6±0.8	0.02	0.6959	-0.269±0.010	<0.01	0.9834
15	0.8±0.2	0.04	2.7±0.6	0.02	0.8046	-0.256±0.015	<0.01	0.9576
30	0.68±0.02	0.016	2.5±0.4	<0.01	0.8873	-0.236±0.017	<0.01	0.9399
60	0.56±0.10	0.011	2.4±0.3	<0.01	0.9104	-0.23±0.02	<0.01	0.8869
120	0.45±0.02	0.014	2.16±0.19	<0.01	0.8898	-0.26±0.03	<0.01	0.8972
240	0.35±0.08	0.02	1.96±0.17	<0.01	0.8562	-0.30±0.02	<0.01	0.9453
360	0.43±0.06	<0.01	1.60±0.11	<0.01	0.9507	-0.311±0.017	<0.01	0.9690
480	0.40±0.05	<0.01	1.49±0.10	<0.01	0.9467	-0.311±0.015	<0.01	0.9776
720	0.46±0.05	<0.01	1.03±0.12	<0.01	0.9709	-0.314±0.011	<0.01	0.9828

Table A.3: Time interval dependent insect activity and frequency shift RGB response using SM boundary

Time Interval (min)	*Insect Activity* $\sigma_A(M)$					*Frequency Shift* $\Delta\bar{f}(M)$		
	$S_{\sigma_A} \pm S.E.$ (MHz/s)	$p-value$	$\sigma_o \pm S.E.$ (MHz/s)	$p-value$	R^2	$S_{\Delta\bar{f}} \pm S.E.$ (MHz)	$p-value$	R^2
1	1.74±0.08	<0.01	1.5±0.2	<0.01	0.9943	-0.077±0.003	<0.01	0.9775
5	1.4±0.3	0.02	1.2±1.2	0.4	0.8576	-0.083±0.004	<0.01	0.9780
15	1.2±0.4	0.05	1.2±1.3	0.4	0.7670	-0.082±0.004	<0.01	0.9634
30	0.8±0.4	0.14	1.9±1.1	0.18	0.5791	-0.079±0.004	<0.01	0.9451
60	0.5±0.3	0.2	2.1±0.9	0.09	0.4656	-0.078±0.004	<0.01	0.9491
120	0.4±0.3	0.2	2.1±0.7	0.07	0.4427	-0.081±0.005	<0.01	0.9537
240	0.4±0.3	0.2	1.7±0.7	0.08	0.4476	-0.083±0.012	<0.01	0.8151
360	0.4±0.3	0.16	1.6±0.6	0.09	0.5431	-0.083±0.012	<0.01	0.8086
480	0.4±0.2	0.13	1.6±0.6	0.07	0.5814	-0.086±0.012	<0.01	0.8318
720	0.43±0.17	0.08	1.1±0.6	0.16	0.6830	-0.086±0.017	<0.01	0.7545

Table A.4: Time interval dependent insect activity and frequency shift RGB response using LG boundary

Bibliography

[1] Rural Infrastructure and Agro-Industries Division. Fao/world bank workshop on reducing post-harvest losses in grain supply chains in africa. Technical report, FAO, 2010. 1

[2] Linda J Mason and Marissa McDonough. Biology, behavior, and ecology of stored grain and legume insects. *Stored product protection*, 1(7):7–20, 2012. 1

[3] Christos G Athanassiou and Frank H Arthur. *Recent advances in stored product protection*. Springer, 2018. 1

[4] MD Toews, FH Arthur, and JF Campbell. Monitoring tribolium castaneum (herbst) in pilot-scale warehouses treated with β-cyfluthrin: are residual insecticides and trapping compatible? *Bulletin of entomological research*, 99(2):121–129, 2009. 1

[5] CH Bell. Fumigation in the 21st century. *Crop protection*, 19(8-10):563–569, 2000. 1

[6] Manoj K Nayak, Gregory J Daglish, and Thomas W Phillips. Managing resistance to chemical treatments in stored products pests. *Stewart Postharvest Rev*, 11(1):1–6, 2015. 1

[7] NDG White, RT Arbogast, PG Fields, RC Hillmann, SR Loschiavo, Bh Subramanyam, James E Throne, and VF Wright. The development and use of pitfall and probe traps for capturing insects in stored grain. *Journal of the Kansas Entomological Society*, pages 506–525, 1990. 1

[8] LB Smith. Efficiency of berlese-tullgren funnels for removal of the rusty grain beetle, cryptolestes ferrugineus, from wheat samples1. *The Canadian Entomologist*, 109(4):503–509, 1977. 1

[9] David W Hagstrum. Seasonal variation of stored wheat environment and insect populations. *Environmental Entomology*, 16(1):77–83, 1987. 1

[10] Jun-Hwan Park and Hoi-Seon Lee. Phototactic behavior 10: phototactic behavioral effects of plodia interpunctella (hübner)(lepidoptera: Pyralidae) adults to different light-emitting diodes of seven wavelengths. *Journal of Applied Biological Chemistry*, 59(2):95–98, 2016. 1

[11] KW Vick, RW Mankin, RR Cogburn, M Mullen, JE Throne, VF Wright, and LD Cline. Review of pheromone-baited sticky traps for detection of stored-product insects. *Journal of the Kansas Entomological Society*, pages 526–532, 1990. 1

[12] Rekha Kaushik and Jyoti Singhai. Sensing technologies used for monitoring and detecting insect infestation in stored grain. *Int. J. Eng. Tech*, 7:169–173, 2018. 2

[13] David W Hagstrum, Thomas W Phillips, and Gerrit Cuperus. Stored product protection. *Kansas State University, Manhattan, KS. KSRE Publ*, 2012. 2

[14] DE Maier, LH Channaiah, A Martinez-Kawas, J Lawrence, E Chaves, P Coradi, and G Fromme. Monitoring carbon dioxide concentration for early detection of spoilage in stored grain. jul. *Kühn-Arch*, 425:505–509, 2010. 2

[15] J Wu, DS Jayas, Qiang Zhang, NDG White, and RK York. Feasibility of the application of electronic nose technology to detect insect infestation in wheat. *Canadian Biosystem Engineering Journal*, 55, 2013. 2

[16] Richard W Mankin, David W Hagstrum, Mark T Smith, AL Roda, and Moses TK Kairo. Perspective and promise: a century of insect acoustic detection and monitoring. *American Entomologist*, 57(1):30–44, 2011. 2

[17] Matheus Cardim Ferreira Lima, Maria Elisa Damascena de Almeida Leandro, Constantino Valero, Luis Carlos Pereira Coronel, and Clara Oliva Gonçalves Bazzo. Automatic detection and monitoring of insect pests—a review. *Agriculture*, 10(5):161, 2020. 2

[18] C Karunakaran, DS Jayas, and NDG White. Soft x–ray inspection of wheat kernels infested by sitophilus oryzae. *Transactions of the ASAE*, 46(3):739, 2003. 2

[19] Sang Sook Kim, Mee-Ra Rhyu, Jae Min Kim, and Sang-Hyo Lee. Authentication of rice using near-infrared reflectance spectroscopy. *Cereal chemistry*, 80(3):346–349, 2003. 2

[20] D Shuman, JA Coffelt, and DK Weaver. A computer-based electronic fall-through probe insect counter for monitoring infestation in stored products. *Transactions of the ASAE*, 39(5):1773–1780, 1996. 2

[21] Dennis Shuman, David K Weaver, and Ronald G Larson. Performance of an analytical, dual infrared-beam, stored-product insect monitoring system. *Journal of economic entomology*, 98(5):1723–1732, 2005. 3

[22] PW Flinn, GP Opit, and JE Throne. Predicting stored grain insect population densities using an electronic probe trap. *Journal of economic entomology*, 102(4):1696–1704, 2009. 3

[23] Insects Limited Inc. Sight trap. https://foresightipm.com/, 2018. Accessed: 30 August 2024. 3

[24] Dalia M Elsheakh, Mohamed I Ahmed, Gomaa M Elashry, Saad M Moghannem, Hala A Elsadek, Waleed N Elmazny, Nelly H Alieldin, and Esmat A Abdallah. Rapid detection

of coronavirus (covid-19) using microwave immunosensor cavity resonator. *Sensors*, 21(21):7021, 2021. 3, 4

[25] RW Mankin. Microwave radar detection of stored-product insects. *Journal of economic entomology*, 97(3):1168–1173, 2004. 3

[26] Alex Reimer, Kelsey Wiebe, Jinwei Rao, Bimu Yao, Yongsheng Gui, Fuji Jian, Paul Fields, Digvir S Jayas, and Can-Ming Hu. A compact microwave device for monitoring insect activity in grain samples. *Biosystems Engineering*, 175:27–35, 2018. 4, 5, 6

[27] Rammah Ali Alahnomi, Zahriladha Zakaria, Zulkalnain Mohd Yussof, Ayman Abdulhadi Althuwayb, Ammar Alhegazi, Hussein Alsariera, and Norhanani Abd Rahman. Review of recent microwave planar resonator-based sensors: Techniques of complex permittivity extraction, applications, open challenges and future research directions. *Sensors*, 21(7):2267, 2021. 4

[28] Ningyi Wang, Nan Zhang, Tianshuang Wang, Fangmeng Liu, Xiaolong Wang, Xu Yan, Chenguang Wang, Xiaomin Liu, Peng Sun, and Geyu Lu. Microwave gas sensor for detection of ammonia at room-temperature. *Sensors and Actuators B: Chemical*, 350:130854, 2022. 4

[29] Mohammad H Zarifi, Pooya Shariaty, Zaher Hashisho, and Mojgan Daneshmand. A non-contact microwave sensor for monitoring the interaction of zeolite 13x with co2 and ch4 in gaseous streams. *Sensors and Actuators B: Chemical*, 238:1240–1247, 2017. 4

[30] Jian Liu and Guomin Li. A remote sensor for detecting methane based on palladium-decorated single walled carbon nanotubes. *Sensors*, 13(7):8814–8826, 2013. 4

[31] Jin-Kwan Park, Tae-Gyu Kang, Byung-Hyun Kim, Hee-Jo Lee, Hyang Hee Choi, and Jong-Gwan Yook. Real-time humidity sensor based on microwave resonator coupled with pedot: Pss conducting polymer film. *Scientific reports*, 8(1):439, 2018. 4

[32] Luqman Ali, Cong Wang, Fan-Yi Meng, Kishor Kumar Adhikari, Yu-Chen Wei, Ji-Hu Li, Zi-Wei Song, and Meng Zhao. Design and optimization of interdigitated microwave sensor for multidimensional sensitive characterization of solid materials. *IEEE Sensors Journal*, 21(20):22814–22822, 2021. 5, 13

[33] Keat Ghee Ong and Craig A Grimes. A resonant printed-circuit sensor for remote query monitoring of environmental parameters. *Smart materials and structures*, 9(4):421, 2000. 5

[34] Joseph Mitola. Software radios: Survey, critical evaluation and future directions. *IEEE Aerospace and Electronic Systems Magazine*, 8(4):25–36, 1993. 5

[35] José Raúl Machado-Fernández. Software defined radio: Basic principles and applications. *Revista Facultad de Ingeniería*, 24(38):79–96, 2015. 5

[36] Changzhi Li, Zhengyu Peng, Tien-Yu Huang, Tenglong Fan, Fu-Kang Wang, Tzyy-Sheng Horng, Jose-Maria Munoz-Ferreras, Roberto Gomez-Garcia, Lixin Ran, and Jenshan Lin. A review on recent progress of portable short-range noncontact microwave radar systems. *IEEE Transactions on Microwave Theory and Techniques*, 65(5):1692–1706, 2017. 5

[37] AS Sedra, KC Smith, T Chan Carusone, and V Gaudet. *Microelectronic Circuits, international 6th edition*. New York: Oxford University Press, 2011. 5, 22, 23

[38] Thomas A Milligan. *Modern antenna design*. John Wiley & Sons, 2005. 5

[39] David P Rees. *Insects of stored products*. CSIRO publishing, 2004. 6, 80

[40] Canadian Grain Comission. Identify an insect. https://grainscanada.gc.ca/en/grain-quality/manage/identify-an-insect/, 2024. Accessed: 31 August 2024. 6

[41] Thangarasu Anukiruthika, Fuji Jian, and Digvir S Jayas. Movement and behavioral response of stored product insects under stored grain environments-a review. *Journal of Stored Products Research*, 90:101752, 2021. 6

[42] Fuji Jian. Influences of stored product insect movements on integrated pest management decisions. *Insects*, 10(4):100, 2019. 6

[43] Fuji Jian, Ron Larson, Digvir S Jayas, and Noel DG White. Three dimensional temporal and spatial distribution of adults of tribolium castaneum (coleoptera: Tenebrionidae) in stored wheat under different temperatures and adult densities. *Agricultural Research*, 1:165–174, 2012. 6

[44] CH Bell. A review of insect responses to variations encountered in the managed storage environment. *Journal of stored products research*, 59:260–274, 2014. 6

[45] Marek Konarzewski and Aneta Ksiażek. Determinants of intra-specific variation in basal metabolic rate. *Journal of Comparative Physiology B*, 183:27–41, 2013. 6

[46] Craig R White and Michael R Kearney. Determinants of inter-specific variation in basal metabolic rate. *Journal of Comparative physiology B*, 183:1–26, 2013. 6

[47] Archibald Vivian Hill. The physiological basis of athletic records. *The Scientific Monthly*, 21(4):409–428, 1925. 6

[48] Mark Burnley. Invited review: The speed-duration relationship across the animal kingdom. *Comparative Biochemistry and Physiology Part A: Molecular & Integrative Physiology*, 279:111387, 2023. 6

[49] Jonah P Drake, Axel Finke, and Richard A Ferguson. Modelling human endurance: Power laws vs critical power. *European Journal of Applied Physiology*, 124(2):507–526, 2024. 6, 60

[50] Peter S Riegel. Athletic records and human endurance: A time-vs.-distance equation describing world-record performances may be used to compare the relative endurance capabilities of various groups of people. *American Scientist*, 69(3):285–290, 1981. 6, 72

[51] David M Pozar. *Microwave engineering: theory and techniques*. John wiley & sons, 2021. 9, 13, 16

[52] Rainee N Simons. *Coplanar waveguide circuits, components, and systems*. John Wiley & Sons, 2004. 9, 12

[53] Said S Bedair and Ingo Wolff. Fast, accurate and simple approximate analytic formulas for calculating the parameters of supported coplanar waveguides for (m) mic's. *IEEE Transactions on Microwave Theory and Techniques*, 40(1):41–48, 1992. 12

[54] H-E Endres and S Drost. Optimization of the geometry of gas-sensitive interdigital capacitors. *Sensors and Actuators B: Chemical*, 4(1-2):95–98, 1991. 13

[55] Jin Soo Kim et al. Analysis of dielectric sensors for the cure monitoring of resin matrix composite materials. *Sensors and Actuators B: Chemical*, 30(2):159–164, 1996. 15

[56] Lin-Feng Chen, Chong Kim Ong, CP Neo, Vasundara V Varadan, and Vijay K Varadan. *Microwave electronics: measurement and materials characterization*. John Wiley & Sons, 2004. 18

[57] Randall W Rhea. *Discrete oscillator design: linear, nonlinear, transient, and noise domains*. Artech House, 2010. 24, 26

[58] Ulrich L Rohde. A new and efficient method of designing low noise microwave oscillators. 2004. 24

[59] Nhat M Nguyen and Robert G Meyer. Start-up and frequency stability in high-frequency oscillators. *IEEE journal of solid-state circuits*, 27(5):810–820, 1992. 25

[60] Richard G Lyons. *Understanding digital signal processing, 3/E*. Pearson Education India, 1997. 27, 29

[61] Great Scott Gadgets. Hardware components-hackrf documentation. https://hackrf.readthedocs.io/en/latest/hardware_components.html, 2024. Accessed: 31 August 2024. 28

[62] Canadian Grain Commission. Red flour beetle. https://www.grainscanada.gc.ca/en/grain-quality/manage/identify-an-insect/primary-insect-pests/red-flour-beetle.html, 2024. Accessed: 31 August 2024. 42, 67

[63] Canadian Grain Commission. Rusty grain beetle. https://www.grainscanada.gc.ca/en/grain-quality/manage/identify-an-insect/primary-insect-pests/rusty-grain-beetle.html, 2024. Accessed: 31 August 2024. 42, 80

[64] David Long and Fawwaz Ulaby. *Microwave radar and radiometric remote sensing*. Artech, 2015. 42

[65] Fuji Jian and DS Jayas. Detecting and responding to resource and stimulus during the movements of cryptolestes ferrugineus adults. *Food and bioprocess technology*, 2:45–56, 2009. 56, 63